

UNCLASSIFIED

AD 427003

DEFENSE DOCUMENTATION CENTER

FOR

SCIENTIFIC AND TECHNICAL INFORMATION

CAMERON STATION, ALEXANDRIA, VIRGINIA



UNCLASSIFIED

NOTICE: When government or other drawings, specifications or other data are used for any purpose other than in connection with a definitely related government procurement operation, the U. S. Government thereby incurs no responsibility, nor any obligation whatsoever; and the fact that the Government may have formulated, furnished, or in any way supplied the said drawings, specifications, or other data is not to be regarded by implication or otherwise as in any manner licensing the holder or any other person or corporation, or conveying any rights or permission to manufacture, use or sell any patented invention that may in any way be related thereto.

47

4270083

CAT... ..

4270083

RADC-TDR-63-465, Vol. I
FINAL REPORT



INVESTIGATION OF NEW CONCEPTS FOR
MICROWAVE POWER GENERATION
(PLASMA STUDIES)

TECHNICAL DOCUMENTARY REPORT NO. RADC-TDR-63-465

December 1963

Techniques Branch
Rome Air Development Center
Research and Technology Division
Air Force Systems Command
Griffiss Air Force Base, New York

Project No. 5573, Task No. 557303

(Prepared under Contract No. AF30(602)-2833 by School of Electrical
Engineering, Cornell University, Ithaca, New York)

UNCLASSIFIED

DDC AVAILABILITY NOTICE

Qualified requesters may obtain copies from the Defense Documentation Center (TISIR), Cameron Station, Alexandria, Va., 22314. Orders will be expedited if placed through the librarian or other person designated to request documents from DDC.

LEGAL NOTICE

When US Government drawings, specifications, or other data are used for any purpose other than a definitely related government procurement operation, the government thereby incurs no responsibility nor any obligation whatsoever; and the fact that the government may have formulated, furnished, or in any way supplied the said drawings, specifications, or other data is not to be regarded by implication or otherwise, as in any manner licensing the holder or any other person or corporation, or conveying any rights or permission to manufacture, use, or sell any patented invention that may in any way be related thereto.

DISPOSITION NOTICE

Do not return this copy. Retain or destroy.

Suggested Keywords: Plasma studies, electron beam interaction,
beam scanner

ABSTRACT

The design and construction, and preliminary experimental results, of a test vehicle for studying plasma electron beam interaction are described in associated Report A. Two connected chambers of the test vehicle, one at hydrogen pressures as high as 10^{-5} Torr for generation of plasma and the other at pressures less than 10^{-5} Torr for the generation of a high-power electron beam in a convergent flow gun, are described.

A demountable subassembly for generating the plasma and directly coupling S-band signals to and from the plasma and the electron beam by means of a cavity is described. The use of the cavities to diagnose the plasma is described in part, with a more detailed description being presented in associated Report B.

The electron gun used to generate the 5-kv unity microperveance beam, having .20 in. diameter in semi-confined flow, is described. This beam is passed from the low-pressure gun chamber into the high-pressure plasma chamber.

A beam scanner for studying the properties of the electron beam in the gas and plasma environment is also described. Use of this scanner to study the ion-induced beam oscillation is described in associated Report C.

PUBLICATION REVIEW

This report has been reviewed and is approved. For further technical information on this project, contact Mr. R. Hunter Chilton, RALTE, Ext. 4251.

Approved: *R. Hunter Chilton*
R. HUNTER CHILTON
Project Engineer
Directorate of Aerospace Surveillance & Control

Approved: *Paul H. Baldern*
Lt Col USAF
ARTHUR J. FROHLICH
Chief, Techniques Laboratory
Directorate of Aerospace Surveillance & Control

FOR THE COMMANDER:

Irving J. Gabelman
IRVING J. GABELMAN
Director of Advanced Studies

CONTENTS
VOLUME ONE

	Page
I. INTRODUCTION	1
II. VACUUM SYSTEM	5
A. SYSTEM OPERATION	5
B. GAS FLOW AND IONIZATION CONFIGURATION	8
C. HYDROGEN LEAK TUBE	13
D. FOCUSING SOLENOID	16
III. THE INTERNAL PLASMA SUBASSEMBLY	18
A. MECHANICAL-ELECTRICAL DESIGN	18
B. PREDICTED PLASMA-DENSITY PROFILE	25
C. THE CAVITIES	26
IV. ELECTRON GUN DESIGN	30
V. BEAM-SCANNING EQUIPMENT	38
BEAM SCANNING MECHANISM	39
1. Control of Faraday Cage Motion inside Vacuum System	39
VI. EXPERIMENTAL RESULTS	47
VII. CONCLUSIONS	51
VIII. REFERENCES	52

	Page
SUMMARIES	53

TECHNICAL REPORTS

ANALYSIS OF THE INTERACTION OF AN ELECTRON BEAM
WITH A PLASMA H. Marantz

PLASMA DIAGNOSTICS D. M. Kerr

ION-INDUCED OSCILLATIONS OF ELECTRON BEAMS
A. S. Gilmour, Jr.

A TEST VEHICLE FOR THE STUDY
OF THE INTERACTION OF A HIGH-POWER
ELECTRON BEAM WITH A PLASMA

L. F. Eastman, D. Kerr, H. Marantz,
Y. Narayan and J. J. Clark*

* Cornell Aeronautical Laboratory, Buffalo, New York

I. INTRODUCTION

In attempts to achieve higher microwave powers at higher frequencies, new methods of harnessing the controlled energies of electron streams are being investigated. One promising method that has begun to be studied in a few laboratories is that of using the electrons in a plasma of a partially ionized low-pressure gas to interact with a controlled, linear electron beam.

Use of a plasma as an interaction "circuit" in linear beam tubes has advantages over a conventional circuit. First, longitudinal waves are coupled very strongly to the electron beam even at extremely high frequencies. This is due both to the intimate mixture possible of the electron beam and the plasma, and to the fundamental properties of the plasma at microwave frequencies. This strong coupling leads to very high gain per centimeter along the path of the electron beam and should also allow greater efficiency in harnessing the electron beam. Second, for a plasma, there is only a set of simple surfaces removed from the electron beam region necessary to maintain the plasma, whereas for slow-wave circuits in conventional traveling-wave tubes at high frequencies, fine, delicate metal electrodes are needed near the electron beam. As a result, much less intricate machining is required with a plasma. There is also much less danger of stray beam electrons damaging the electrode structure because of the thermal effects of bombardment.

Finally, the properties of the plasma can be easily controlled externally by controlling the plasma-generating discharge current, the gas pressure, and the magnetic field that is applied along the direction of the electron beam flow to confine the electron beam and the plasma electrons.

To attain high-power amplification of microwave signals using the interaction of an electron beam with a plasma, several problems need to be solved. First, the natural fluctuations of the plasma and thus the fluctuation of its microwave properties must be minimized. These fluctuations are functions of the electrode structure used to maintain the plasma (as well as of the confining magnetic field), the gas composition and pressure, and the plasma discharge current. Resonant cavities measure the fluctuations in the density and loss of the plasma as well as microwave noise. Next, the fluctuations of the electron beam caused by its coupling to that portion of the plasma that is generated by the electron beam must be minimized. This portion of the plasma also fluctuates, mainly because of its interaction with the electron beam. This beam-generated portion of the plasma can either be generated in a region where no plasma would be generated by any other means, or it can be generated as excess plasma in a region where moderate fractional ionization has already been brought about by other means. In either case, fluctuations of the beam and its beam-generated plasma can be measured under controlled, pulsed beam conditions using a beam-scanning mechanism to diagnose the beam, with no microwave signals applied and with the plasma discharge either off or on. Next there is the problem of coupling the microwave

signals through the plasma and to the beam-plasma system at the core of the plasma. This direct coupling is difficult, compared with coupling to the electron beam before it enters the plasma, but it is necessary to use fully the beam-plasma amplifier's potential advantage in removing the electrodes from close proximity to the electron beam. The difficulty arises because the properties of the dense plasma are so different from a vacuum, or even a vacuum containing an electron beam. The problem can be approached by studies of the fringing fields of a beam-plasma system of finite diameter and of the interaction of such a system with a low-loss resonant cavity. Finally, there is the problem of understanding and controlling the high small-signal gain per centimeter of beam travel in a beam-plasma system, having a finite geometry as well as the saturating beam and plasma nonlinearities. The small-signal part of this problem can readily be solved by simultaneous analytical and experimental studies, but the large-signal problem is much more difficult, even when using the best balance of analytical and experimental studies.

In order to help solve some of these problems, a comprehensive beam-plasma test vehicle was designed and constructed. This test vehicle had two chambers connected by a small cylindrical tunnel. A pulsed electron gun of unity micropervance and capable of generating an electron beam of up to 10 kw was placed in one chamber. The electron beam passed through the tunnel into the other chamber, where a flexible plasma-generating structure and microwave cavities for coupling simultaneously to the beam and plasma were located in an

internal subassembly. Using hydrogen gas at pressures of the order of 10^{-3} Torr in the plasma chamber, the beam-plasma amplification interaction could be investigated in detail at a chosen frequency of 3,000 Mc/s.

This report includes a detailed description of the main vacuum system, the internal plasma subassembly, the electron gun and focusing structure, and the spent beam-scanning mechanism. It also includes a discussion of the design, experimental methods used, and preliminary results.

Three reports are appended. These report on the plasma diagnosis method and measurements ("Plasma Diagnostics", by D. M. Kerr); on experimental results and qualitative descriptions of ion oscillations in linear beams ("Ion-induced Oscillations of Electron Beams", by A. S. Gilmour) and on the theoretical analysis of small-signal gain in finite beam-plasma systems ("Investigation of the Interaction of an Electron Beam with a Plasma", by H. Marantz).

II. VACUUM SYSTEM

This chapter describes a universal test vehicle for the beam-plasma interaction. The vacuum system and other associated system components of this test vehicle are shown in Figures 1 and 2. The system consists of an electron gun region, which is pumped by a 400 l/s VacIon pump and which can be sealed off from the remainder of the test vehicle by the vacuum ball valve to the left of the gun region. To the left of the ball valve is the plasma region, and to the left of this is the beam-scanning area for tests on the spent electron beam. Hydrogen gas is provided by a palladium leak tube. The leak rate is controlled by adjusting the power applied to a heating coil in the tube. In addition there are the following system components:

1. a Philips cold-cathode-discharge vacuum gauge,
2. an auxiliary 8 l/s VacIon pump for rapid evacuation of the test region,
3. an electromagnet used in the beam-plasma region to generate a d-c magnetic field up to 1200 gauss, and
4. a portable unit for starting the VacIon pumps.

A. SYSTEM OPERATION

Operation of the vacuum system was as follows: Upon assembly of the system, the portable starting unit was used to reduce the system pressure to at least 5×10^{-3} Torr. This consisted of a rough mechanical

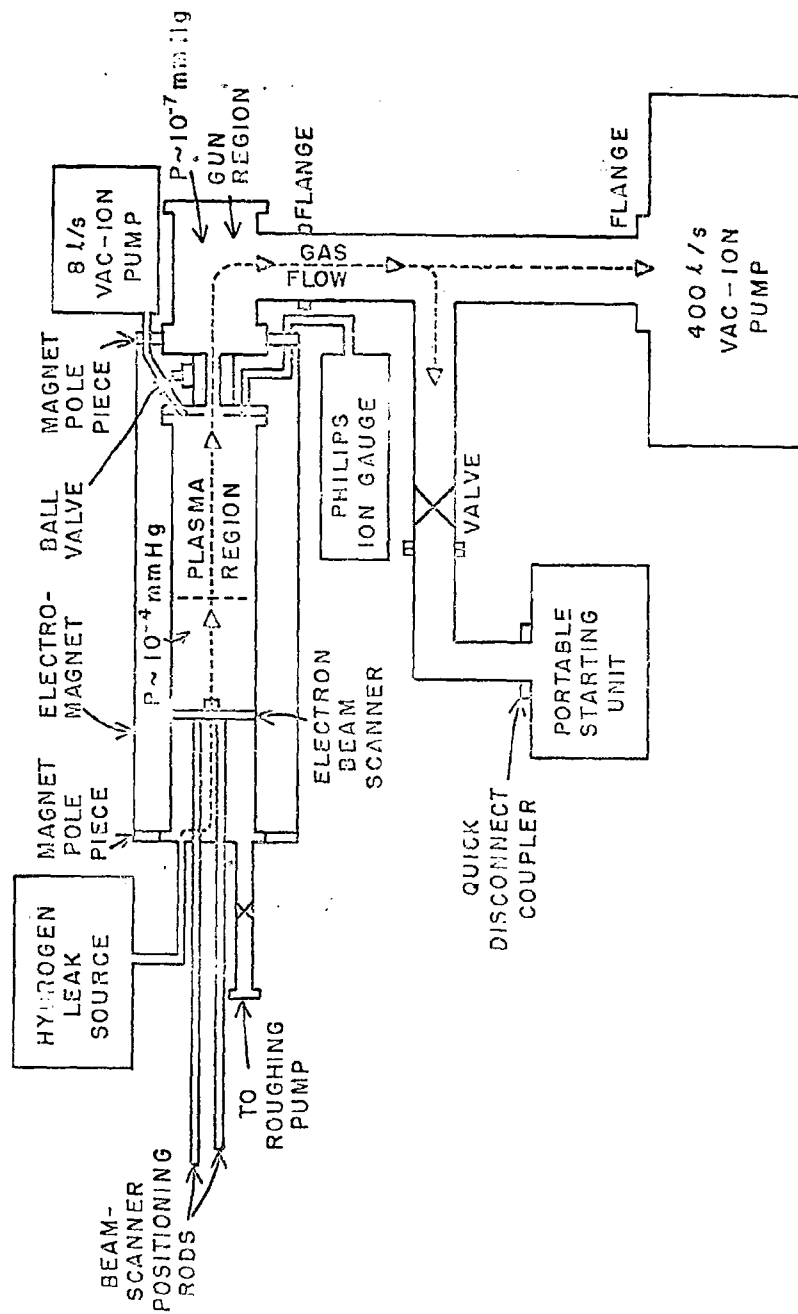


FIGURE 1. Vacuum System and Associated Components of Beam-Plasma Amplifier.

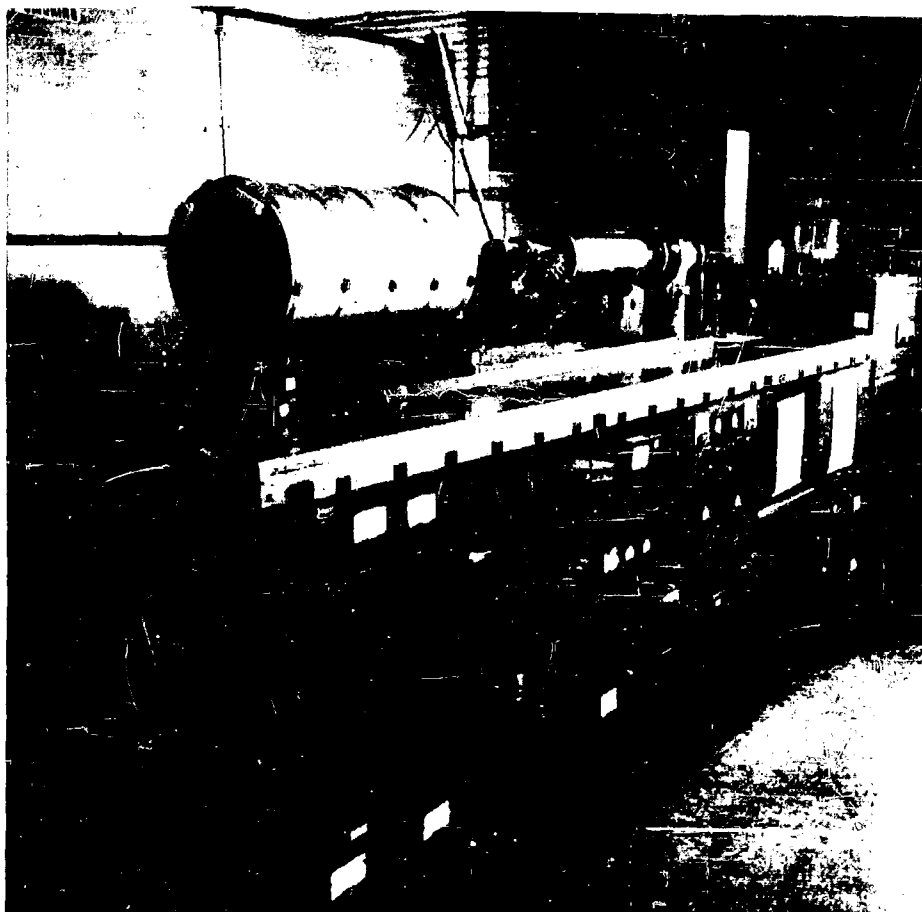


FIGURE 2. Test Vehicle.

pump, a cold trap, and VacSorb pumps. The 8 l/s and 400 l/s VacIon pumps were started next, and the portable starting unit was valved off and disconnected from the system by means of a Veeco quick coupler; then the VacIon pumps reduced the over-all system pressure to a working level. The plasma cathodes were then heated, and pumping continued until a steady-state system pressure of 1×10^{-9} Torr was reached in the gun region and 1×10^{-7} Torr in the plasma region. Next, the 8 l/s VacIon pump was shut off, and the hydrogen leak source was turned on to raise the hydrogen pressure as high as 1×10^{-3} Torr in the plasma region.

It should be noted that in the process of making changes in the internal subassemblies, the ball-valve arrangement (shown in Figure 3), in conjunction with the valve in the beam-scanner region and that in the gun section, allowed either side of the ball valve to be pumped or be let down to air independently of the other side.

B. GAS FLOW AND IONIZATION CONFIGURATION

Most previous investigators of beam-plasma interaction phenomena have used either mercury or cesium gas for the plasma. This is because the mercury easily yields the pressures of interest in the 10^{-4} - 10^{-3} Torr region, in room-temperature equilibrium with its liquid phase, while cesium is easily ionized by contact with a heated tungsten surface. Hydrogen, however, is easily controlled in pressure by either the controlled-leak method or by the heated-generator method. Also since hydrogen is

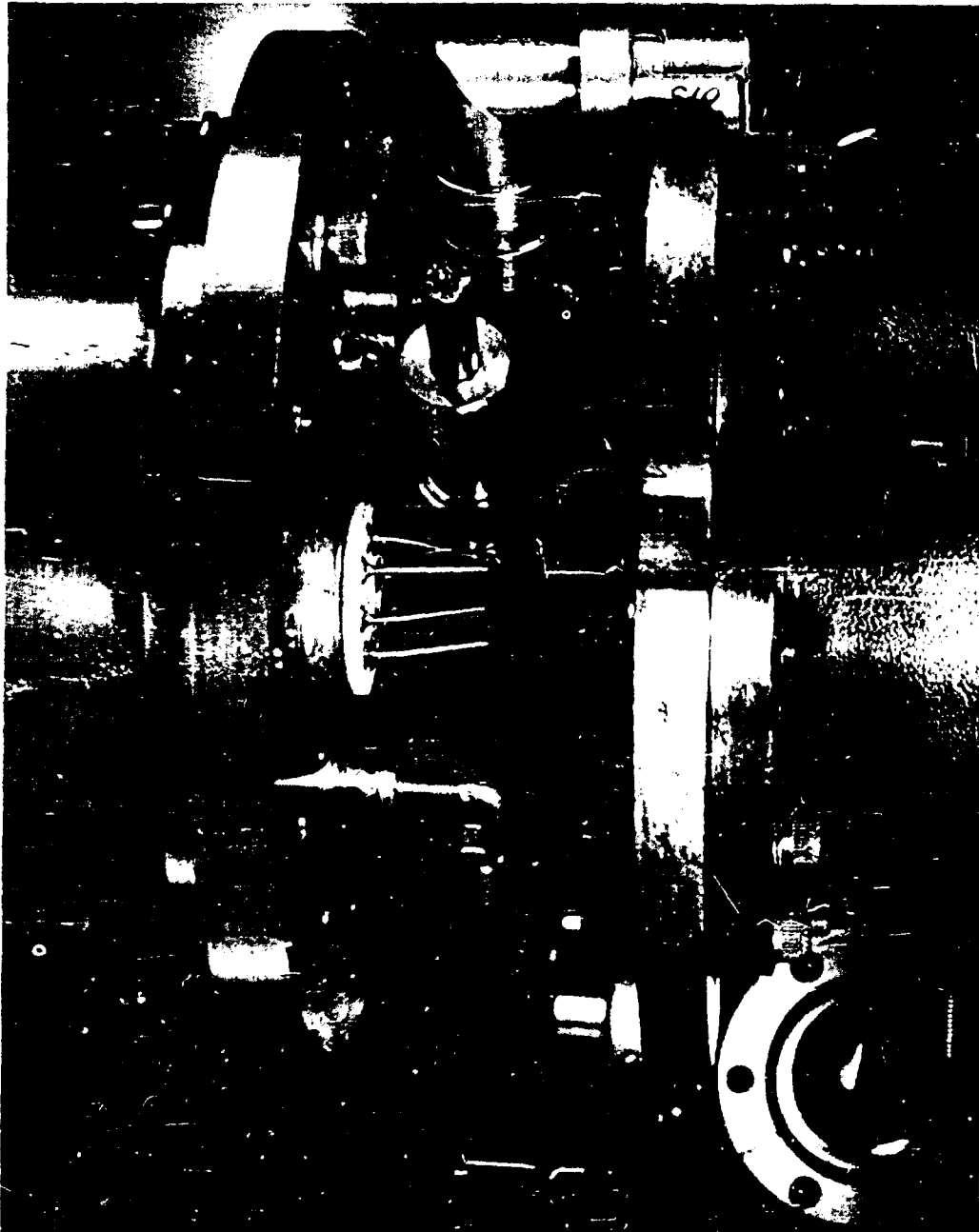


FIGURE 3. Close-up View of Bali-Valve Section.

the lightest gas, its ions cause the least sputtering of the cathodes used in both the plasma discharge and the electron gun. Finally, hydrogen does not damage the cathode chemically; in fact, it improves emission somewhat.

To avoid contamination of the cathodes (especially the cathode in the electron gun), cold-cathode, gas-discharge, getter-ion (VacIon) pumps were chosen for this experiment. Since the pump makes it possible to pump hydrogen faster than air,¹ this further adds to the difference in pressure between the high-pressure plasma region (where the hydrogen source is located), and the low-pressure gun region (where the pump is located).

The 400 l/s VacIon pump was capable of pumping hydrogen at a rate of over 1000 l/s at a pressure of 10^{-6} Torr. Since the ball-valve arrangement between the plasma region and the gun region was chosen to have a conductance of approximately 10 l/s for hydrogen, the pumping speed of the over-all system for hydrogen was expected to be approximately 10 l/s; and there should have been a ratio of 100:1 in pressure between the two regions when the hydrogen gas was being leaked in. The 10^{-6} pressure in the region of the beam gun was desirable (1) to minimize back-ion bombardment and (2) to minimize space-charge defocusing and ion-fluctuation effects, which would occur in the gun region at higher pressures. Higher pressure could damage the gun cathode during the 5-kv negative pulses, cause beam scalloping and fluctuation, and in addition prevent long-life operation of the 400 l/s VacIon pump.

The pressure of $10^{-4} - 10^{-3}$ Torr in the plasma region was a compromise to obtain electron plasma densities sufficiently high at low discharge voltages without simultaneously causing excessive scattering of the electron beam and an excess of H^+ ions. As a result, collisions of beam electrons with the neutral gas, H^+ ions would be produced by the electron beam at a rate given by²

$$n^+(t) = (n_0^-) (\nu_i t) \quad ,$$

where

- $n^+(t)$ = the ion density of the beam-generated plasma (ion/cm³),
- n_0^- = the electron density of the beam (electrons/cm³),
- ν_i = the ionization frequency of beam electrons (sec⁻¹),
- t = time in seconds .

We can obtain ν_i from

$$\nu_i = u_0 P_{ei} p = 1.9 \times 10^9 p \text{ (sec}^{-1}\text{)} \quad ,$$

where

- u_0 = the d-c velocity of electron beam (cm/sec) ,
- P_{ei} = the probability of ionizing collisions per centimeter of path per millimeter of mercury pressure,
- p = pressure in millimeters of mercury.

We define t_{SCN} as the time required for the ions to produce space-charge neutralization of the beam electrons; this is given by

$$t_{SCN} = \frac{1}{\nu_i} = \frac{.52 \times 10^{-9}}{p}$$

The 0.4-a electron beam is 0.20 in. in diameter. These assumptions give an electron density for the beam of approximately $10^9/\text{cm}^3$. If we now assume an average pressure of $.5 \times 10^{-4}$ Torr in the drift-tube region and a beam-pulse duration of 10 μs , we have

$$n^+ = (n_0^-) (\nu_i t) ,$$

$$n_{\text{max}}^+ = 10^9 \text{ ions/cm}^3 ;$$

i. e., space-charge neutralization occurs at the end of the pulse.

It has been shown (see Report C by A. S. Gilmour) that serious beam fluctuations of about a few megacycles occur at the space-charge neutralization point during a pulse. This effect can be delayed by lower pressure and better ion drainage.

Recent studies³ on ion defocusing in Brillouin-focused electron beams showed that there was a noticeable distortion of the beam shape when the space charge of the ion was only about one-fourth the space charge of the beam. With semiconfined magnetic focusing, defocusing of the space charge of the beam by ions is greatly reduced. The radius of the beam in a gun with semiconfined flow remains greater than three-fourths of the original space-charge radius, whereas the radius of a Brillouin beam will, theoretically, be reduced to zero with complete neutralization. To avoid reduction of the beam radius, therefore, a gun with semiconfined flow was used.

Further steps were taken to minimize the effects of ion bombardment of the cathode. The profile of the potential of the system was such that ions created in the plasma region would be accelerated to

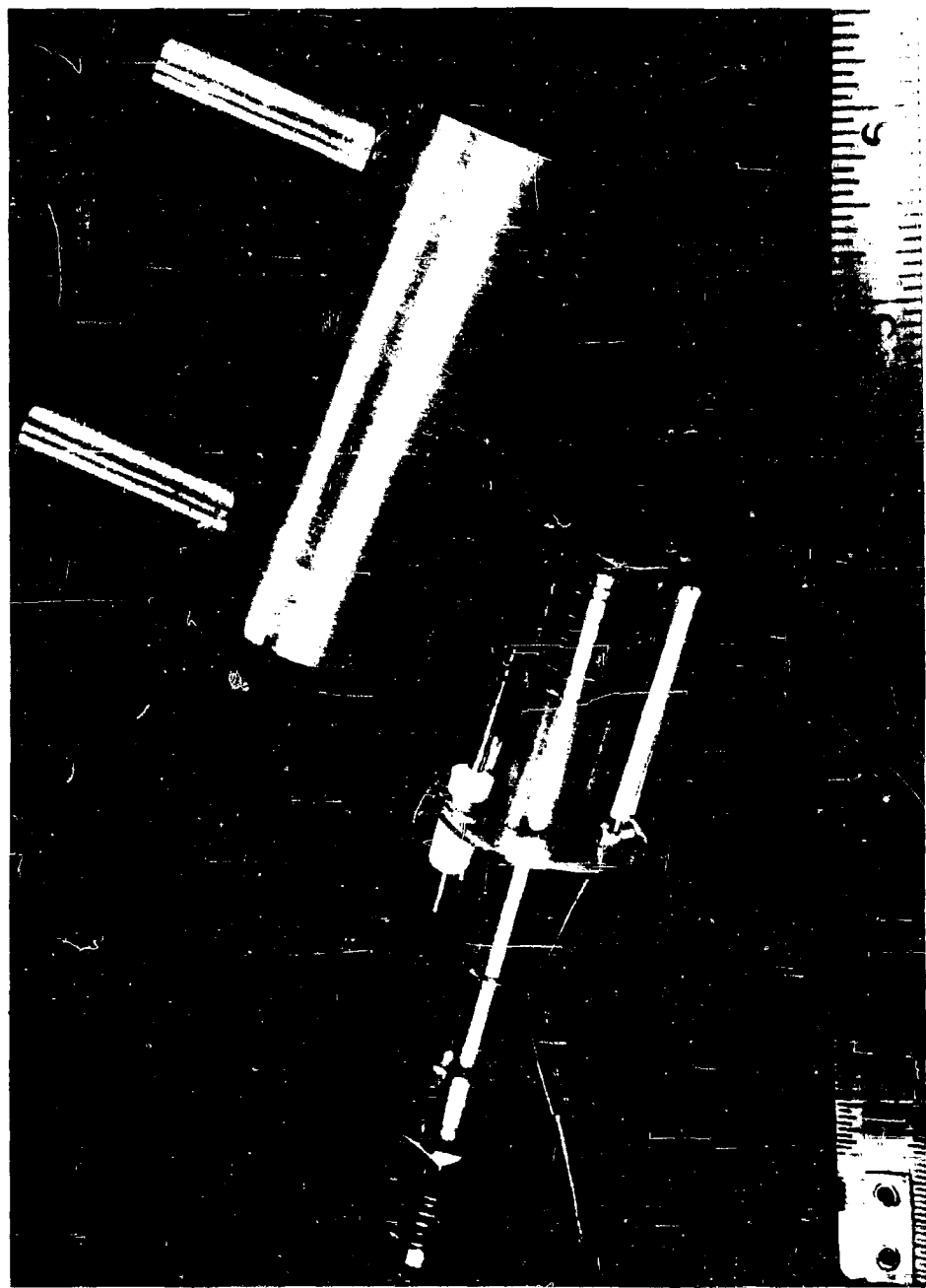
the plasma cathodes by a potential of only -25 v. The ions would be reflected by an effective positive potential of 25 v in the grounded ball-valve region. This potential profile acted as an ion trap. Any of the few ions which did diffuse back through the ball-valve section, and those created in the high-pressure ball-valve region, would be accelerated by the negative 5-kv pulses applied to the gun cathode, but their bombarding effects would be minimized because:

1. the electron gun has a high (50:1) area convergence to localize the deterioration to the center of the cathode;
2. a low (<.001) duty cycle minimizes the time that the ions bombard the cathode.

C. HYDROGEN LEAK TUBE

To maintain the desired pressure of hydrogen gas in the plasma region and to control the increase in pressure in this region over that in the gun region, a hydrogen-leak apparatus was used in conjunction with pumping units. A palladium leak tube with a maximum leak rate of 2 l/s at 1×10^{-3} Torr pressure constructed in this laboratory is shown in Figure 4. Another leak tube was purchased, whose rate was 100 l/s at the same pressure. Such a tube was the center of this system. A mixed-source gas could be used to leak pure hydrogen into the evacuated system, because only hydrogen diffused through palladium.

The theoretical explanation for the operation of the tube is described by the diffusion equation,



$$D = \frac{k}{d} p^{\frac{1}{2}} e^{-b/T}$$

where D is the rate of diffusion (defined as the volume of gas in cubic centimeters reduced to S. T. P.) that diffuses through one square centimeter of wall surface per second per millimeter of wall thickness; p is the gas pressure in millimeters of mercury; T is the temperature of the metal in degrees Kelvin; d is the thickness of the metal wall in millimeters; and b and k are constants for the particular system. Calculations were made using this equation with known constants to determine the surface area of palladium to be used in the tube constructed in this laboratory for a desirable range of controlling temperatures.

Figure 4 gives an indication of the size and some indication of the function of the particular elements of the tube. The hydrogen leak is a stainless steel tube through which the hydrogen-nitrogen gas mixture flows. The palladium diffusion surface is simply a small square of metal brazed to a Kovar tube of proper size, which is heated by a filament that surrounds it, and which is enclosed in the hydrogen leak tube. A thermocouple was spot-welded to the palladium surface. A plot was made of the characteristic of pressure versus temperature. In addition, a power supply for the filament was constructed, which included a variable-voltage control, and a meter to indicate the thermocouple temperature. To avoid the possibility of a hydrogen explosion, a gas mixture of low hydrogen content is desirable. Commercial

forming gas* (8 per cent hydrogen, 92 per cent nitrogen) was used, and since the palladium tube allowed only the hydrogen gas to diffuse through its walls, the presence of nitrogen in the known mixture did not affect the purity of the hydrogen plasma gas.

D. FOCUSING SOLENOID

To avoid radial diffusion of the plasma electrons and simultaneously focus the electron beam, a solenoid capable of establishing d-c axial magnetic fields up to 1200 gauss, and its associated power supply (15 a maximum) were constructed. Provision was made for adjusting the solenoid vertically and horizontally. Measurements of the magnetic field of the solenoid alone and in combination with the solenoid pole pieces indicated that a decrease in the strength of the magnetic field occurred in the region of the ball valve. It was found that the stem of the ball valve, which was machined at Cornell University, was made of material that was slightly magnetic, and therefore perturbed the magnetic field enough to perturb the electron beam. This perturbation did not seriously alter the beam performance. Also, since the plasma itself was not located near the ball valve, it was not perturbed by this decrease in magnetic field. Therefore, measurements

* Later in the program it was found desirable to have forming gas flowing when the VacIon pumps had to be let down to air. The forming gas was leaked directly into the 400 l/s VacIon pump (after shutoff and during residual pumping) before the pump was let down to air. This made it easier to restart the pump.

on the various plasma parameters are to be continued as scheduled.

The high magnetic field in the electron gun region was caused by the magnet of the 400 l/s VacIon pump and stray solenoid fields and was controlled by properly shielding the pump fields and using a small external bucking coil.

For optimum operation in future work, the design that is being developed on another program* for the configuration of the magnetic field for best confined flow will be used. The magnetic field in the pole pieces, plasma cathode, and plasma regions agreed with theoretical predictions.

* Linear Beam Contract No. AF 30(602)-2573,

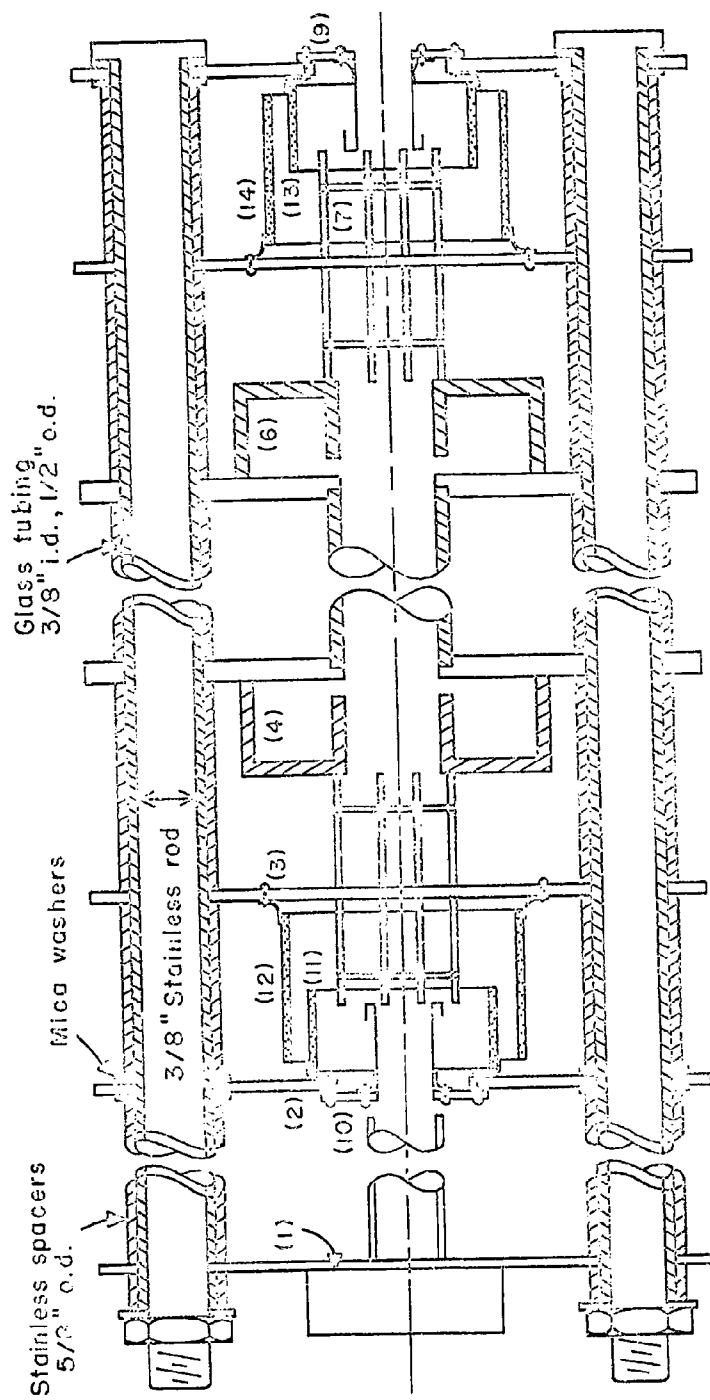
III. THE INTERNAL PLASMA SUBASSEMBLY

A. MECHANICAL - ELECTRICAL DESIGN

This section describes the design and construction of the sub-assembly (see Figures 5 and 6) to create the Penning-discharge plasma and to couple the signal to and from the beam-plasma system. The flexibility of this assembly is apparent from its demountable design. The cathode separation, interaction length, etc. could be changed by changing the spacer dimensions. The subassembly could be assembled as a separate unit and then mounted on main support rods that were heliarced to the flange of the ball valve. Because the vacuum system and the connecting ball valve were demountable, the entire test vehicle had great flexibility.

The Penning discharge was generated by opposing impregnated ring cathodes, which gave a Penning-discharge geometry when combined with the cylindrical anode and longitudinal magnetic field. The dual hot-cathode Penning discharge yielded an S-band density plasma at pressures as low as 10^{-4} Torr. The electrons were trapped axially by the electrostatic field and radially by the magnetic field. The primary electrons therefore had to make several axial transits before being collected at the anode. The same mechanism trapped plasma electrons generated by primary electron-neutral collisions.

The anode structure was made of three sections. The cylinder in the interaction region between the two cavities was of copper in order



Key: (1) Collector ; (2) Left cathode ; (3,7) Mesh anode to allow viewing of plasma ; (4) Output cavity ; (5) Anode "spool", 2" drift space ; (6) Input cavity ; (8) Right cathode ; (9,10) Back electron shield ; (11,13) Heat shield on cathode plate ; (12,14) Heat shield on anode plate.

FIGURE 5. Internal Plasma Subassembly.

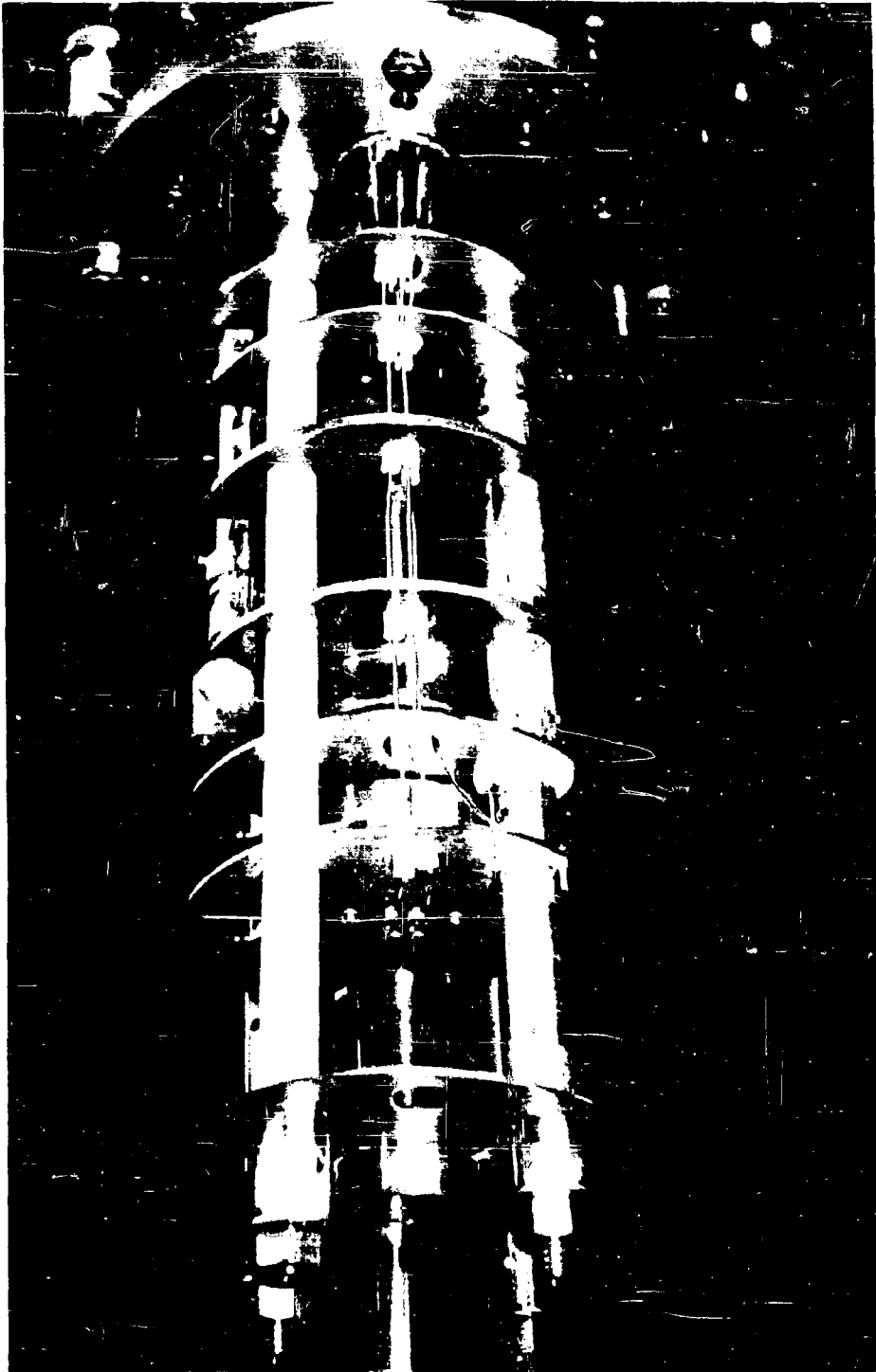


FIGURE 6. Internal Plasma Subassembly.

to reduce losses at microwave frequencies and to stabilize the plasma in that region. The sections from the cavities to the cathodes were made of stainless steel wires arranged in a circle to allow observation of the plasma and, at the same time, stabilizing the plasma.

The ring cathodes used for the generation of the plasma were of the impregnated type and are shown in Figure 7. The cathode mounting is shown in Figure 8a. The cathode was operated at a negative potential of approximately 25 v and the anode at ground potential. Since the ball-valve flange is at ground potential, there is a possibility of backward flow of electrons from the back of the heated cathode, which could cause arcing. This is prevented by the relatively cool molybdenum backing plate at cathode potential, as shown in Figure 8a. The backing plate has a hole to allow the electron beam to pass and the cathode is held to this backing plate by means of three tantalum wires 120° apart. These have small areas of contact between the cathode and support plate and reduce heat loss by conduction. A hollow stainless-steel tube, polished on the inside, is used as a heat shield around the cathode. A similar shield of a larger diameter is mounted to the anode support plate, as shown in Figures 8b and c and Figure 6.

The heater leads were brought to ceramic standoffs to which connections could be made. The heater power recommended by the manufacturer was 150 w/in.^2 of cathode surface, or 20 w for this surface. A bell-jar test was run and the brightness temperature of the cathode surface was measured as a function of heater power. The results were plotted in Figure 9. It was found that because of side

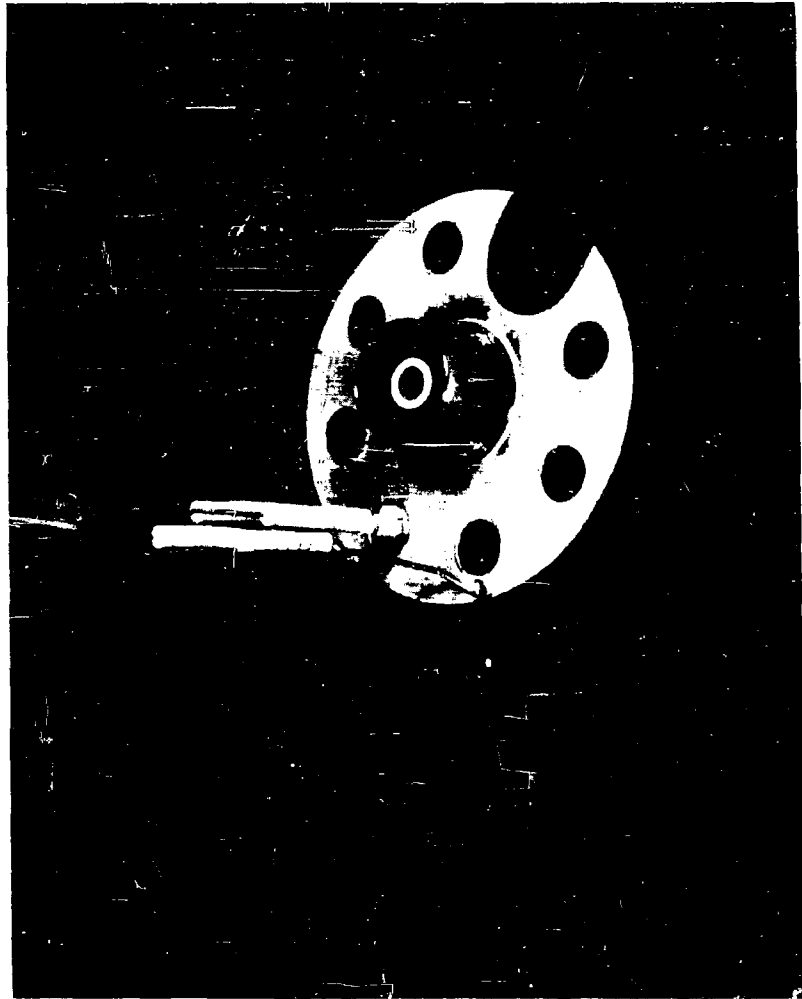
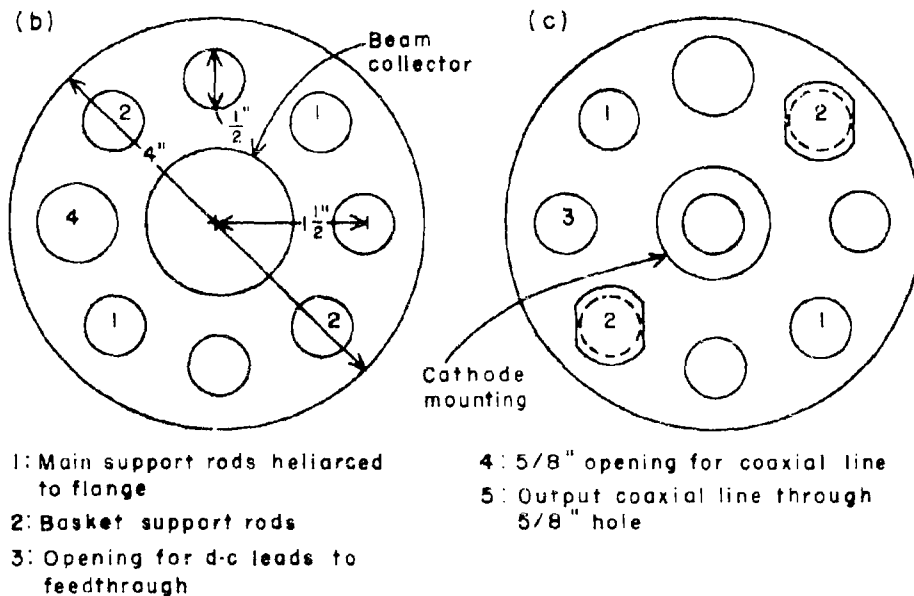
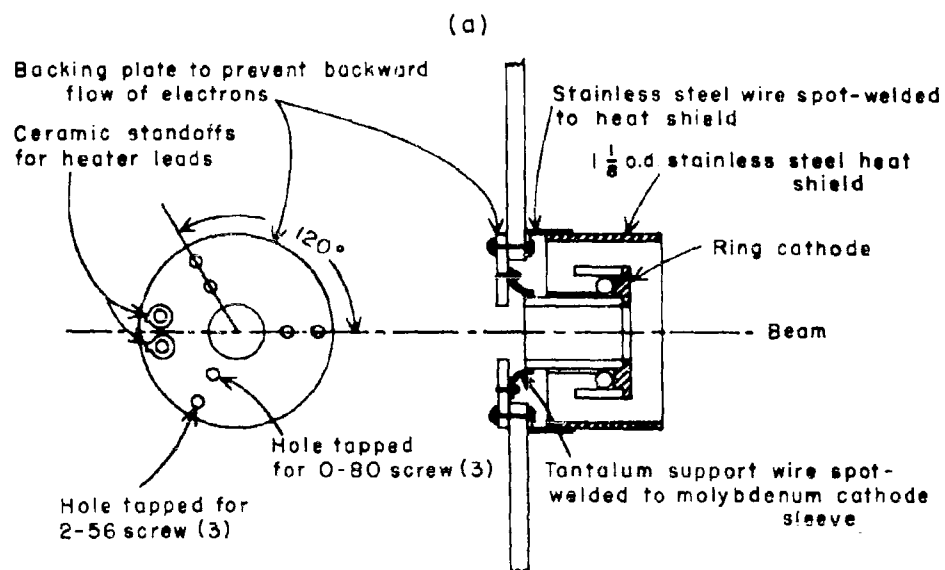


FIGURE 7. Ring Cathode with Its Heat Shield.



FIGURES 8a. Mounting of Plasma Cathode; 8b, c. Support Disks for Plasma-forming Subassembly Showing Orientations of Support Rods (b) Input Coaxial Line at Beam Collector and (c) Output Coaxial Line at Input

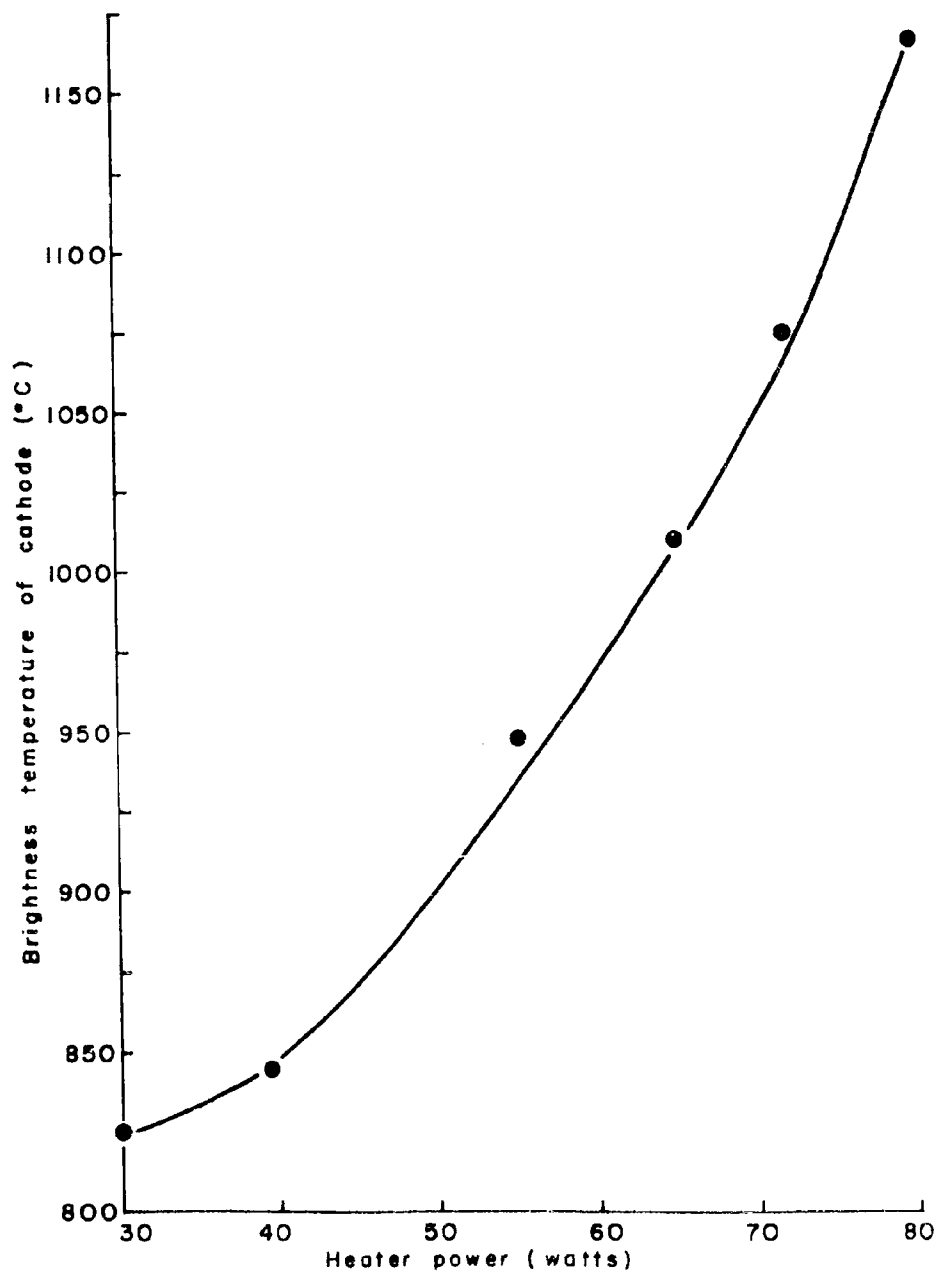


FIGURE 9. Ring Cathode Temperature versus Heater Power

radiation losses and support conduction losses, heater power of 80 watts per heater was required to attain the rated brightness temperature of 1490° C.

The d-c connections to the subassembly were made to an octal feedthrough in the ball-valve flange. The connection to the feedthrough from the heaters, cathode, etc. were made by copper wires with ceramic insulators to prevent short circuits.

B. PREDICTED PLASMA-DENSITY PROFILE

The radial density profile of the electrons and ions in the plasma generated by the thermionic electrons from a ring cathode can be determined by solving the continuity equation,

$$\frac{\partial n}{\partial t} - D \nabla^2 n + C = 0, \quad (3.1)$$

where n is the plasma particle (primarily ion) density per unit volume; C is the net rate of particle creation per unit volume per unit time; and D is the diffusion constant. Under steady-state conditions $\partial n / \partial t = 0$, we get

$$\nabla^2 n + \frac{C}{D} = 0 \quad (3.2)$$

For the case of a ring cathode of radius a and a hole of radius b in a hollow cylinder of radius R , we can solve Equation (3.2). In a hollow cylinder, n is independent of ϕ and z ; therefore Equation (3.2) reduces to

$$\frac{\partial^2 n}{\partial r^2} + \frac{1}{r} \frac{\partial n}{\partial r} + \frac{C}{D} = 0 \quad (3.3)$$

The solution is

$$\begin{aligned} n &= K_1 \ln \frac{R}{r} \quad , \quad a \leq r \leq R \quad ; \\ n &= K_2 r^2 + K_3 \ln r + K_4 \quad , \quad b \leq r \leq a \quad ; \\ n &= K_5 \quad , \quad 0 \leq r \leq b \quad . \end{aligned}$$

When the boundary conditions that n and $\partial n / \partial r$ are continuous at $r = a, b$ are used, the constants can be evaluated to give

$$2R = 0.625 \text{ in.}, \quad 2a = 0.500 \text{ in.}, \quad 2b = 0.300 \text{ in.},$$

and the normalized expressions in terms of C/D are

$$\begin{aligned} n \frac{D}{C} &= 0.055 \quad , \quad 0 \leq r \leq b \quad ; \\ n \frac{D}{C} &= 0.161 + 0.073 \ln r - 0.25 r^2 \quad , \quad b \leq r \leq a \quad ; \\ n \frac{D}{C} &= -0.029 - 0.126 \ln r \quad , \quad a \leq r \leq R \quad . \end{aligned}$$

This profile is plotted in Figure 10.

C. THE CAVITIES

Gridless-gap cavities of the singly re-entrant type were designed and constructed to couple power on and off the system. Copper loops force-fitted into the ends of a 1/4 in. center conductor of rigid coaxial lines coupled power to the cavities. The copper center conductors were tapered along a one-wavelength distance near the loops

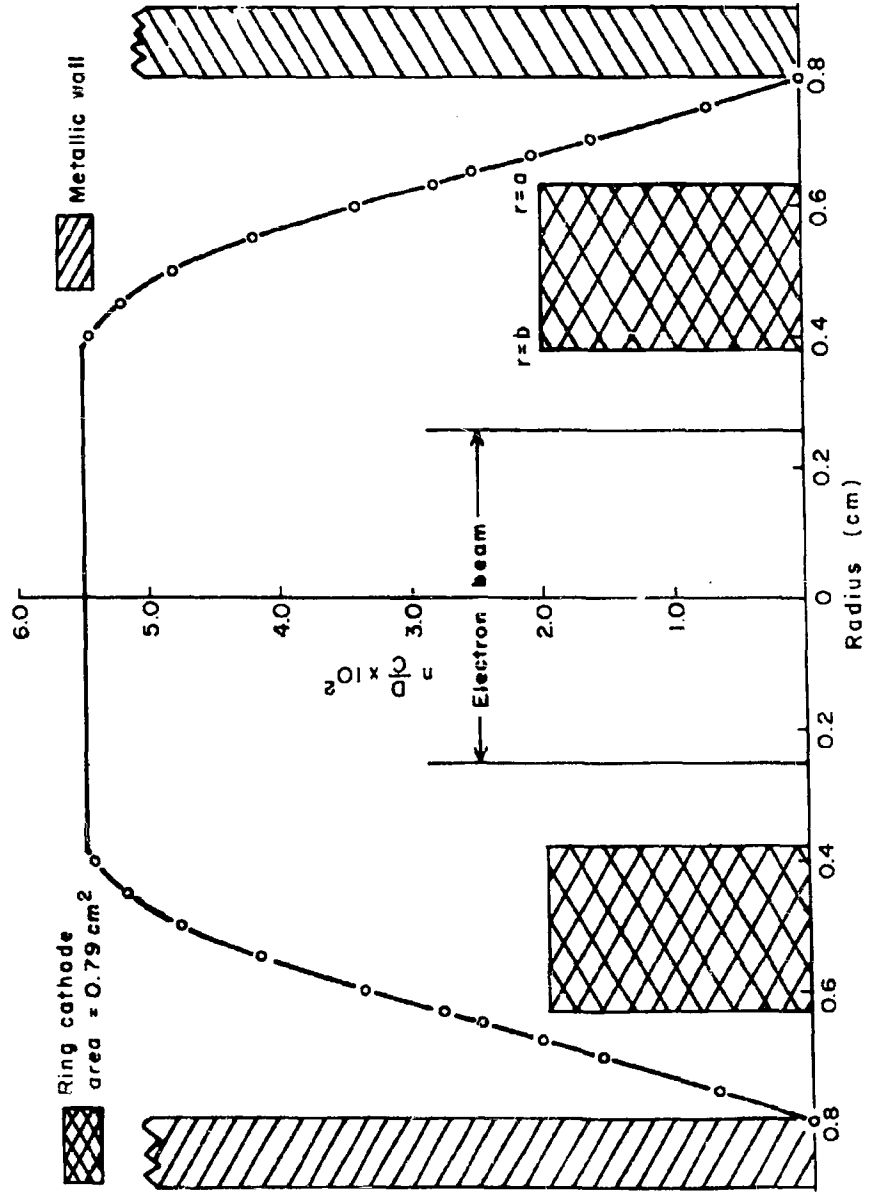


FIGURE 10... Normalized Electron Density (or Ion Density) versus Radius for a Cylindrical Plasma Column.

to avoid standing waves on the line. The vacuum seals to the cavities were made by compressing teflon discs at two points of contact, i. e., break points in the inner and outer conductors of the rigid coaxial transmission line. This seal was designed to cause virtually no electrical discontinuity in the transmission line. The vacuum jacket seal was made to the outer conductor by a Veeco vacuum coupler in the output flange. The cavities were slightly overcoupled to the transmission lines, since the plasma tended to compensate by loading the cavities. The cavity, its coupling scheme, and the vacuum seal are explained in detail in Report B of this report and a photograph of these components is shown in Figure 11.

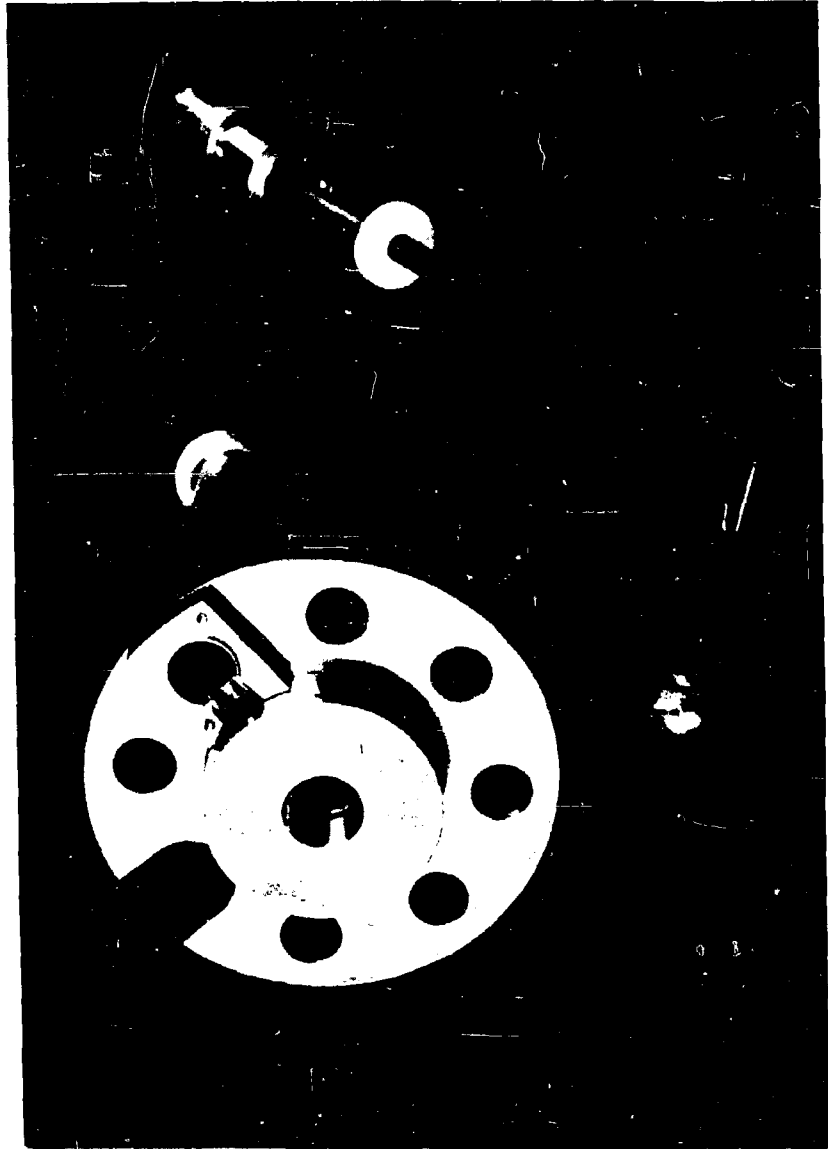


FIGURE 11. Disassembled Microwave Cavity.

IV. ELECTRON GUN DESIGN

An electron gun was designed, based on the Sperry Gyroscope Company STL-100 gun used previously at this laboratory in linear beam studies.⁴ The internal dimensions were the same as those of the STL-100, but the new gun was made entirely of stainless steel and set screws were used in the assembly for greater flexibility. Stainless steel was used instead of cold-rolled steel so that semiconfined magnetic focusing could be used in place of Brillouin focusing. With semiconfined magnetic focusing, defocusing of the space charge of the beam by ions is greatly reduced. The radius of the beam in a gun with semiconfined flow will remain greater than three-fourths of the original space-charge radius, whereas the radius of a Brillouin beam will, theoretically, be reduced to zero with complete neutralization. To avoid reduction of the beam radius, therefore, a gun with semiconfined flow is preferable.

Steps were taken to minimize the effects of ion bombardment of the cathode. The profile of the potential of the system was such that ions created in the plasma region would be accelerated to the plasma cathodes by a potential of only about -25 v. The ions would be reflected by an effective positive potential of 25 v in the grounded ball-valve section between the gun and the plasma region. This potential was expected to act as an ion trap. Ions which did diffuse back through the ball-valve section and those created in the electron gun would have their bombarding

effects minimized by the following means:

1. an electron gun with a high (50:1) area convergence to localize the deterioration to the center of the cathode;
2. a low duty cycle (<.001) to minimize the time that ions bombarded the cathode;
3. use of hydrogen gas, since this ion causes less cathode sputtering than other gases because of its low mass;
4. differential pumping resulting from the constriction of the ball-valve section that permitted a 100:1 pressure differential between the plasma region and the electron gun.

The specifications to be met by the gun design were: a 5-kv, 40-a beam at unity microperveance with a beam diameter of .20 in. and an area convergence of 50:1. The gun uses semiconfined flow with the focusing magnetic field four times that required for Brillouin focusing. The gun and focusing magnet were constructed at Cornell. The intermediate details of the gun are shown in Figure 12. The layout of the gun assembly is shown in Figure 13, and a photograph of it in Figure 14. The supporting structure was designed both to locate and rigidly support the electron gun. The pole piece was one of the vacuum flanges on the ball-valve section and the anode was positioned on the pole piece by a stainless-steel ring. The gun was supported at the rear by another stainless-steel ring and rods attached to the rear T-section flange.

When the strength of the magnetic focusing field was measured along the axis of the system, two problems arose. At the position of

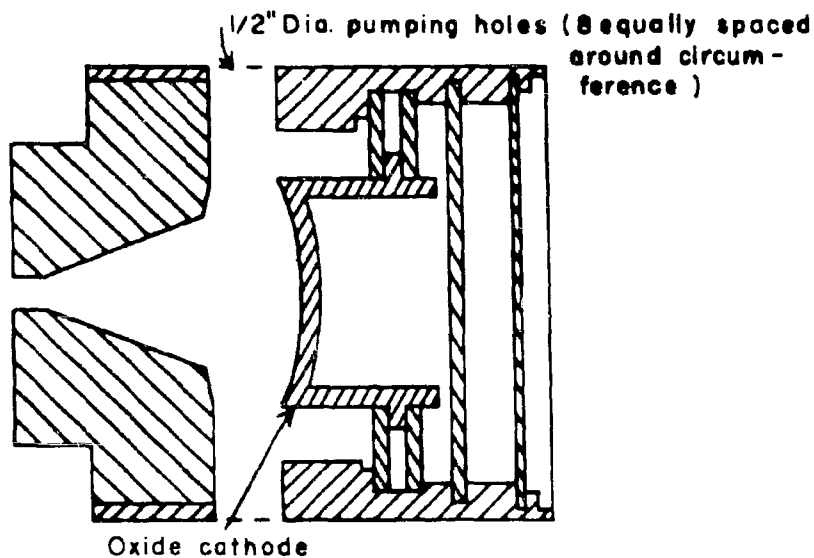


FIGURE 12. Details of Electron Gun.

the ball valve, there was a sudden dip in the field, which was found to be caused by a piece of magnetic material inadvertently used in the construction of the valve; in the gun region, the field strength was found to be much higher than that necessary for operation with semi-confined flow. It was decided to leave the ball-valve section unchanged and construct a new valve later if necessary, since the risk involved in trying to machine away the magnetic material was too great. Preliminary data could then be taken despite the small irregularity in the field. The problem of the excess magnetic field in the gun region was solved

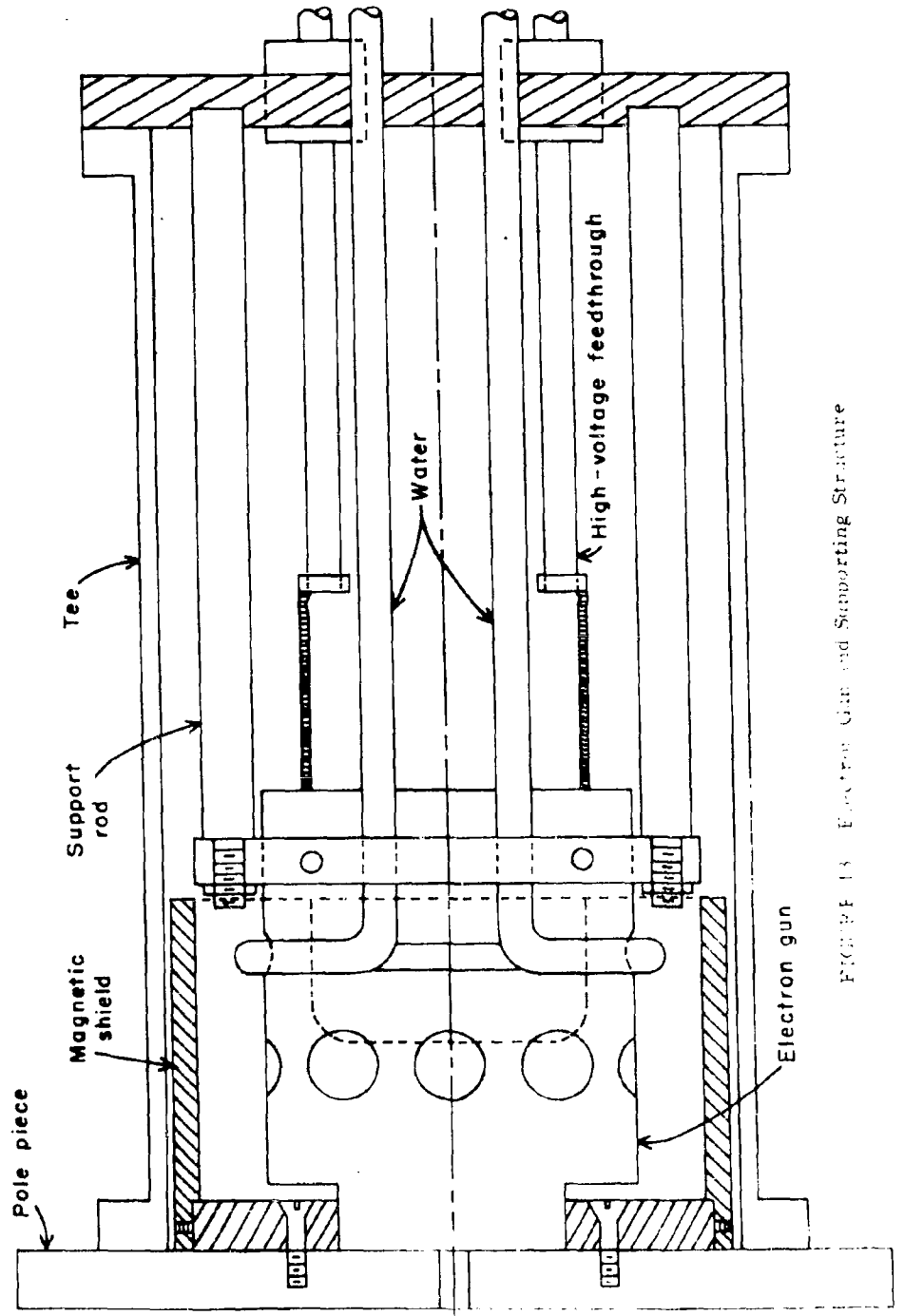


FIGURE 13 Electron Gun and Supporting Structure

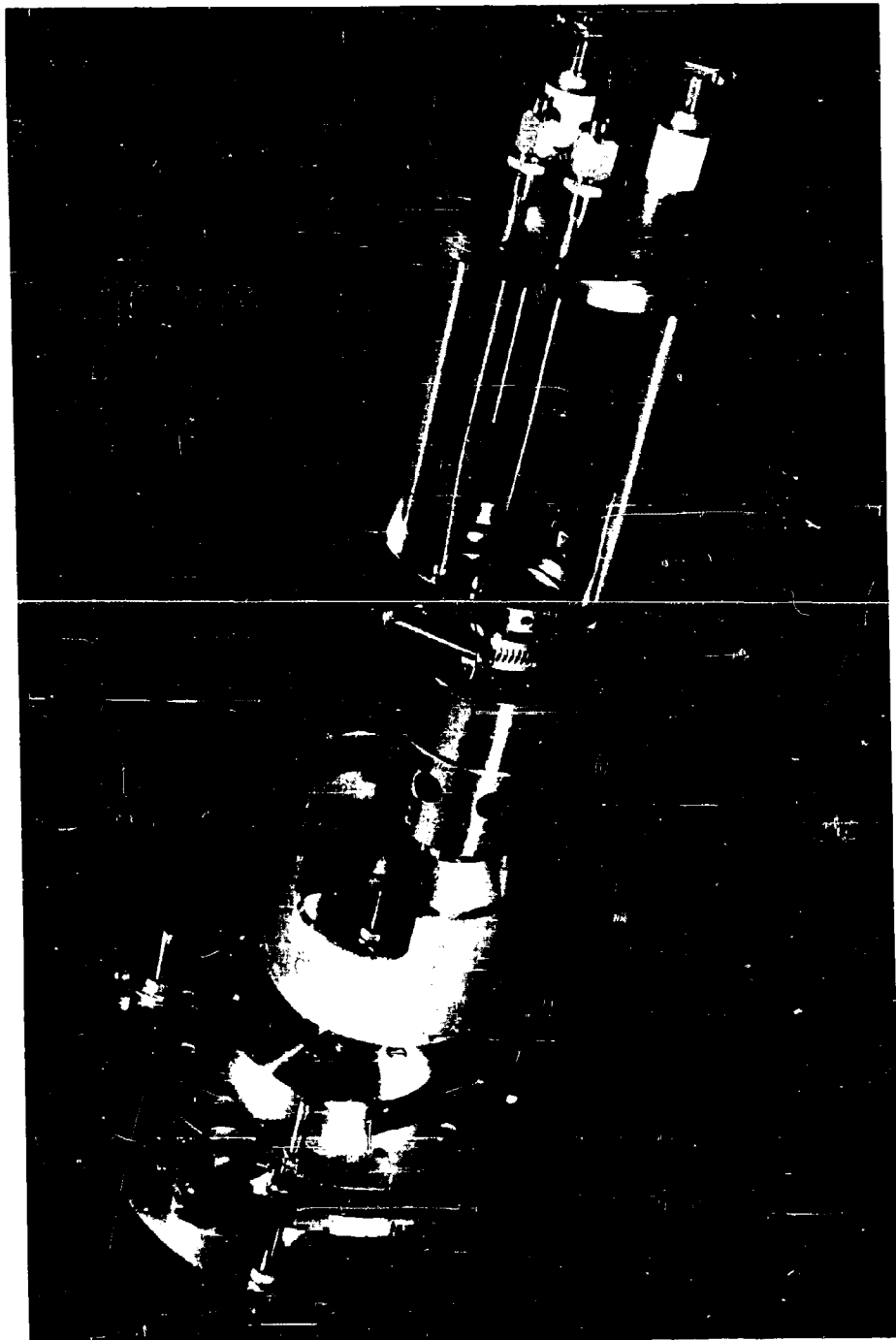


FIGURE 14. Gur. Assembly.

by making a magnetic shield that fitted around the gun, and, by trial and error, choosing the proper length to give the desired ratio of the field strength in the plasma region to the field strength in the gun region. Figure 15 shows the field shape before using the shield, and Figure 16 shows the field shape in the final configuration.

Final construction and assembly of the electron gun proceeded routinely and no unexpected difficulties arose.

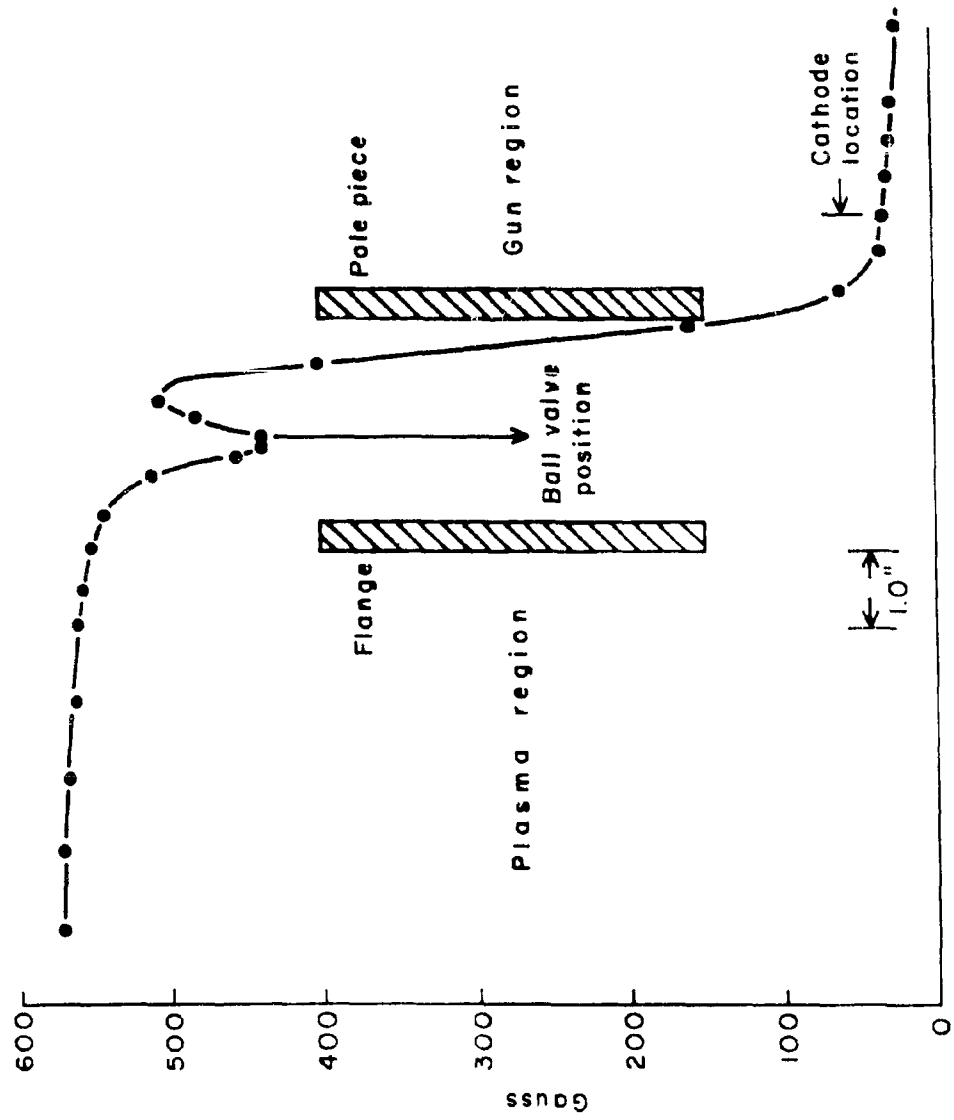


FIGURE 15. Magnetic Focusing Field on Axis of Beam-Plasma System without Magnetic Shield, Solenoid Current 5a

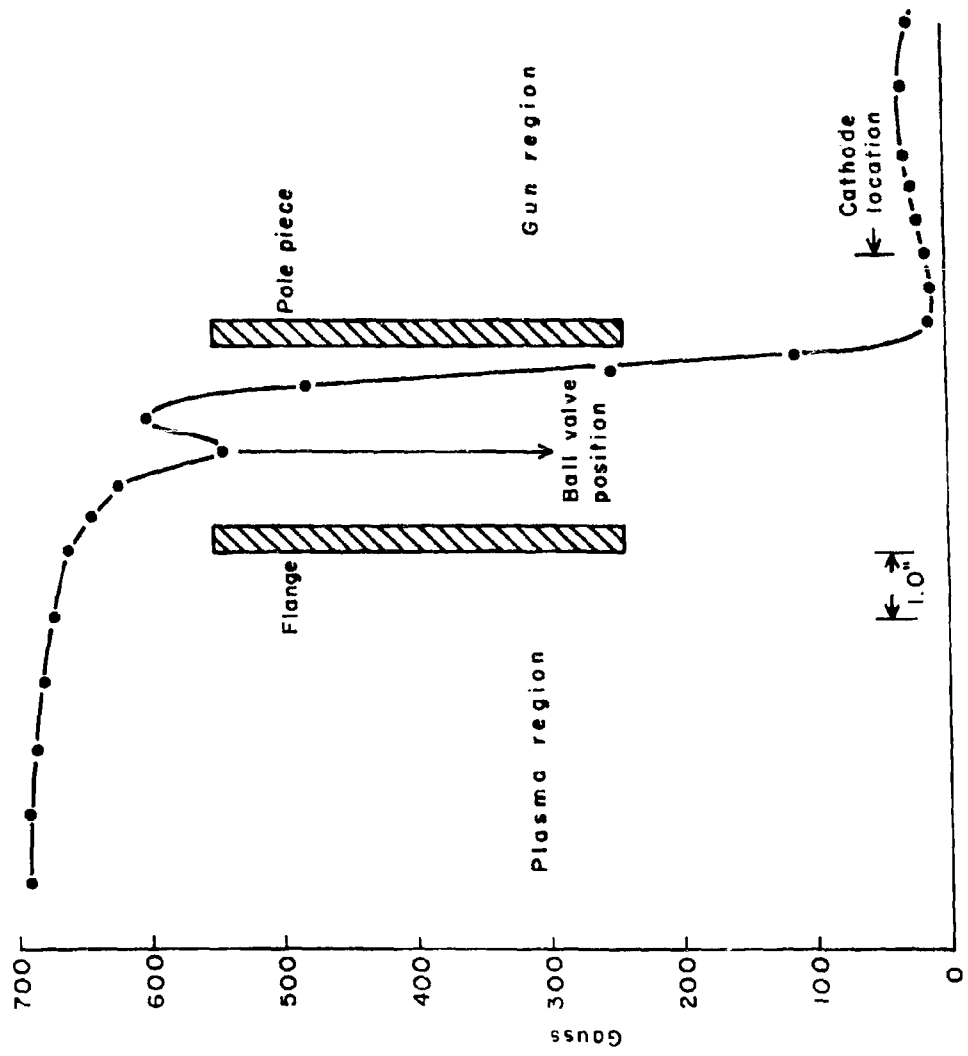


FIGURE 16. Magnetic Focusing Field on Axis of Beam-Plasma System with Magnetic Shield. Solenoid Current = 10 a.

V. BEAM-SCANNING EQUIPMENT

Since it is planned to make careful experimental studies of the electron beam as it leaves the plasma interaction region, provisions were made in the test vehicle to allow positioning of a beam-scanning mechanism directly behind the output plasma cathode by simply removing the copper collector now in use. Removal of the collector was accomplished by loosening the nuts on the ends of the internal plasma subassembly support rods and main support rods, removing the collector detaching a 3 in. extension section of the support rods, and replacing the nuts.

It is intended that the electron beam be scanned as follows:

1. With no plasma discharge and no hydrogen present, to document the initial state of the beam.
2. With hydrogen present but no plasma discharge, to study the beam fluctuations resulting from beam-generated ions; with a plasma discharge present but with no r-f excitation, to study the beam fluctuations further.
3. With a plasma discharge present and with r-f excitation, to understand the gain saturation phenomenon.

In addition to the results directly applicable to this study information will be obtained to allow comparison between the beam-scanning experiments, already completed by Gilmour (see Report C of this report), on a Brillouin-focused beam partially defocused by ions and our experiments under conditions of semiconfined flow.

The beam-scanning mechanism to be used is machined, but not assembled. It is similar to the scanner reported by Gilmour⁴ and a summary follows for convenience. In addition, Figures 21 and 22 indicate the type of information that can be derived from such a scanner.

BEAM SCANNING MECHANISM

1. Control of Faraday Cage Motion inside Vacuum System

A simplified sketch of the part of the beam-scanning mechanism inside the beam tester is shown in Figure 17. Most of the electron beam will be collected by the beam-collecting plate, which is carbonized to reduce the secondary electron ratio. A small portion, however, will be allowed to pass through the 0.010 in. aperture in the center of the plate to a Faraday cage. The electron current from the cage will go out through a coaxial vacuum feedthrough in the bottom control rod to an indicating device outside the tester. The collecting plate will be positioned in the plane perpendicular to the axis of the solenoid by rotations of the two control rods. As shown in the sketch, the plate could be moved horizontally by rotating the bottom rod. Vertical motion could be produced in a similar manner by rotating the side rod. Teflon bearings, which are used to prevent binding between stainless-steel parts, are attached to the back of the plate and slid on the lever arms attached to the side and bottom rods during horizontal and vertical motion. Although rotational motions are converted to translational motions in positioning the cage, they could be considered to be linear, since the distances moved are small compared to the length of the lever arms.

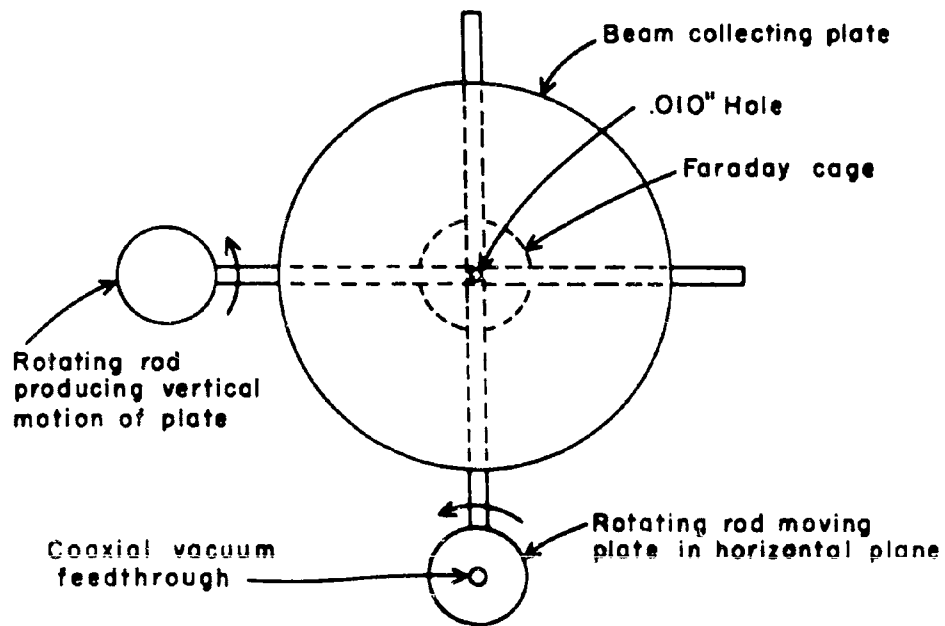


FIGURE 17. Simplified Sketch of Beam-scanning Mechanism inside Beam Tester.

The collecting plate and positioning rods are illustrated in Figure 18. The disk shown behind the collecting plate and the lever arms are used to center the entire mechanism in the drift tube. As shown in Figure 19, this disk is guided by a teflon bearing that rode on a rail in the drift tube and is prevented from touching the drift tube by two spring-loaded teflon blocks. Axial motion of the cage assembly is produced by moving the control rods through the Veeco quick couplings.

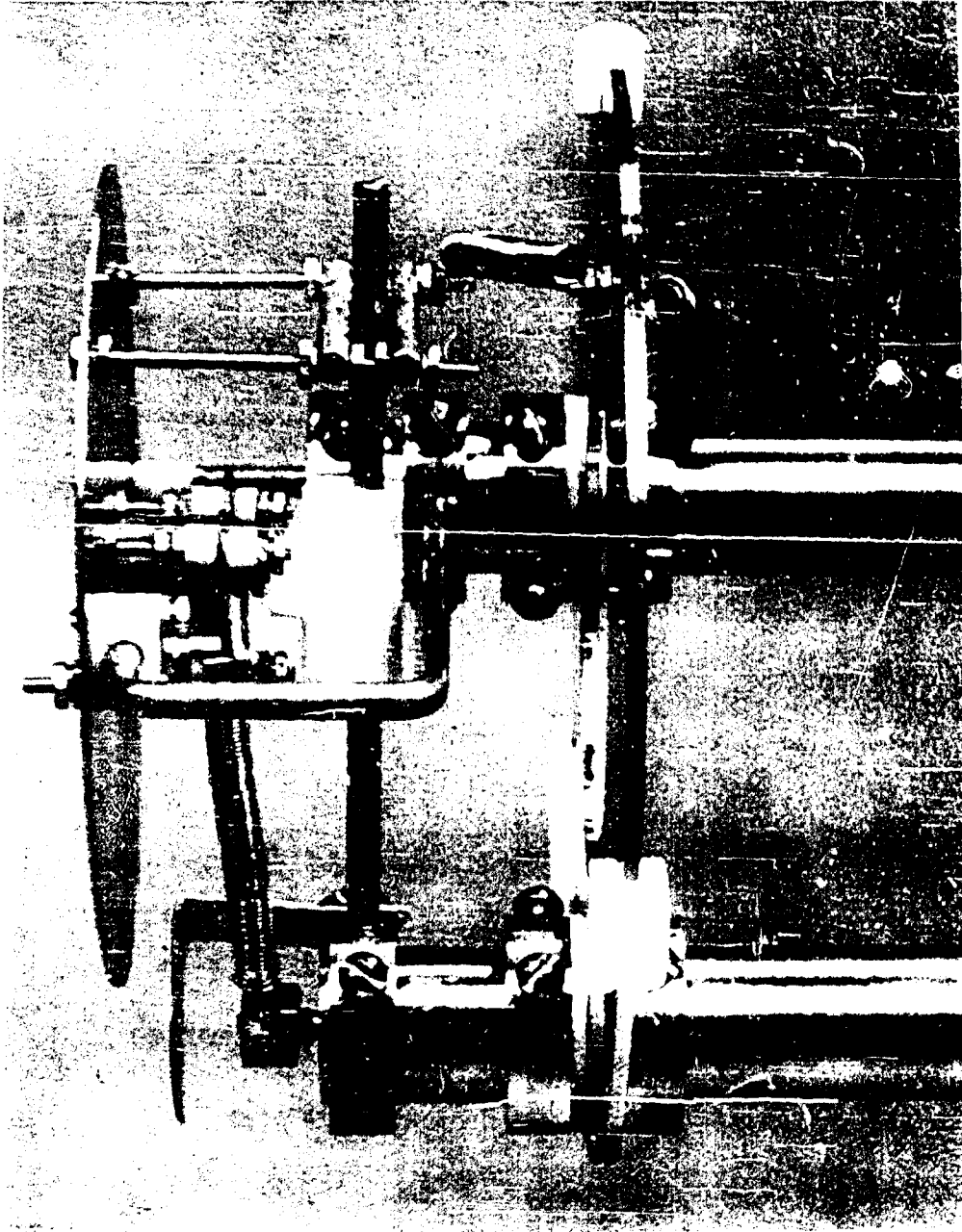


FIGURE 18. Collecting Plate and Positioning Rods.

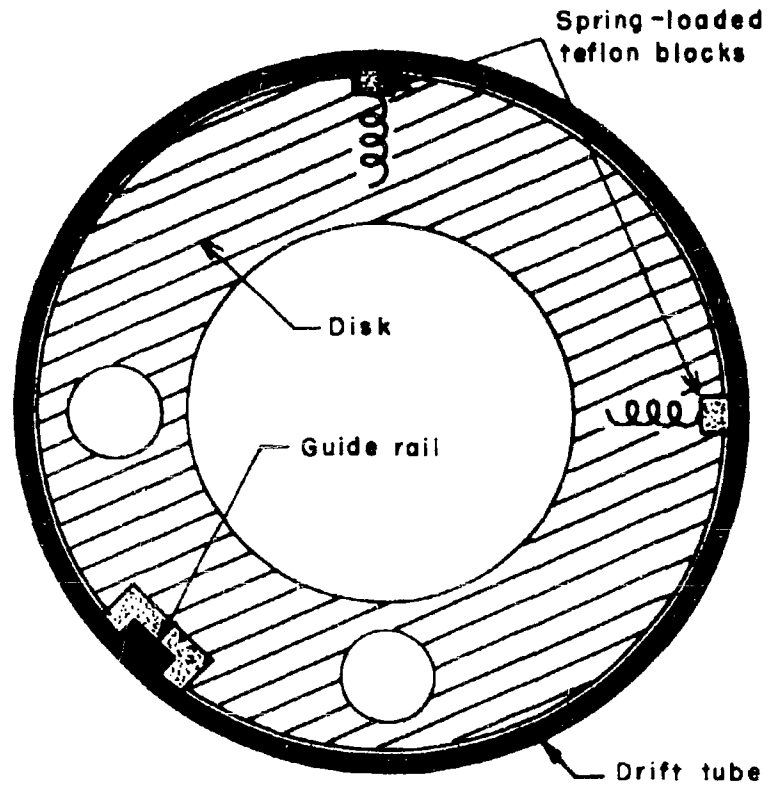


FIGURE 19. Disk Which Centers Faraday Cage Assembly.

2. Control-Rod Positioning Mechanism

The angular position of the control rods is adjusted by means of the micrometers shown in Figure 20. Each micrometer contacts a lever arm at a radius that is twice the radial position of the cage inside the tester; therefore, incremental changes in the cage position are determined by taking one-half the incremental micrometer readings. The

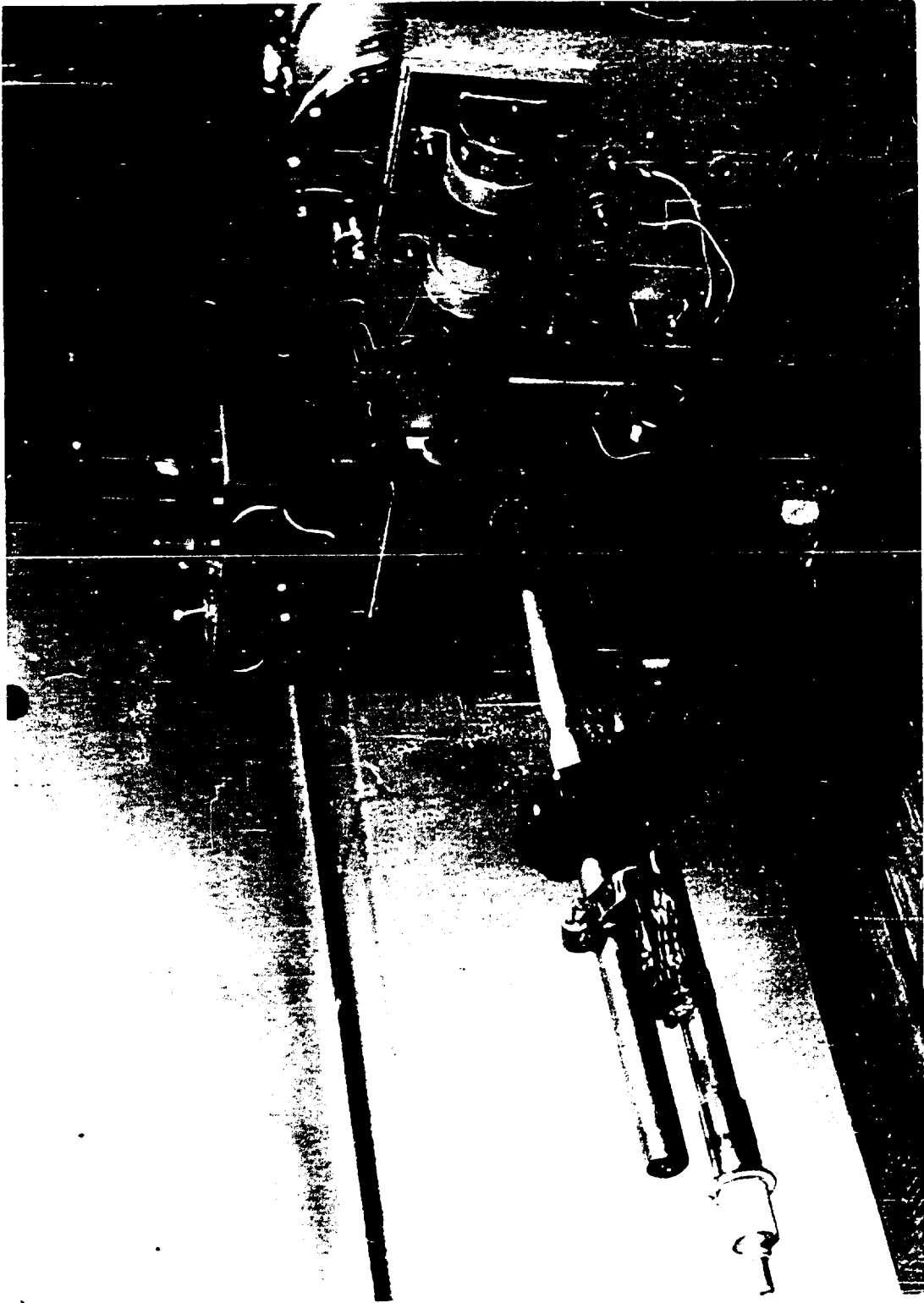


FIGURE 20. Control-Rod Positioning Mechanism.

cage is positioned axially by using a gear-and-rack arrangement. In the first measurements taken on an electron beam by Gilmour,⁴ he positioned both micrometers manually. More than an hour was required to obtain a detailed cross-sectional plot of the current densities in the beam at one axial position. Since it was expected that hundreds of beam cross sections would be needed to determine accurately the scallop wavelength of the beam as a function of the solenoid field and as a function of the beam voltage, a motor drive was attached to the horizontal positioning micrometer. In addition, the automatic reversing switches shown in Figure 20 were installed to force the motor to sweep the Faraday cage back and forth automatically. A ten-turn helipot was geared to the motor to provide a voltage proportional to the horizontal position, and this voltage was applied to the x input of an x - y recorder. The current from the Faraday cage was fed to the y input of the recorder. The vertical position in the beam was indicated in the recorder by changing the y reference position. A typical beam cross section taken in this manner is shown in Figure 21, and Figure 22 shows the variation of beam radius with axial position.

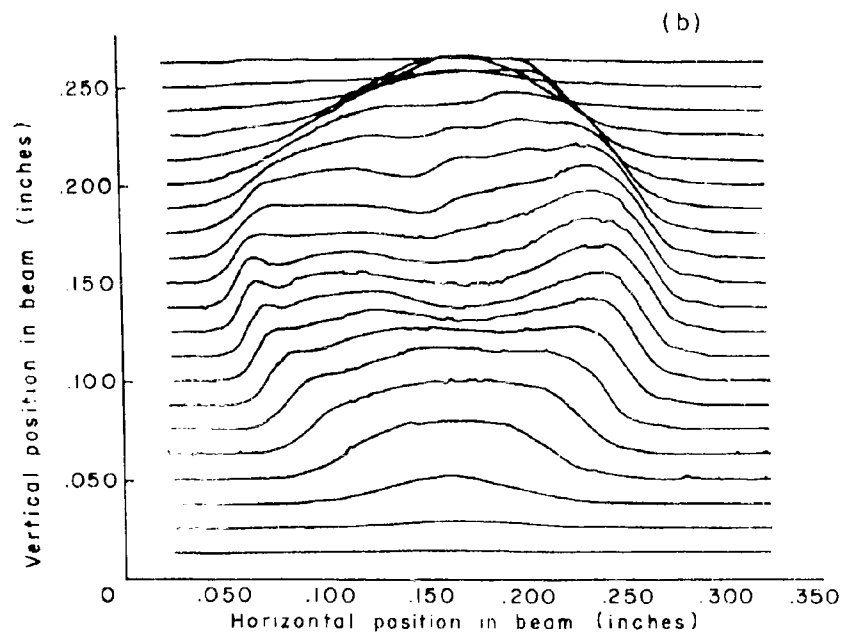
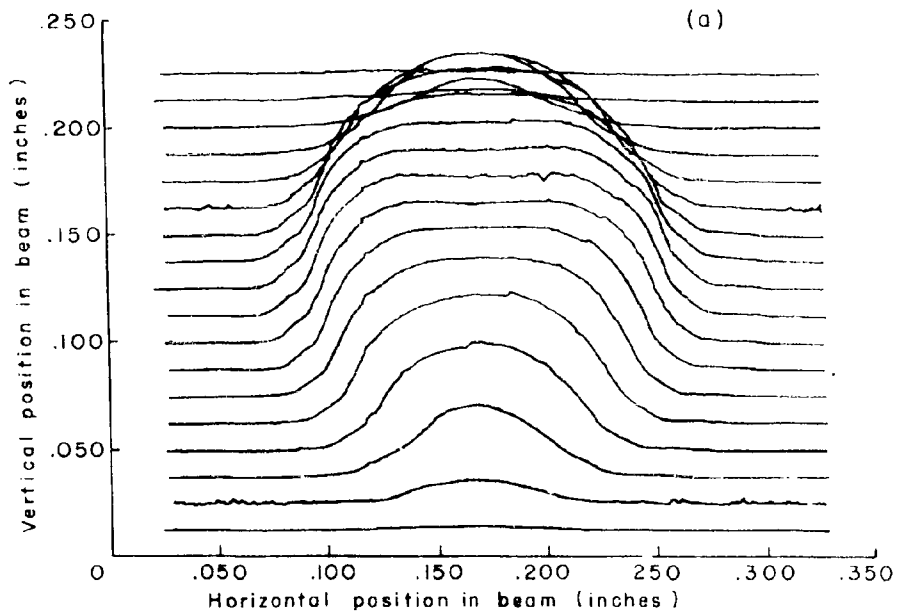


FIGURE 21. Electron Beam Cross Sections Taken under Brillouin Flow Conditions for: (a) No Current through Filament, less than 2% scallop on beam; (b) 7 to 9 Amperes through filament.

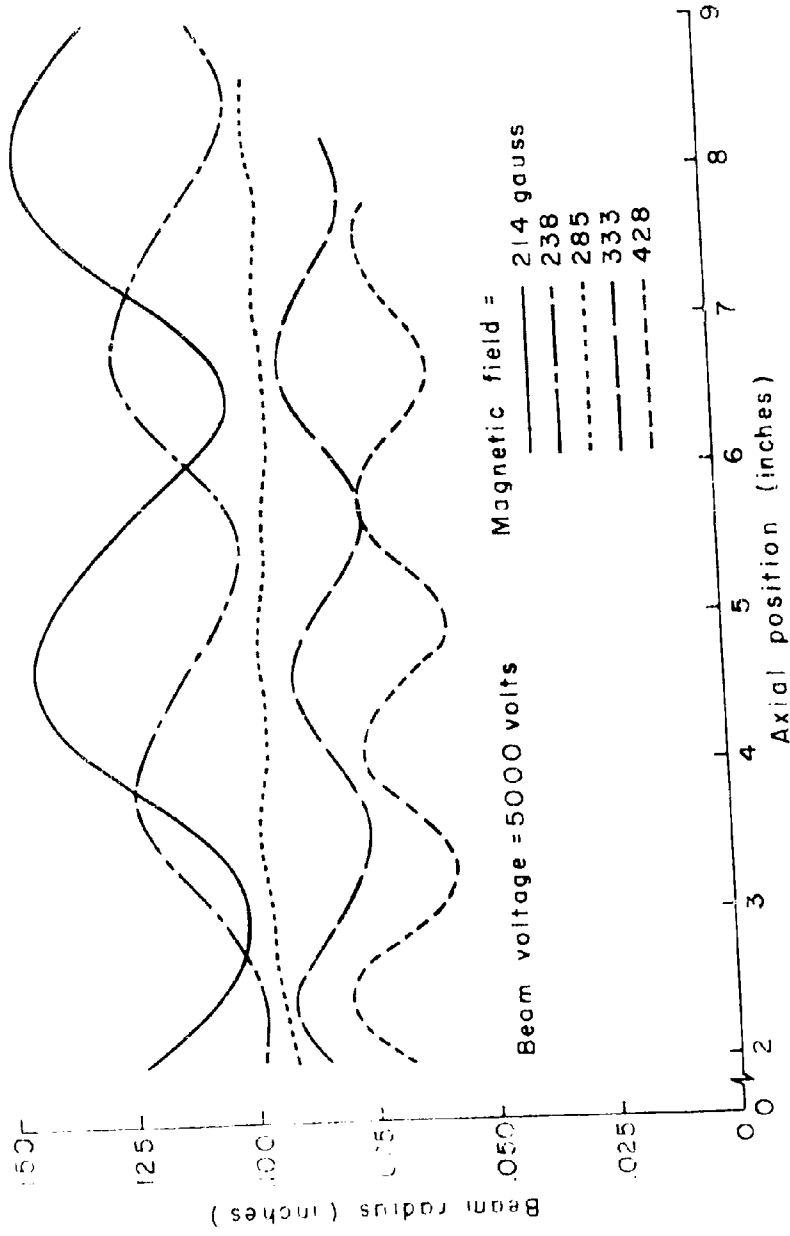


FIGURE 22 Beam Radius vs. Axial Position

VI. EXPERIMENTAL RESULTS

The generation and preliminary diagnosis of the plasma in the internal plasma subassembly, as well as the generation and preliminary testing of the electron beam from the semiconfined flow convergent gun, have been carried out. The microwave cavities were used to diagnose the plasma and to test the electron beam.

The Penning-discharge plasma operated at a nearly constant value of 40 volts and could be varied in density by varying the discharge current from a few milliamps to a few hundred milliamps. The plasma density also could be varied by controlling the hydrogen pressure, which in turn was controlled by a variable hydrogen leak, and by the magnetic field. The hydrogen pressure was over 100 times as great in the plasma chamber as it was in the gun region.

The electron density and collision frequency are found by measuring the frequency shift and change in Q caused by introducing the plasma into the microwave cavity. The equation used to find the electron density and collision frequency are based on a perturbation solution that assumes that the fields in the presence of the plasma are not very different from those of the unperturbed cavity. When the plasma density is low enough for the approximation to be valid, the discharge current, which is proportional to electron density, and the resonant frequency shift have an approximately linear relationship. Figure 23 shows the detuning of the microwave cavity as a function of the discharge current for fixed hydrogen pressure and fixed magnetic field. The relationship is linear, so the perturbation technique will be useful in establishing the operating point of the plasma.

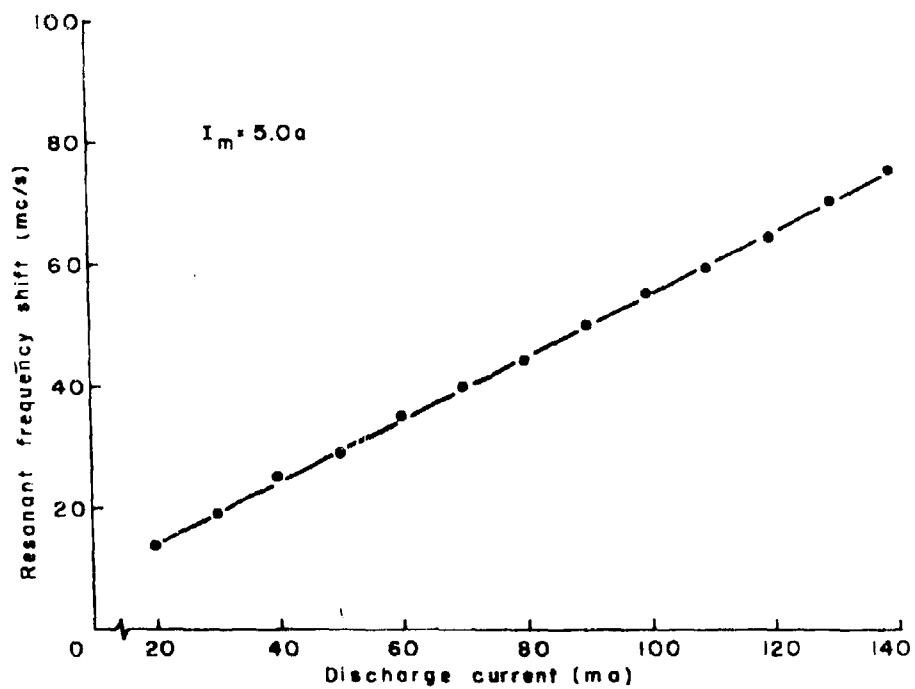


FIGURE 23 Typical Diagnostic Curve for Cavity Detuning as a Function of Discharge Current.

Additional diagnostic data are given in associated Report 3 and show the effect of varying magnetic field. Current voltage characteristics for the discharge at various values of magnetic field are also given there.

The discharge was found to be quite stable and the plasma was easily controlled by varying the discharge current. It was also possible to reset the current so that the cavity detuning was within one or two megacycles of the previously obtained values.

The electron beam operated at 5 kv with a microperveance of approximately unity and operated normally in a solenoid magnetic field with or without hydrogen pressure of up to 10^{-3} mm Hg.

The gain of the amplifier system operating as a klystron has been calculated to serve as a starting point for the investigation. The beam diameter (0.180 in.) was very much smaller than the diameter of the drift tube (0.650 in.). Thus, the coupling to the beam was expected to be low.

The gap coupling coefficient was calculated using the expression,⁵

$$\mu = \frac{I_0^2(\gamma b) - I_1^2(\gamma b)}{I_0^2(\gamma a)} \frac{1}{d^2} \left| \int_{-\infty}^{\infty} F(z) \cos \beta_c z \, dz \right|^2 .$$

$F(z) = E_z/E_m$ is the normalized gap field. All other symbols have their usual meaning. The field distribution was measured experimentally and the integral evaluated graphically, where

d = Drift space length = 5.08 cm ,

b = Beam radius = 0.090 in. = 2.28×10^{-3} m ,

a = Radius of drift tube = 0.325 in. = 8.25×10^{-3} m .

Hence, $\mu^2 = 1.02 \times 10^{-2}$.

The gain of a two cavity klystron amplifier is given by the expression,⁶

$$G = \frac{\mu^4}{16 R_o^2 G_T^2} \left[\frac{\omega^2 \sin^2 z_1}{F^2 \omega_p^2} + \cos^2 z_1 \right]$$

where

$$z_1 = \frac{F \omega_p d}{u_o}$$

$$F = \text{Reduction factor} = \left[1 + \left(\frac{Y}{\beta_e} \right)^2 \right]^{-1/2} = 0.74$$

$$R_o = \frac{V_o}{I_o} \text{ the d-c beam impedance} = 20 \text{ K}\Omega$$

$$G_T = \frac{1}{R_{sh}} + \frac{u^2}{2R_o} = 0.44 \times 10^{-5} \text{ mho}$$

$$R_{sh} = \text{Shunt resistance of the cavity} = 125 \text{ K}$$

$$\omega_p = 3.06 \times 10^9 \text{ c/s}$$

$$(G) \text{ db} = 10 \log G = -24 \text{ db}$$

The klystron gain measured experimentally was -30 db.

VII. CONCLUSIONS

It can be concluded that a test vehicle, having a plasma generating chamber separate from an electron gun chamber, can be constructed to yield more than 100:1 pressure ratios to allow dense plasma, on the one hand, and a low pressure environment for the electron gun, on the other hand, and that high-power convergent gun electron beams operate well under these conditions.

It can also be concluded that a flexible subassembly can be constructed in the plasma chamber to allow the generation of a plasma and input and output direct microwave coupling to a plasma.

It can further be concluded that a beam scanner can be constructed to study an electron beam, sent through a gas atmosphere, for fluctuations, as well as to study the microwave properties of such an electron beam after efficient interaction has taken place.

Finally, it can be concluded that the test vehicle developed can be used effectively to study the interaction of a pulsed electron beam of a few kilowatts with a controlled plasma of a double hot-cathode Penning configuration at 3,000 Mc/s operating frequency.

VIII. REFERENCES

1. S. L. Rutherford and R. L. Jepsen, "Enhanced Hydrogen Pumping with Sputter-Ion Pump," Rev. Sci. Inst., 32 (1961), pp. 1144-1146.
2. "A Beam Generated Plasma System," Report No. NA-8210-8191-1, Great Neck, N. Y.: Sperry Gyroscope (March 1960).
3. A. S. Gilmour, Jr., and D. D. Hallock, "Ion Effects in a Brillouin Beam," Research Report EE 545, Cornell University (October 1962).
4. A. S. Gilmour, "A Beam Tester for Studying the Characteristics of d-c and Velocity-modulated Electron Beams," Research Report EE 495, Cornell University (May 1961).
5. "Electron Beam Coupling in Interaction Gaps of Cylindrical Symmetry," Trans. I.R.E., ED-8 (May 1961), p. 193.
6. A. H. W. Beck, Space-Charge Waves, London: Pergamon (1958), p. 190.

ANALYSIS OF THE INTERACTION
OF AN ELECTRON BEAM WITH A PLASMA

H. Marantz

SUMMARY

The theoretical analysis undertaken in this report has two objectives. First, to understand the physical processes of plasma generation in a low-pressure Penning discharge. Second, to obtain quantitative information on the factors which, independent of external coupling, limit the gain of the beam-plasma interaction.

In the low-pressure double-Penning discharge, particle losses from the system are due more to the effects of free-streaming and electric-field acceleration than to diffusion. This is the case whenever the axial mean-free-path is comparable to the length of the system. The discharge characteristics predicted by this model are much closer to the experimental data than those predicted by the high-pressure model with axial diffusion.

The beam-plasma interaction is handled both qualitatively and quantitatively. The explanation of the interaction mechanism is developed, first from the principles of particle trapping and energy conservation and, then, in terms of the familiar microwave device, the multi-cavity klystron. The interaction is treated quantitatively by using appropriate integrals of the Boltzmann equation to describe the microwave characteristics. This information, together with Maxwell's equations, form a closed set of equations from which the fields are obtained. The analytical approach for solving the eigenvalue problem is formidable for all but the simplest

approximations. We have closed-form solutions for these, and numerical results were obtained for the remaining cases with a digital computer.

Analysis of the interaction, using a simple one-dimensional model, showed that extremely high (> 100 db/cm) gain was possible. The results include the effects of finite-transverse-inhomogeneous beam-plasma cross section, magnetic field, plasma collision, and plasma-electron temperature. These conditions are all present in a real plasma and serve to limit the gain to about 10 db/cm at S-band frequencies. Although this is an order of magnitude less than that predicted by the simplest model, it is still higher than existing devices at these frequencies.

PLASMA DIAGNOSTICS

D. M. Kerr

SUMMARY

Two singly re-entrant cavities of the type ordinarily used in klystron amplifiers were designed and tested for use in the electron-beam hydrogen-plasma system. They were designed primarily for use as the input and output coupling structures of the beam-plasma amplifier, but they also are used to investigate the properties of the plasma discharge, in particular, to determine the electron density and collision frequency.

The design and cold tests of the cavities are described, and comparisons are made between theoretical and experimental values. A theoretical discussion of cavity Q in the presence of coupling losses is included, since the measurement of cavity Q is important in diagnosing the plasma. A perturbation technique was used to determine the quantity, $\mu^2 R_{sh}/Q_0$, which is important in considering coupling to the system.

The general theory of the cavity perturbation is given and equations are obtained relating the shifts in resonant frequency and Q to the average electron density and collision frequency. The possible disadvantages of this type of measurement are discussed briefly and then preliminary data is presented. A linear relationship between resonant frequency shift and discharge current is found, as predicted, and, in the range of discharge currents expected in the beam-plasma amplifier, this type of diagnostic technique appears to be successful.

ION-INDUCED OSCILLATIONS OF ELECTRON BEAMS

A. S. Gilmour, Jr.

SUMMARY

In this study, the ion-induced oscillations of a pulsed, convergent flow, Brillouin beam were measured in detail for pressures of hydrogen gas from 10^{-8} Torr to 10^{-3} Torr. The beam passing through the hydrogen was .20 in. in diameter and had .40 a current for 5 kv. The beam dynamics, as they depended on time during the pulse, were measured, using a beam scanner that was able to measure the beam current-density at any transverse location and over a considerable length of the beam. Associated test equipment allowed sampling of any desired portion of the time pulse. The experimental results, showing definite transverse and radial ion-induced electron-beam oscillations, are given in detail and explained. The transverse oscillations occurred at the lower pressures and increased with time during the pulse. The radial oscillations occurred at the larger pressures and also increased with time during the pulse. It was concluded that the feedback mechanisms for these two forms of oscillation are the charged particles moving from the drift region back toward the gun region and affecting the beam-formation conditions there.

Earlier work by Mihran and Agdur is discussed and extended, and the theoretical work of Peterson and Puthoff is extended to explain the oscillation build-up.

Ways of controlling or eliminating these oscillations are deduced and explained.

ANALYSIS OF THE INTERACTION
OF AN ELECTRON BEAM WITH A PLASMA

H. Marantz

ACKNOWLEDGMENTS

The author would like to thank Professor L. F. Eastman for his guidance and encouragement throughout the course of this work, and Professor R. N. Sudan for the lecture series he gave on plasmas.

He is indebted to the members of the computing center for their assistance in programming, and to the publications staff for editing and typing this thesis.

This work was made possible under the sponsorship of the U. S. Air Force under Contract No. AF30(602)-2833.

ABSTRACT

A detailed analysis is made of the gain characteristic of the beam-plasma amplifier. The first section is a study of the general specification of a plasma and of the d-c plasma discharge in particular. It is found that the analysis of the low-pressure Penning discharge must take particle streaming under consideration to account for the discharge current and the percentage of ionization.

The second section analyzes several mechanisms for broadening the gain characteristic of an infinite beam plasma. It is concluded that the beam-plasma inhomogeneities account for the greatest change in the gain characteristic. Corrections for plasma collisions and temperature can be neglected for the experimental values expected.

TABLE OF CONTENTS

	Page
ABSTRACT	iv
LIST OF IMPORTANT SYMBOLS	viii
LIST OF FIGURES	vii
I. INTRODUCTION	1
II. CHARACTERISTICS OF A PLASMA	5
A. GENERAL CHARACTERISTICS	5
B. THEORY OF THE PLASMA DISCHARGE	7
III. THEORY OF THE INTERACTION	16
A. PHYSICAL EXPLANATION	16
B. MATHEMATICAL DESCRIPTION	18
1. General Equations	18
2. Effects of Geometry and Magnetic Field	22
3. Effects of Beam-Plasma Inhomogeneity	33
4. Effects of Collisions and Nonzero Plasma Temperature	36
a. Collisions	36
b. Plasma Temperature	39
C. CALCULATION OF POWER GAIN AND PHASE SHIFT	41
1. Experimental	41
2. Theoretical	43
IV. CONCLUSIONS	46
V. REFERENCES	47

	Page
APPENDIX A. BOLTZMANN AND BOLTZMANN TRANSPORT EQUATIONS	50
APPENDIX B. DERIVATION OF POISSON'S EQUATION	52
APPENDIX C. COMPUTER PROGRAM FOR THE INHOMOGENEOUS CASE	59
APPENDIX D. CORRECTION TERM FOR MAXWELLIAN DISTRIBUTION IN LONGITUDINAL VELOCITY	71

LIST OF FIGURES

Figure		Page
1	Vacuum System and Associated Components of Beam-Plasma Amplifier.	3
2	Plasma-forming Subassembly.	4
3	Plasma Cross Sections.	12
4	Dispersion Diagram for a Homogeneous Beam-Plasma Media.	27
5	Gain Dependence on Magnetic Field (Power Gain = $8.6 \frac{\omega_{pb}}{v_0} R_2$ db/cm).	30
6	Gain Dependence on Beam Density.	31
7	Gain Dependence on d_3 .	32
8	Inhomogeneous Beam-Plasma Cross Sections.	35
9	Gain Dependence on Beam Width.	35
10	Gain Dependence on Plasma Width.	37
11	Gain Dependence for a Hollow Beam.	38
12	Gain Dependence on Plasma Collisions.	40
13	Gain Dependence on Plasma Temperature.	42
14	Measurement (a) of Power Gain and (b) of Phase Shift.	44

LIST OF IMPORTANT SYMBOLS

A. GREEK

α	normalized frequency parameter
β	longitudinal propagation constant
β_e	electron beam propagation constant
β_o	free space propagation constant
λ	d-c discharge time constant
β_T	thermal propagation constant
γ	normalized velocity spread parameter
λ_{90}	mean-free-path between strong collisions
ν_c	plasma collision frequency
ρ	space charge density
ϕ	quasi-static potential
ω	frequency

B. ROMAN

d_i	first partial derivative with respect to the variable i
d_1	normalized electron cyclotron frequency
d_2	normalized beam plasma frequency
d_3	normalized beam velocity and radial parameter
d_4	normalized plasma collision frequency
f	velocity distribution function
h	Debye length

p	critical impact parameter
n	particle density
v	velocity
B	magnetic flux density
D	diffusion constant
E	electric field strength
H	magnetic field strength
L	length of plasma discharge vehicle
R	beam-plasma reduction factor
R_2	imaginary part of beam-plasma reduction factor
V_D	plasma discharge voltage

C. GENERAL COMMENTS

∇ del operator

Single subscripts are used to indicate either particle type, or whether the parameter is a function of time. Double subscripts indicate both of these factors. The first subscript is used for time dependence, the second for particle type.

I. INTRODUCTION

Interest in plasmas started in 1902 with Heaviside's postulation of an ionized layer above the earth. Since then, two major fields of interest have developed: first, the use of a plasma as an energy converter, e. g. , thermonuclear machines and ion-propulsion guns; and second, the use of a plasma as a wave-propagating medium, e. g. , magneto-ionic theory and the production of shock and electromagnetic waves in a plasma.

We are concerned with using a plasma to amplify and generate communication signals at about 3 Gc/s. The possible advantages of using a plasma are fourfold: (1) it allows propagation of power at high frequencies, where metallic slow-wave structures are difficult to construct; (2) it has strong interaction with an electron beam, yielding high electronic gain per centimeter of drift length; (3) electronic tuning of the plasma is possible; and (4) the nonlinear properties of the plasma could be used in frequency multiplying applications.

Pierce¹ was one of the first to think of using a plasma in a practical device for microwave amplification. The basic interaction theory was developed in papers by Bohm and Gross,² Haeff,³ and Pierce.⁴ More recently, the analysis has been extended by Trivelpiece,⁵ Paik,⁶ Chorney,⁷ and Bers⁸ to include the effects of finite geometry. The theory of the double stream instability for a nonzero temperature plasma has been discussed by E. A. Jackson,⁹ J. D. Jackson,¹⁰ and Kellogg and Limohn.¹¹

In this study, a Penning discharge device and a microwavetube electron gun were placed back to back (see Figures 1 and 2). This discharge, by using a confining axial magnetic field, generated high plasma densities at relatively low gas pressures. The electron gun used semiconfined focusing to send a 5-kv, .4-a (10- μ s pulsed) beam through the plasma region. Microwave signals were directly coupled to and from the beam-plasma region by using singly re-entrant klystron cavities.

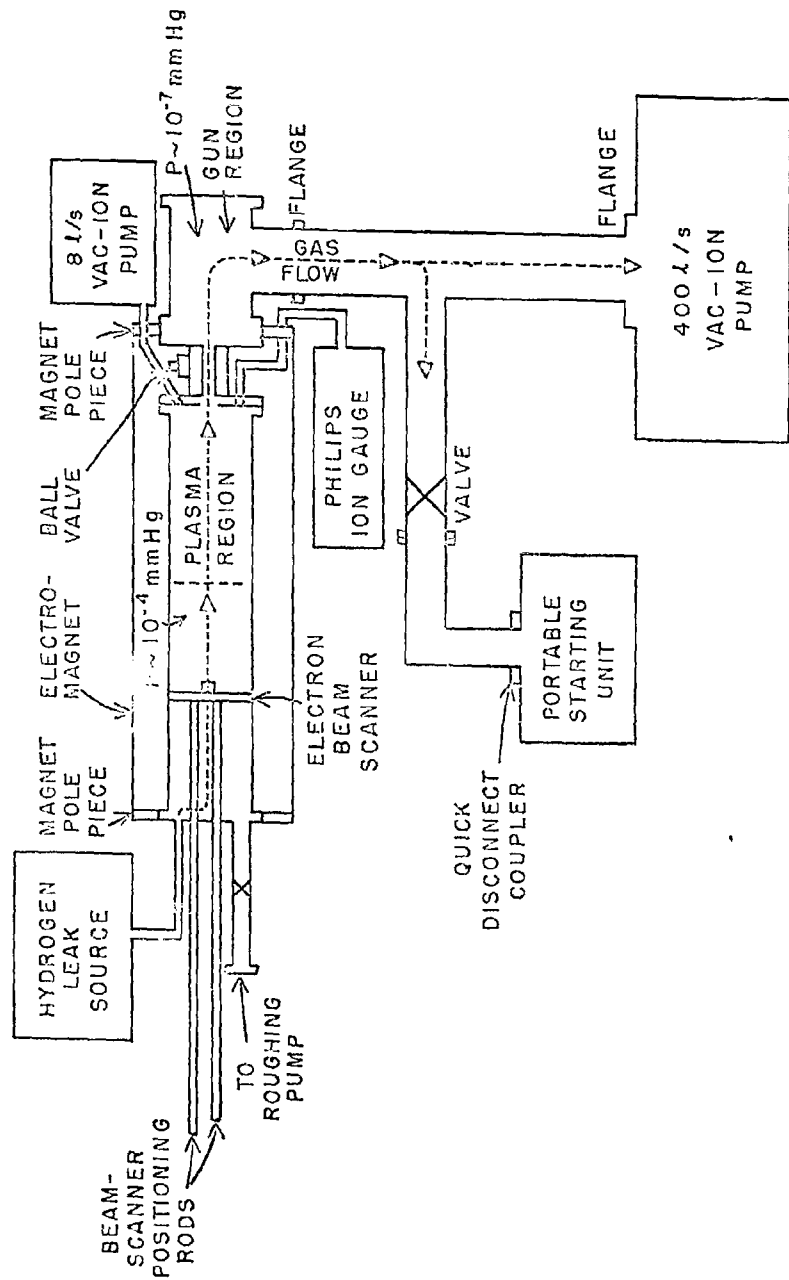
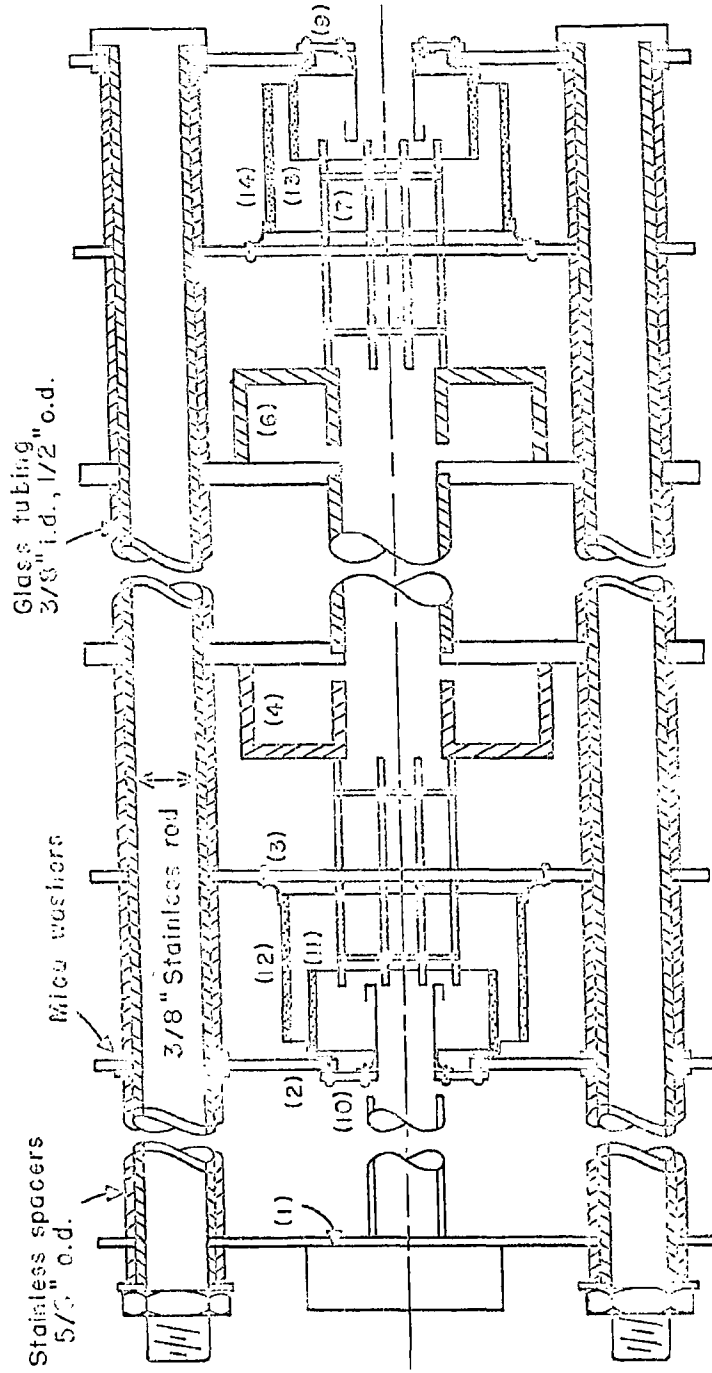


FIGURE 1. Vacuum System and Associated Components of Beam-Plasma Amplifier.



Key: (1) Collector ; (2) Left cathode ; (3,7) Mesh anode to allow viewing of plasma ;
 (4) Output cavity ; (5) Anode "spool", 2" drift space ; (6) Input cavity ; (8) Right cathode ;
 (9,10) Back electron shield ; (11,13) Heat shield on cathode plate ; (12,14) Heat shield
 on anode plate.

FIGURE 2. Internal Plasma Subassembly.

II. CHARACTERISTICS OF A PLASMA

A. GENERAL CHARACTERISTICS

A plasma is an ionized gas in which the positive particle density is approximately equal to the negative particle density. Plasmas occur in nature (sun's corona, earth's ionosphere) and in man-made devices (arc discharges and flame of Bunsen burner). There are four parameters that determine the assumptions to be made in our analysis. First, the Debye length h must be considered. This is the shielding distance for the potential resulting from a single charged particle. Therefore, even though we assume equal numbers of positive and negative charges, potentials still exist for distances of the order of the Debye length, which is given by

$$h_i^2 = \frac{kT_i}{(4\pi n_i q_i^2)} \quad (2.1)$$

Second, the average distance between charged particles d is

$$d = (2n)^{-1/3} \quad (2.2)$$

Third, the average critical-impact parameters for the collision of two charged particles P_{oi} is defined as that impact parameter which results in a scattering angle of $\pi/2$. For the coulomb potential, we get

$$P_{oi} = \frac{q_i^2}{3kT_i} \quad (2.3)$$

The fourth parameter is the average mean-free path between strong charged-particle collisions λ_{90} . If we use a coulomb potential, we get

$$\lambda_{90} = (\pi n_i P_{oi}^2)^{-1} \quad (2.4)$$

When the Debye length is much smaller than a typical dimension of our geometry, we know that in the absence of strong external fields, the plasma volume can be assumed to be electrically neutral. When $P_o \ll d$, the close collisions are strictly two-particle collisions. This justifies using the coulomb or modified coulomb potential in calculating the effects of plasma collisions. If $P_o > d$, the concept of a distinct two-particle collision must be replaced by that of collective interaction, and the effects of collisions cannot be easily isolated. For $d \ll \lambda_{90}$, the effective mean-free path (distance between deflections of ninety degrees or more) is long. The expansion of the collision term in terms of small-velocity changes leads to the Fokker-Planck Equation.¹² In order to determine the d-c properties of the discharge, we must know the particle density and the root-mean-square particle velocity. For the microwave properties, we must be able to calculate the r-f current and space-charge density. The approach used to get these quantities depends on the time scale for which the information must be valid.

i) During a collision, we use the BBKGY relations. These equations are derived by taking successive moments of Liouville's equation with respect to the velocity of each particle. For a plasma with

n negative particles, this involves $2n$ coupled differential equations.

ii) Between collisions, we use Boltzmann's equation; this involves only two coupled differential equations.

iii) After several collisions, we use the moment equations that are derived from Boltzmann's equations. There are four of them, but we have three fewer independent variables than in item ii. Typically, the times for this experiment are:

10^{-15} s for collision time,

10^{-7} s for the time between collisions,

10^{-9} s for the r-f time of interest,

10^{-5} s for the d-c time of interest .

We shall therefore use the Boltzmann transport equations to describe the d-c discharge and the Boltzmann equation to describe the microwave phenomena. These equations are derived in Appendix A.

B. THEORY OF THE PLASMA DISCHARGE

A low-voltage, hydrogen-plasma (thermionic) discharge was used, the geometry of which is shown in Figure 2. The cathode electrons were accelerated by the cathode-anode potential, so that they had an energy greater than the ionization potential when they passed through the center. Since these electrons collide with the neutral molecules, they never return to the cathodes and must eventually reach the anode. Some of these give up their energy in ionizing collisions before being

collected by the anode. The plasma of electrons and H_2^+ thus created will "diffuse" away from the point of ionization, the ions going to the cathode, the electrons to the anode. The term "diffuse" is used because it is not diffusion in the usual sense that governs the longitudinal flow of particles in our system. When the system pressure is low enough that the particle mean-free path is of the same order of magnitude as a typical dimension of the confining structure, particle streaming and electric-field acceleration must be taken into account. Simon¹³ has used these terms to explain anomalous diffusion in arc plasmas. The equations governing the discharge are (see Appendix A):

$$d_+ n_+ = I_+ - \nabla \cdot \left[-\underline{D}_+ \cdot \nabla n_+ + \underline{\mu}_+ \cdot \underline{E} n_+ \right] - \frac{v_{+||} n_+}{L} - \frac{e E_{||}}{m_+ v_{+||}} \quad (2.5)$$

$$d_+ n_- = I_- - \nabla \cdot \left[-\underline{D}_- \cdot \nabla n_- + \underline{\mu}_- \cdot \underline{E} n_- \right] - \frac{v_{-||} n_-}{L} + \frac{e E_{||}}{m_- v_{-||}} \quad (2.6)$$

$$\nabla \cdot \epsilon_0 \underline{E} = e(n_+ - n_-) \quad (2.7)$$

In equations (2.5) and (2.6), $-v_{-||} n_- / L$ represents the free streaming effects and $e E_{||} / m_- v_{-||}$ the electric-field acceleration effects. Note that these effects are not important in the transverse direction because of the strong magnetic field required to confine the electron beam. Therefore, we do not include the transverse components of these terms in Equations (2.5) and (2.6). Conversely, because

of the long axial mean-free path at low pressures, the axial diffusion terms do not apply. If we calculate the highest possible electric field that could be present in the plasma in the absence of oscillations, we find

$$E_{\max} \approx 10^4 \text{ v/m}$$

Using Gauss's law, we calculate the maximum deviation from a neutral plasma, which is

$$\int \underline{E} \cdot dA = \frac{e}{\epsilon_0} (n_+ - n_-) \quad (2.8)$$

Assuming a radial electric field about some point, we can integrate over an infinitesimal sphere, to get

$$n_+ - n_- = E_{\max} \frac{\epsilon_0}{e} \approx 10^{12} \text{ m}^{-3} \quad (2.9)$$

Since we are dealing with plasma densities on the order of 10^{17} m^{-3} , we may set $n_+ = n_-$ throughout the plasma, though not to compute a local electric field. Furthermore, using the Einstein relation to compare the relative particle flow resulting from diffusion and mobility, we see that the mobility contribution is negligible. We have neglected volume recombination. With these assumptions, Equations (2.5) and (2.6) become

$$d_+ n = I_+ - D_{+||} \nabla_t^2 n - \frac{v_{+||}}{L} - \frac{eE_{||}}{m_+ v_{+||}} \quad (2.9)$$

$$d_- n = I_- - D_{-||} \nabla_t^2 n - \frac{v_{-||}}{L} + \frac{eE_{||}}{m_- v_{-||}} \quad (2.10)$$

Multiply Equation (2.9) by $m_+ v_{+||}$, Equation (2.10) by $m_- v_{-||}$, and add

$$d_+ n = \left[\frac{m_+ v_{+||} I_+ + m_- v_{-||} I_-}{m_+ v_{+||} + m_- v_{-||}} \right] + \left[\frac{m_+ v_{+||} D_{+||} + m_- v_{-||} D_{-||}}{m_+ v_{+||} + m_- v_{-||}} \right] v_t^2 n - \left[\frac{m_+ v_{+||}^2 + m_- v_{-||}^2}{m_+ v_{+||} + m_- v_{-||}} \right] n \quad (2.11)$$

By setting the left-hand side of Equation (2.9) equal to zero, calculating I_{+1}, I_{-1} , and assuming appropriate boundary conditions, we could solve for the exact steady-state solutions. We can obtain much information, however, using much simpler calculations and heuristic reasoning. Most of the ionizations take place in the volume connecting the two plasma cathodes. The originally empty inner cylinder becomes filled with plasma by transverse diffusion. If we neglected the axial particle motion, we could assume that the particle density was constant across the inner cylinder diameter. In fact, Chorney et al., using a pair of annular cathodes under much the same conditions as ours, have observed that the plasma light intensity was lowest in the center. This does not necessarily mean that the inner cylinder has a lower electron density, but that the ratio of fast to slow electrons is smaller there. Chorney¹⁴ later noted that a discharge instability occurred at high magnetic fields. This effect has been analyzed by Kadomtser et al.¹⁵ They found that the instability was associated with the growth of a low-frequency θ -dependent mode. In Chorney's experiment, the plasma was enclosed by glass walls; therefore the excitation of an

axially unsymmetric mode was much more probable than in our own case. Therefore we do not expect a critical magnetic field that would be low enough to interfere with good electron beam focusing. Figure 3 shows the particle density cross section calculated using a one-dimensional model. Also shown there are some analytical expressions that could be used to approximate this distribution profile. For d-c calculations the approximation using the series

$$\frac{n}{n_0} = \sum_i C_i J_0(b_i r) \quad , \quad (2.12)$$

where J_0 is the zero order Bessel function of the first kind, is very useful. Setting $I_+ = I_- = 0$ in Equation (2.11), we can calculate the amount of discharge current. Solving Equation (2.11) by separation of variables and neglecting all but axially symmetric modes, we find that the terms in the solution are of the form,

$$n = n_{oi} e^{-\lambda_i t} J_0(b_i r) \quad , \quad (2.13)$$

where

$$\lambda_i = b_i^2 \left[\frac{m_+ v_{+||} D_{+t} + m_- v_{-||} D_{-t}}{m_+ v_{+||} + m_- v_{-||}} \right] + \frac{[m_+ v_{+||}^2 + m_- v_{-||}^2]}{L[m_+ v_{+||} + m_- v_{-||}]} \quad . \quad (2.14)$$

The n_{oi} are determined by the initial (steady-state) configuration. The current is given by

$$I = 2 \int n dv \left[1 - \frac{1}{\epsilon} \right] e \lambda (b^2) \quad (2.15)$$

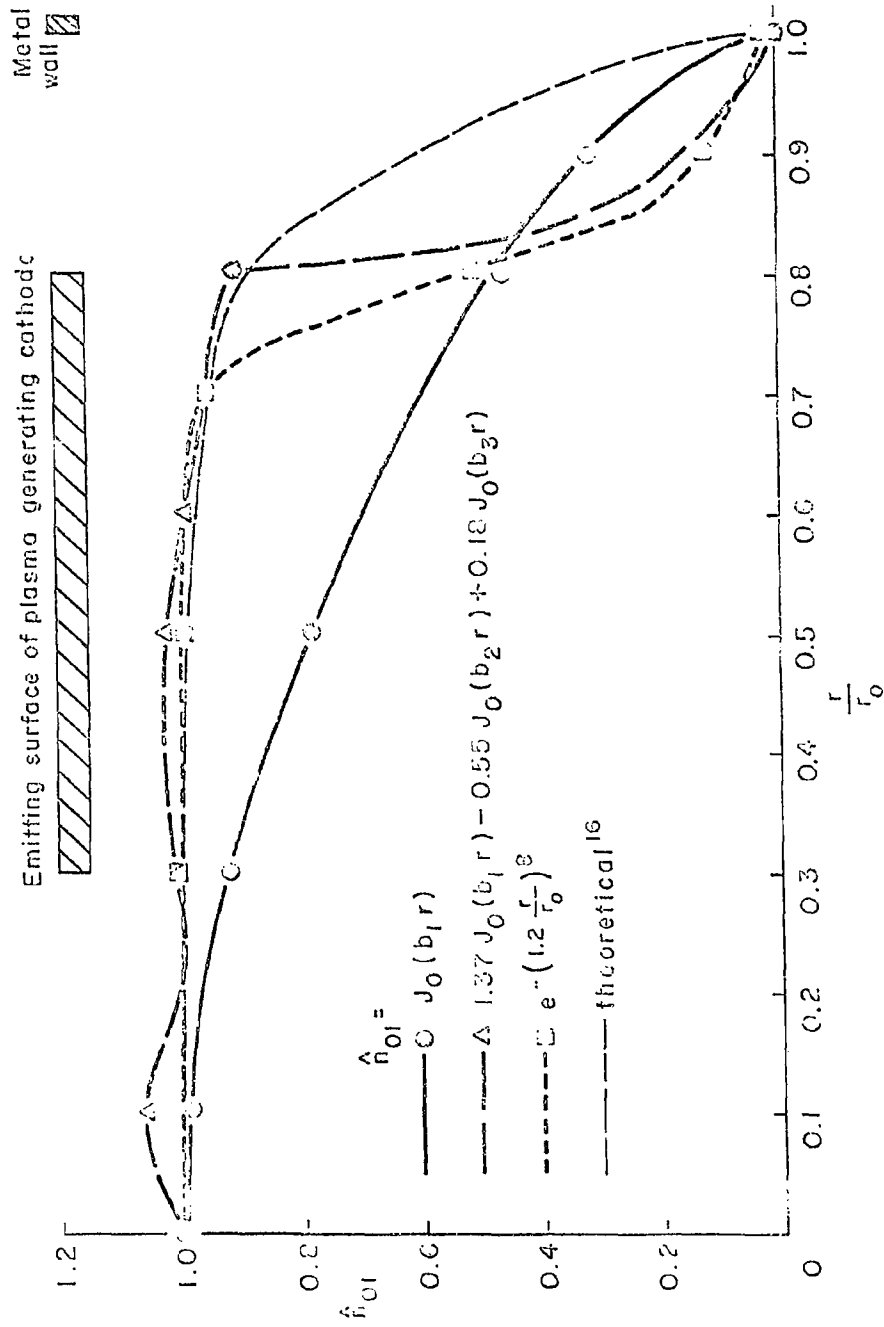


FIGURE 3. Plasma Cross Sections.

$$\overline{b^2} = \frac{\sum_i n_{oi} b_i^2}{\sum_i n_{oi}} \quad (2.16)$$

Implied in this derivation is the assumption that the presence of ionization processes will not significantly change the rate at which particles leave the system. There will not be large gradients in the spatial distribution of neutral particles, so that the minimum pressure that will supply all the charged particles is given by

$$p_{\min} = n_o k T_N \times .75 \times 10^{-3} \text{ mm Hg (cgs)} \quad (2.17)$$

The actual pressure is calculated, knowing P_o , the probability of ionization per centimeter per millimeter of mercury, the mean electron velocity, and the time it takes a fast electron to leave the system:

$$p = \frac{\bar{\lambda}}{P_o \bar{v}}$$

$$\text{percentage of ionization} = \frac{P_{\min}}{p} \times 100 \quad (2.18)$$

For work on hot plasmas, it is desirable to know the ratio between fast and slow electrons, so that the electron velocity distribution can be approximated. First, we calculate a transverse electron drift velocity by considering the initial position of the last set of electrons to reach the anode after $1/\lambda$ seconds. The ratio of the time the electron spends as a fast electron to that as a slow electron gives us the ratio of number of fast to number of slow electrons in the volume.

Using values expected in our experiment, we should be able to predict, to within an order of magnitude, discharge current, percentage of ionization, and the ratio of fast to slow electrons.

Using the discharge geometry of Figure 2 and the cross-section of Figure 3, we compute a typical set of discharge parameters. Given

$$\begin{aligned}
 V_D &= 15 \text{ v} \\
 \omega_{PF} &= 2\pi \times 3 \text{ kmr/s} \\
 \omega_{ce} &= 2\pi \times 2.25 \text{ kmr/s} \\
 v_c(V_D) &= 10^7 \text{ kmr/s} \\
 r_o &= .75 \text{ cm} \\
 L &= 10 \text{ cm} \\
 T_N &= 10^3 \text{ K} \\
 b^2 &= 2 \times 10^4 \text{ m}^{-2}
 \end{aligned}$$

we calculate

$$v_- = (2 V_D)^{1/2} \approx 2 \times 10^6 \text{ m/s}$$

$$v_+ = \left(\frac{2kT_N}{m_+} \right)^{1/2} \approx 4 \times 10^3 \text{ m/s}$$

$$D_{-t} = \frac{\langle v_-^2 \rangle}{v_c \left(1 + \frac{\omega_{ce}}{v_c} \right)^2} \approx 8 \text{ m}^2/\text{s}$$

$$D_{+t} = \frac{\langle v_+^2 \rangle}{v_c \left(1 + \frac{\omega_{bc}}{v_c} \right)^2} \approx 1.6 \text{ m}^2/\text{s}$$

$$P_+ = m_+ v_+ = 6.8 \times 10^{-24}$$

$$P_- = m_- v_- = 1.8 \times 10^{-24}$$

Let

$$B = b^2 \frac{[P_+ D_{+t} + P_- D_{-t}]}{[P_+ + P_-]} \approx 7.2 \times 10^4$$

$$A = \frac{1}{L} \frac{[P_+ v_+ + P_- v_-]}{[P_+ + P_-]} = 4.2 \times 10^6$$

$$\lambda = B + A \approx 4.3 \times 10^6$$

$$I = 2e(64) \int n_0 dv \lambda = 10^{-7} \lambda = .43a$$

$$\frac{n_0 kT .75 \times 10^5}{\lambda} \approx .15 \text{ percent, the percentage of ionization .}$$

III. THEORY OF THE INTERACTION

A. PHYSICAL EXPLANATION

A plasma can support many different types of waves. These are usually described in two ways: (1) whether the electrons or the ions or both provide the particle reaction that comprises the wave, (2) the type of electric or magnetic field that can be associated with the wave. We are concerned with the electrostatic waves, which have their electric fields parallel to the direction of propagation, and the electromagnetic waves with their electric fields perpendicular to the direction of propagation. Both are also high-frequency waves; i. e., the electrons oscillate back and forth in a background of stationary positive ions.

The amplification mechanism is explained by following an electrostatic wave as it propagates through the plasma. The wave travels at phase velocity v_0 with a finite amplitude; therefore, the wave trough can trap those electrons whose streaming velocities are in a range $v_0 + \Delta < v < v_0 - \Delta$. Once trapped, the electrons move with the wave trough at velocity v_0 . Now consider the electron distribution function f_i at velocities $v_0 \pm \Delta$. Let $\delta = f_i(v_0 + \Delta) - f_i(v_0 - \Delta)$. If $\delta \neq 0$, there is a net transfer of energy between the wave and the particles, since the total energy of the system is conserved. For small signals, the net energy transferred is given by

$$\Delta E = m_i f_i(v_0) v_0^2 \Delta \left. \frac{\partial f(v)}{\partial v} \right|_{v = v_0}$$

Therefore, if the slope of $f_1(v)$ is positive at v_0 , the transfer of energy is to the wave, and the trough grows in amplitude, traps more particles, etc. until some nonlinearity levels off the growth. Typically, this could be due to particle overtaking; i. e., the r-f electron velocity becomes greater than the d-c electron velocity. If the slope is negative at v_0 , the energy is transferred to the particles, and the wave amplitude decays until it reaches the noise level associated with the system. This is a form of Landau damping.

In microwave terms, the plasma is analogous to a sequence of uncoupled cavities, all resonant at the same frequency. When a beam is passed through these cavities, any beam disturbance that has a Fourier frequency component near the resonant frequency of the cavity will excite an oscillation in the cavity, which will simultaneously modulate the beam. In a multicavity klystron for example, the first cavity modulates the velocities of the beam electrons with an external microwave signal. The beam then travels through a drift space where the electrons become density modulated. When the beam arrives at the second cavity, it excites an oscillation that simultaneously remodulates the beam. Each subsequent cavity save the last one impresses a stronger modulation on the beam, thus converting an increasing amount of the kinetic energy of the beam to r-f energy. In the beam-plasma amplifier, the cavities are distributed rather than discrete; therefore the signal gain is exponential as in a traveling-wave tube. Unlike the usual TWT interaction structure, however, the plasma does not necessarily support a propagating wave by itself.

These are two points to be made in interpreting the complex propagation constant. First, we can expect gain only when the phase velocity of the waves is less than that of the d-c velocity. Second, we are primarily interested in the forward-wave interaction; i. e., the velocity of energy transport is in the same direction as the phase velocity of the wave. The backward-wave interaction is also present for certain frequencies, but for high-frequency amplifiers, the forward-wave interaction has greater bandwidth and stability. The gain characteristics (Figures 5-7, 9-13) usually show both forward and backward waves, especially for $1 < a < (1+d_1^2)^{\frac{1}{2}}$; therefore, v_E must pass through zero. As a result we get a zero in the actual gain at the boundary between these two types of waves. We shall set $v_E = v_g$, although this is not strictly valid in a region where the propagation constant is complex and varies rapidly.¹⁷

These explanations are most applicable and easiest to use for the ideal case of infinite, homogeneous beam-plasma cross sections. They do not include the effects of finite geometry, magnetic field, inhomogeneous cross sections, collisions, and nonzero temperature. These effects, which are present in a real plasma, are treated in the following section.

B. MATHEMATICAL DESCRIPTION

1. General Equations

We use three sets of equations to describe the interaction. The first set describes the wave phenomena as postulated by Maxwell:

$$\nabla \times \underline{E} = -\mu_0 d_t \underline{H} \quad , \quad (3.1)$$

$$\nabla \times \underline{H} = \epsilon_0 d_t \underline{E} + \underline{J} \quad , \quad (3.2)$$

$$\nabla \cdot \epsilon_0 \underline{E} = \rho \quad , \quad (3.3)$$

$$\nabla \cdot \mu_0 \underline{H} = 0 \quad . \quad (3.4)$$

The second set, postulated by Boltzmann, describes the properties of the media (see Appendix A):

$$d_t f_i + (\underline{v}_i \cdot \underline{D}) f_i + \frac{q_i}{m_i} [(\underline{E} + \underline{v}_i \times \underline{B}) \cdot \nabla \underline{v}_i] f_i = 0 \quad . \quad (3.5)$$

The subscript i refers to the group of particles of type i .

The third set of equations couples the two previous ones:

$$\underline{J} = \sum_i q_i \int \underline{v}_i f_i dv_i \quad , \quad (3.6)$$

$$\rho = \sum_i q_i \int f_i dv_i \quad . \quad (3.7)$$

These equations will be solved subject to the following boundary conditions. The boundary is a perfectly conducting cylinder, infinite in length, and solutions for the axial electric field must be square integrable over any unit cross-sectional area. This means that

$$E_\theta = E_z = 0 \quad \text{at } r = r_0$$

$$E_z \in L^2$$

We are interested in finding the steady-state axially symmetric modes. These modes have a nonzero axial electric field at the center of the cylinder, thus ensuring a strong interaction between the beam and the plasma. Therefore, we look for solutions that have a space-co-ordinate dependence of the form $R(r) \exp j(\omega t - \beta z)$. This simplifies the following partial derivatives to

$$d_t = j\omega \quad d_z = -j\beta \quad d_\theta = 0$$

The media equations introduce the nonlinear term,

$$\left[(\underline{v}_i \times \underline{B}) \cdot \nabla_{\underline{v}_i} \right] f_i$$

Though the solution with nonlinearity included is a problem of great interest, we consider the linearized equations to keep the mathematics simple. To linearize the equations, we expand all the variables, except time, in the following manner:

$$A(\underline{x}, v, t) = A_0(\underline{x}_0, v_0) + \lambda A(\underline{x}_0, v_0, t) \quad (3.8)$$

where λ is an indication of the order of nonlinearity. For the linearized solutions we require that

$$|\lambda A_1| \ll |A_0| \quad (3.9)$$

Put Equation (3.8) into the three sets of equations, then collect terms by their power in λ . By making λ arbitrarily small, we can justify setting each coefficient of λ^i equal to zero, thereby getting a zero-order and a first-order set of equations, which are

$$\nabla \times \underline{E}_0 = 0 \quad (3.10)$$

$$\nabla \times \underline{H}_0 = \underline{J}_0 \quad (3.11)$$

$$\nabla \cdot \epsilon_0 \underline{E}_0 = \rho_0 \quad (3.12)$$

$$\nabla \cdot \mu_0 \underline{H}_0 = 0 \quad (3.13)$$

$$(\underline{v}_{oi} \cdot \nabla) f_{oi} + \frac{q_i}{m_i} \left[(\underline{E}_0 + \underline{v}_{oi} \times \underline{B}_0) \cdot \nabla_{\underline{v}_{oi}} \right] f_{oi} = 0 \quad (3.14)$$

$$\underline{J}_0 = \sum_i q_i \int \underline{v}_{oi} f_{oi} d\underline{v}_{oi} \quad (3.15)$$

$$\rho_0 = \sum_i q_i \int f_{oi} d\underline{v}_{oi} \quad (3.16)$$

$$\nabla \times \underline{E}_1 = -\mu_0 d_+ \underline{H}_1 \quad (3.17)$$

$$\nabla \times \underline{H}_1 = \epsilon_0 d_+ \underline{E}_1 + \underline{J}_1 \quad (3.18)$$

$$\nabla \cdot \epsilon_0 \underline{E}_1 = \rho_1 \quad (3.19)$$

$$\nabla \cdot \mu_0 \underline{H}_1 = 0 \quad (3.20)$$

$$d_+ f_{1i} + (\underline{v}_{oi} \cdot \nabla) f_{1i} + (\underline{v}_{1i} \cdot \nabla) f_{oi} + \frac{q_i}{m_i} \left[(\underline{E}_0 + \underline{v}_{oi} \times \underline{B}_0) \cdot \nabla_{\underline{v}_{oi}} \right] f_{1i} \\ + \frac{q_i}{m_i} \left[(\underline{E}_1 + \underline{v}_{1i} \times \underline{B}_0) + \underline{v}_{oi} \times \underline{B}_1 \right] \cdot \nabla_{\underline{v}_{oi}} f_{oi} = 0 \quad (3.21)$$

$$\underline{J}_1 = \sum_i \int (\underline{v}_{1i} f_{oi} + \underline{v}_{oi} f_{1i}) d\underline{v}_{oi} + \int \underline{v}_{oi} f_{oi} d\underline{v}_{1i} \quad (3.22)$$

$$f_1 = \sum_i \left[\int f_{1i} dv_{0i} + \int f_{0i} dv_{1i} \right] \quad (3.23)$$

Equations (3.10) through (3.16) form a nonlinear time-independent set. Equations (3.17) through (3.23) form a linear time-dependent set. Assume that $\underline{E}_0 \approx 0$. This is a reasonable assumption as long as the charged particle density $\rho_0 \approx 0$. (This requires that $\rho_0 > 10^{17} \text{ m}^{-3}$). Assume that we have solved the time-independent set of equations. We usually chose the zero-order distribution functions to be Maxwellian. This is reasonable because the electron-beam duty cycle, i.e., ratio of on to off time, is very low, and Boltzmann's H theorem states that the equilibrium distribution function is Maxwellian. To solve the time-dependent set, we express f_{1i} in terms of the variables, E_1 , H_1 , v_1 , and then evaluate either \underline{J}_1 or ρ_1 by performing the appropriate integrals over velocity space. We put these results either into the wave equation or into Poisson's equation and solve for the self-consistent (nontrivial) fields. This gives us a differential equation whose solutions are eigenfunctions, from which we get the dependence of the field on the spatial co-ordinates. We also get the longitudinal propagation constant β as a function of frequency.

2 Effects of Geometry and Magnetic Field

We take f_{0i} to be a normalized shifted Maxwellian distribution in the zero-order longitudinal velocity v_{1i} . This gives

$$f_{0i}(v_1) = \pi^{-1/2} v_{T_i}^{-1/2} e^{-\frac{(v_1 - v_{0i})^2}{v_{T_i}^2}} \quad (3.24)$$

However, we will anticipate the results of Section 3b which follows, that a nonzero plasma temperature does not strongly affect the gain characteristic when the geometry is finite, and consider the case where v_{T_i} approaches zero; then f_{oi} becomes the Dirac delta function defined by

$$1 = \int_{-\infty}^{\infty} f_{oi}(v_i) dv_i \quad (3.25)$$

This is easily seen by making the change of variables,

$$U = \frac{v_i - v_{oi}}{v_{T_i}} \quad (3.26)$$

and taking the integral of the limit. Since f_{oi} is defined by an integral over velocity space, we must use the velocity moments of the Boltzmann equation instead of the equation itself to describe the beam-plasma media. Following the derivation given by Spitzer,¹⁸ we get the following equations:

$$d_+ \underline{v}_{1i} + (\underline{v}_{oi} \cdot \nabla) \underline{v}_{1i} + (\underline{v}_{1i} \cdot \nabla) \underline{v}_{oi} = F_i \quad (3.27)$$

$$F_i = N_i \left[\underline{E}_1 + \underline{v}_{1i} \times \underline{B}_0 + \underline{v}_{oi} \times \underline{B}_1 \right] \quad (3.28)$$

$$d_+ N_{1i} + \nabla \cdot (N_{oi} \underline{v}_{1i} + N_{1i} \underline{v}_{oi}) = 0 \quad (3.29)$$

$$\underline{J}_1 = \sum_i (N_{oi} q_i \underline{v}_{1i} + N_{1i} q_i \underline{v}_{oi}) \quad (3.30)$$

$$\rho_1 = \sum_i q_i N_{1i} \quad (3.31)$$

Equations (3.27) - (3.31), the wave equations, and the boundary conditions give enough information to solve both for the propagation constant as a function of frequency, and also for the r-f fields. In the general case, however, this involves solution of two coupled, linear, fourth-order differential equations. There are two types of approximations that reduce the order of the differential equation from four to two. The mode decoupling approximation is used when the waves of interest would propagate in the absence of the beam-plasma media. These waves form two orthogonal sets in an empty wave guide, and the approximation is that these sets are still orthogonal when the wave guide is not empty. To use this approximation, set

$$E_{\theta} = H_r = H_z \equiv 0 \quad , \quad (3.32)$$

or

$$E_z = E_r = H_{\theta} \equiv 0 \quad . \quad (3.33)$$

The quasi-static approximation is used when the waves of interest are dependent on the presence of a beam plasma. The approximation states that the r-f magnetic field is small compared to that usually associated with an electromagnetic wave and, therefore, the r-f electric field is nearly irrotational. We can, therefore, set the curl of \underline{E}_1 equal to zero and solve for the scalar potential ϕ instead of using a vector as a variable. To use this approximation, set

$$\nabla \times \underline{E}_1 \equiv 0 \quad , \quad (3.34)$$

$$\underline{E}_1 = -\nabla\phi \quad , \quad (3.35)$$

and evaluate \underline{H}_1 from Equation (3.18). This is called the quasi-static approximation, because its validity depends on the phase velocity of the wave being much less than the speed of light. The approximation is also not valid at frequencies for which any of the modes, e.g., the beam cyclotron modes, have a resonance resulting from the cyclotron motion of the electrons.

When this approximation is used, the wave equation for the homogeneous case (see Appendix B) is

$$D \frac{d}{dr} \phi + \frac{D}{r} \phi + A \phi = 0 \quad , \quad (3.36)$$

$$D = \left\{ 1 - \frac{1}{a^2 - d_1^2} - \frac{d_2^2}{a^2 \left[\left(1 - \frac{\beta}{\beta_e} \right)^2 - \frac{d_1^2}{a^2} \right]} \right\} \quad , \quad (3.37)$$

$$A = -\beta^2 \left[1 - \frac{1}{a^2} - \frac{d_2^2}{a^2 \left(1 - \frac{\beta}{\beta_e} \right)^2} \right] \quad , \quad (3.38)$$

where

$$a = \frac{\omega}{\omega_{pp}} \quad d_1 = \frac{\omega_{ce}}{\omega_{pp}} \quad d_2 = \frac{\omega_{pb}}{\omega_{pp}} \quad .$$

Equation (3.36) is a form of Bessel's equation and its solution is given by

$$\phi = \sum \phi_i J_0(b_{oi}r) \quad , \quad (3.39)$$

$$J_0(b_{oi}r_0) = 0 \quad , \quad (3.40)$$

$$\frac{-\beta^2}{\beta_{eo}^2} \left\{ 1 - \frac{1}{a^2} - \frac{d_2^2}{a^2 [1 - \beta/\beta_e]^2} \right\} = \frac{b_{oi}^2}{\beta_{eo}^2} \quad (3.41)$$

$$\left\{ 1 - \frac{1}{a^2 - d_1^2} - \frac{d_2^2}{a^2 \left[\left(1 - \frac{\beta}{\beta_e}\right)^2 - \frac{d_1^2}{a^2} \right]} \right\}$$

Equation (3.41) is a dispersion relation, whose solution gives

$$\beta = \beta(a, d_1, d_2, d_3)$$

where $d_3 = 2.4 v_o / r_o \omega_{pp}$. Figure 4 plots β/β_{eo} versus a for a set of parameters (d_1, d_2, d_3) that correspond to expected experimental values. Let us consider the case for r_o approaching infinity; then b_{oi} approaches zero and Equation (3.41) reduces to the following relations:

$$-\beta^2 = 0 \quad (3.42)$$

$$\left[1 - \frac{1}{a^2} - \frac{d_2^2}{a^2 (1 - \beta/\beta_e)^2} \right] = 0 \quad (3.43)$$

$$\left\{ 1 - \frac{1}{a^2 - d_1^2} - \frac{d_2^2}{a^2 \left[\left(1 - \frac{\beta}{\beta_e}\right)^2 - \frac{d_1^2}{a^2} \right]} \right\} = \infty \quad (3.44)$$

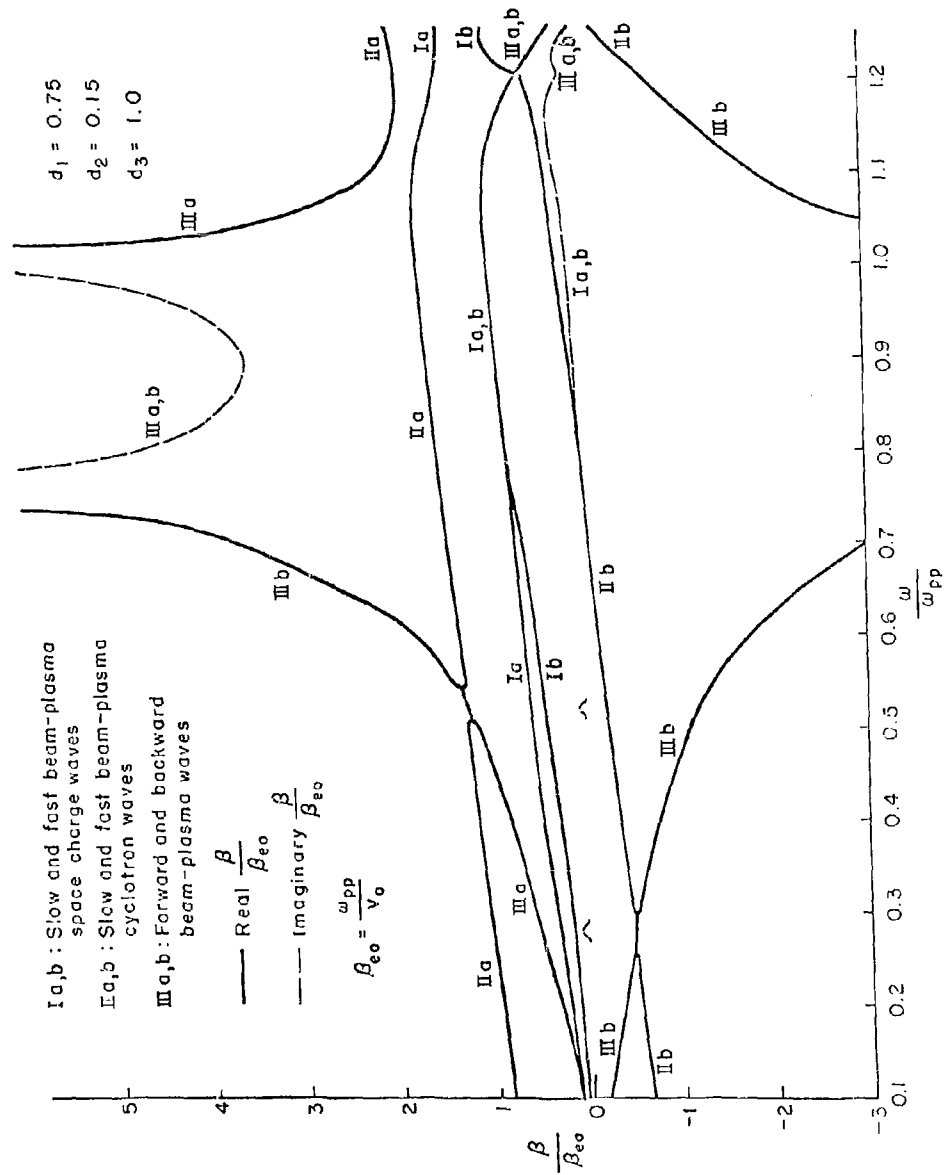


FIGURE 4. Dispersion Diagram for a Homogeneous Beam-Plasma Media.

Equation (3.42) voids the quasi-static approximation; the correct equation is

$$-\beta^2 = \frac{\omega^2}{C^2} \left[1 - \frac{1}{a^2} - \frac{d_2^2}{a^2} \right], \quad (3.45)$$

and the solutions represent electromagnetic waves that propagate in free space. Equation (3.43) gives the space-charge modes,

$$\beta = \beta_e \left[1 \pm \frac{d_2}{a} \left(\frac{1}{a^2 - 1} \right)^{1/2} \right]$$

Equation (3.44) gives the cyclotron modes,

$$\beta = \beta_e \left[1 \pm \frac{d_1}{a} \right] \quad a \neq d_1$$

The space charge and cyclotron modes are beam modes that are modified by the presence of the plasma. By the physical arguments given earlier, we know that the amplifying wave must have a phase velocity approximately that of the beam, i.e., $\beta \approx \beta_e$ for amplification. This suggests the following change of variable often used in microwave tube analysis,

$$\beta = \beta_e \left[1 + \frac{d_2}{a} R \right], \quad (3.46)$$

where R is called the plasma-frequency reduction factor, and "plasma" refers to the beam electrons. In our case, R is usually complex, so that the analogy does not strictly apply; nevertheless, we will call R the beam-plasma reduction factor. Gain is proportional to the

imaginary part of R , whenever the gain is possible. Rewriting the dispersion relation in terms of R gives

$$\frac{d_3^2}{a^2} = \frac{\left(1 + R \frac{d_2}{a}\right)^2 \left(1 - \frac{1}{a^2} - \frac{1}{R^2}\right)}{\left(1 - \frac{1}{a^2 - d_1^2} - \frac{1}{R^2 - \frac{d_1^2}{d_2^2}}\right)} \quad (3.47)$$

For r_0 finite, the singularity at the plasma frequency in the space-charge mode is removed. Indeed for the choice of parameters shown in Figure 4, neither the real nor imaginary parts of R are large at a equal to one. Physically we can think of this as a coupling of a growing space-charge mode to a plasma wave that is being attenuated, with the degree of coupling dependent on the influence of the cylinder walls. Figures 5, 6, and 7 show the effects of gain versus frequency varying d_1 , d_2 , and d_3 respectively. Whenever the gain is particularly high, it is very apt to be limited by other effects, e. g., inhomogeneities, collisions, nonzero temperature. Figure 4 is the dispersion diagram of the modes given by Equations (3.16), (3.17), and (3.18). As expected, the mode coupling through induced wall currents has removed the singularity in the space-charge mode of the beam plasma near the plasma frequency. Figure 4 could have been obtained qualitatively using coupled mode theory.^{19, 20} The interaction of the slow cyclotron mode with the forward mode leads to forward-wave gain, and the interaction of the fast cyclotron mode with the backward mode leads to backward-wave

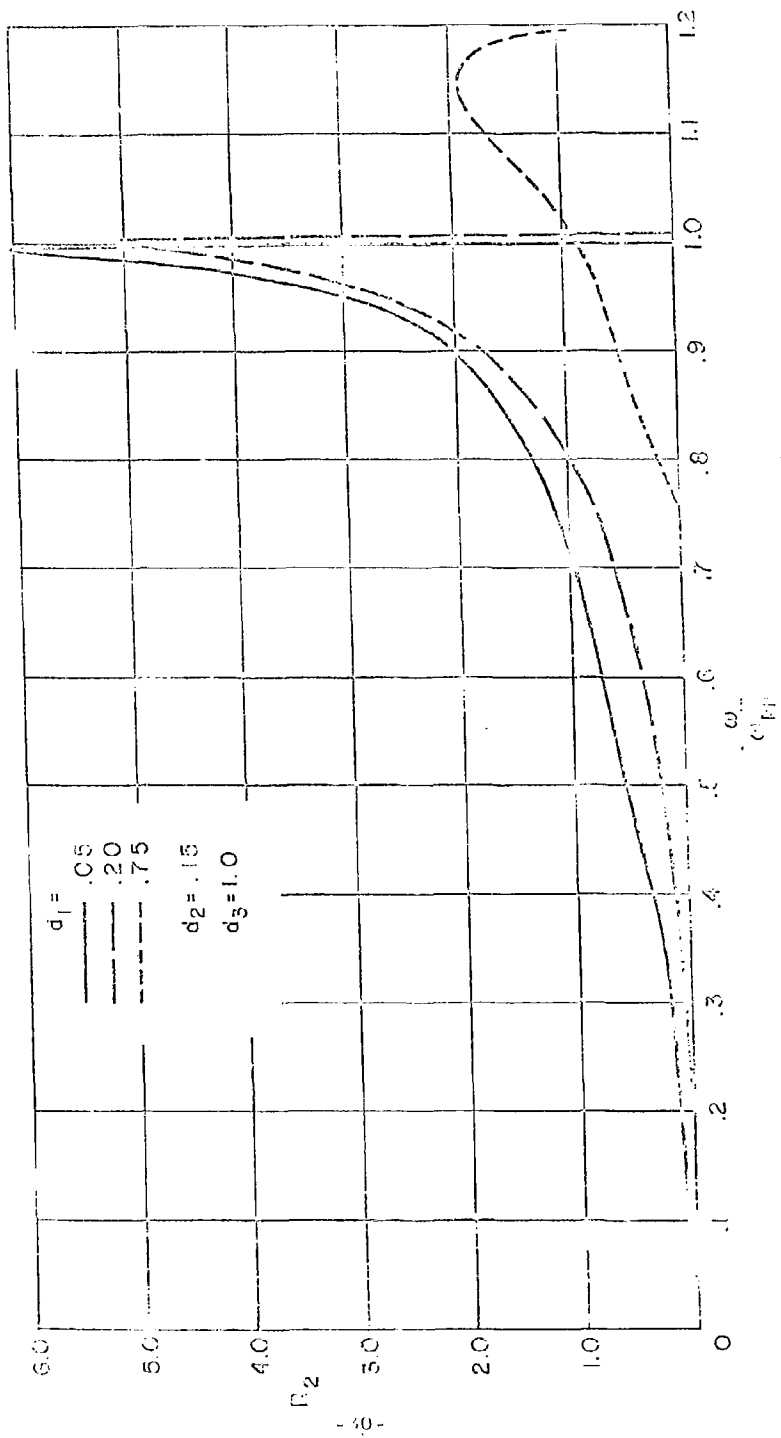


Fig. 10. Gain Dependence on M_2 for Field (Power Gain) $\approx 8.6 \frac{pb}{V_0} R_2$ (db cm).

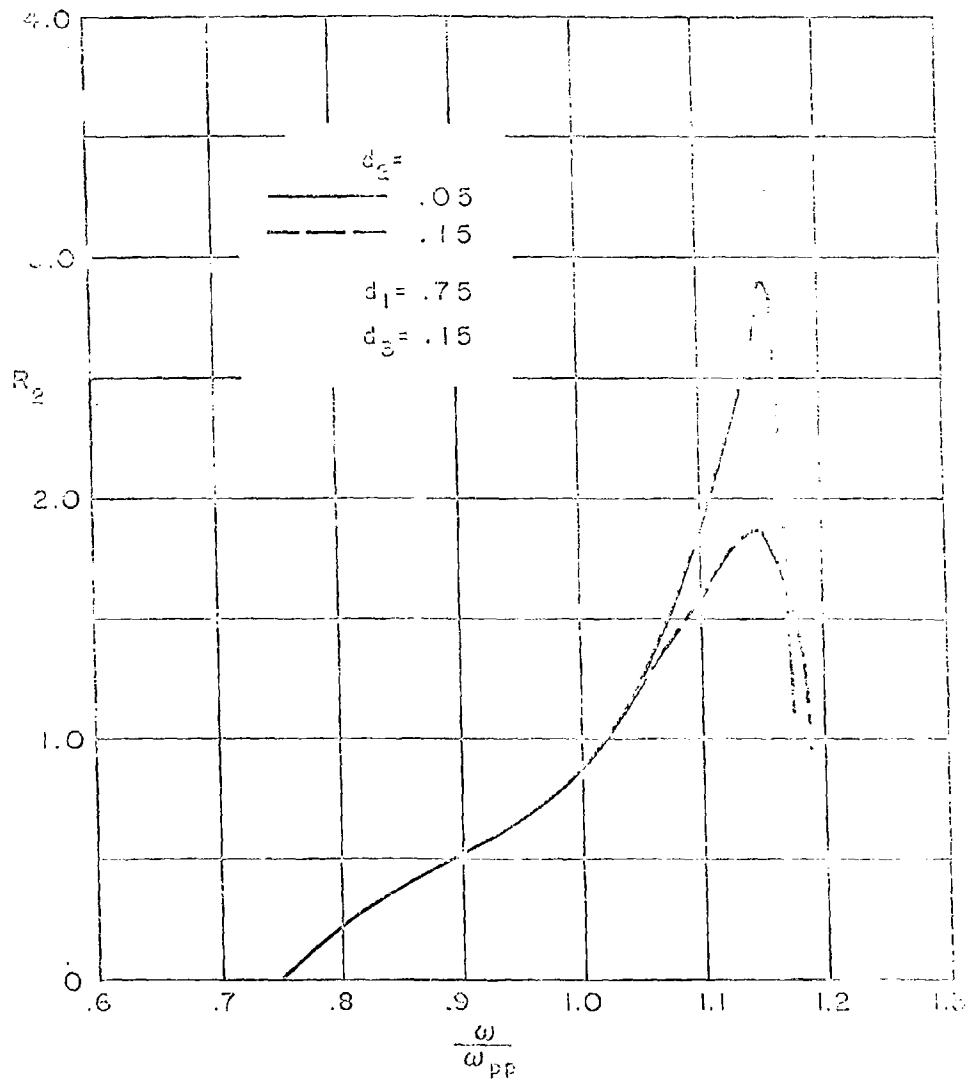


FIGURE 6. Gain Dependence on Beam Density.

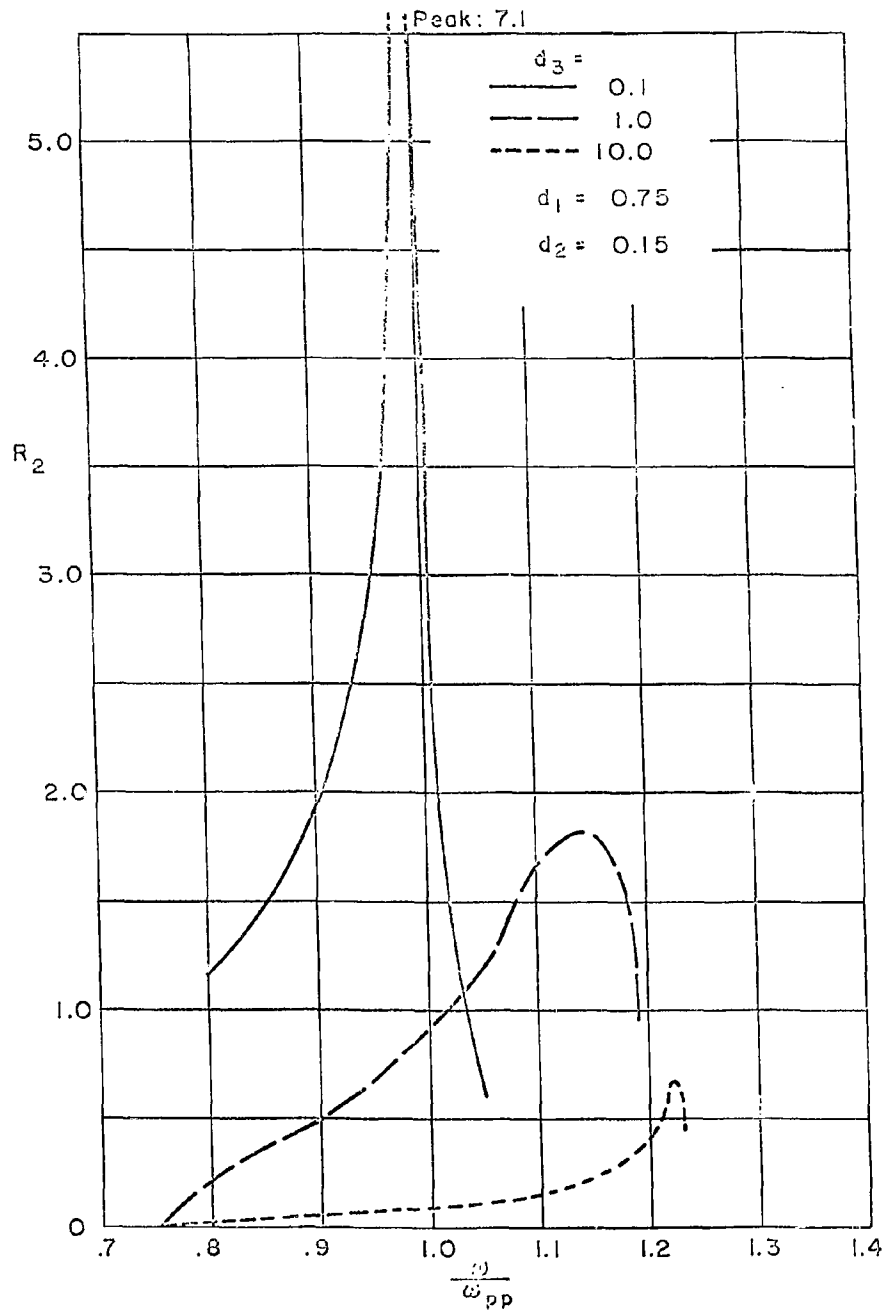


FIGURE 7. Gain Dependence on d_3

gain. Note that by having the inequality $1 \gtrsim d_2 > d_1$, the two forward-wave regions can be combined to get a broad amplification bandwidth. Maintaining this inequality at high frequencies, however, would be impractical, so this case is not discussed further.

3. Effects of Beam-Plasma Inhomogeneity

Using the same restrictions as in the homogeneous case, gives differential equation (see Appendix B):

$$D d_{rr} \phi + \frac{(E+D)}{r} d_r \phi + A \phi = 0 \quad , \quad (3.48)$$

$$A = -\frac{d_3^2}{a^2} \left(1 + R \frac{d_2}{a}\right)^2 \left(1 - \frac{\hat{N}_{o1}}{a^2} - \frac{\hat{N}_{o2}}{R^2}\right) \quad , \quad (3.49)$$

$$D = \begin{pmatrix} 1 - \frac{\hat{N}_{o1}}{a^2 - d_1^2} & -\frac{\hat{N}_{ov}}{R^2 - \frac{d_1^2}{d_2^2}} \end{pmatrix} \quad , \quad (3.50)$$

$$E = r \begin{pmatrix} \frac{d_r \hat{N}_{o1}}{a^2 - d_1^2} & + \frac{d_r \hat{N}_{o2}}{R^2 - \frac{d_1^2}{d_2^2}} \end{pmatrix} \quad . \quad (3.51)$$

The density variations were chosen to be of the form,

$$A_i e^{-\left(a_i r \frac{r}{r_0}\right)^{q_i}}$$

The constants a_i determine the cut-off points for the variation while the constants q_i determine the sharpness of the cutoffs. This gives great flexibility in choosing density cross sections, as illustrated in Figure 3. Examples of cross-sections used are shown in Figure 8.

The coefficients for Equation (3.9) become

$$A = -\frac{d_3^2}{a^2} \left[1 + R \frac{d_2}{a} \right]^2 \left[1 - \frac{e^{-(a_1 r_0 v)^{q_1}}}{a^2} - \frac{e^{-(a_2 r_0 v)^{q_2}}}{R^2} \right], \quad (3.52)$$

$$D = \left[1 - \frac{e^{-(a_1 r_0 v)^{q_1}}}{a^2 - d_1^2} - \frac{e^{-(a_2 r_0 v)^{q_2}}}{R^2 - \frac{d_1^2}{d_2^2}} \right], \quad (3.53)$$

$$E = -\frac{q_1 (a_1 r_0 v)^{q_1} e^{-(a_1 r_0 v)^{q_1}}}{a^2 - d_1^2} - \frac{q_2 (a_2 r_0 v)^{q_2} e^{-(a_2 r_0 v)^{q_2}}}{R^2 - \frac{d_1^2}{d_2^2}}. \quad (3.54)$$

A second-order, ordinary, linear differential equation with nonconstant complex coefficients that are also rational functions of the eigenvalue R , is difficult to solve explicitly by analytic techniques. It can be handled by a series of straightforward, though long, numerical computations. A computer program for solving this equation is given in Appendix C. The program couples a procedure for numerical integration to a search procedure for R . There was a question of validity when $D(r) = 0$ was in the range of integration. However, by expanding the coefficients in a

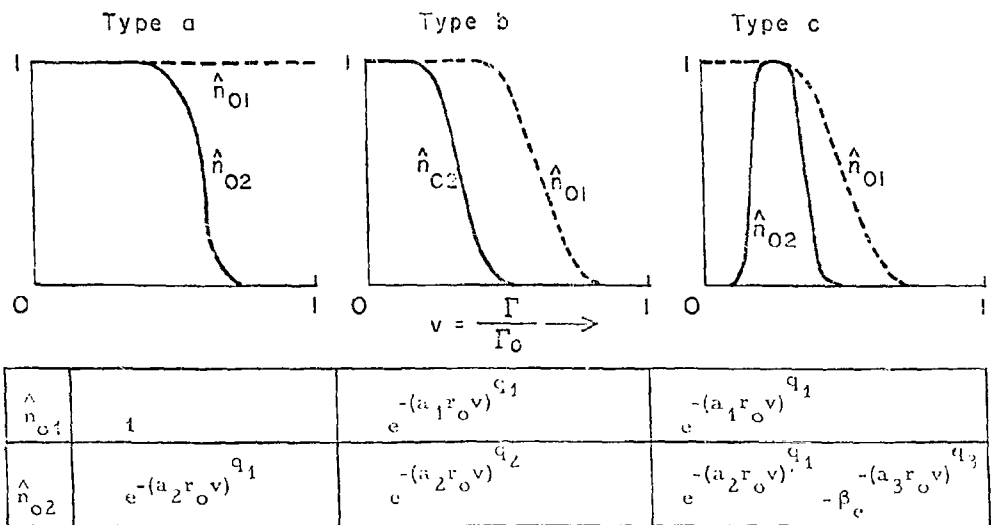


FIGURE 8. Inhomogeneous Beam-Plasma Cross Sections.

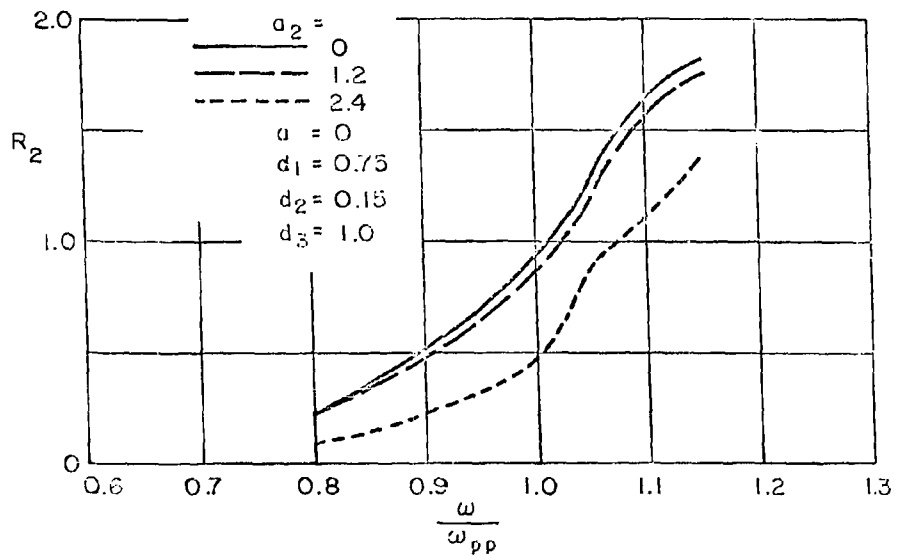


FIGURE 9. Gain Dependence on Beam Width.
(See Type a of Figure 8.)

power series about such a point, we obtain a good solution.²¹ Indeed, increasing the fineness of the integration at these points gave finite, though discontinuous, values for ϕ and $d_x\phi$. Figures 9, 10, and 11 show the gain characteristics for the cross sections of Figure 8.

In Figures 10 and 11 the gain curves for the cross section with the smallest diameter show several peaks,²² because of lowered coupling between the beam and plasma modes. Consider the analogy of a lumped circuit of several cavities synchronously tuned and strongly coupled to each other by a linear mechanism. When sufficiently over-coupled, the circuit-frequency characteristic shows just one broad peak. As the coupling decreases, the peak becomes narrower and higher and then becomes two broad peaks. These also become narrower and higher until they also divide into two peaks, etc. The results of the repeated division is shown in Figure 10, where the beam-plasma coupling, through induced surface current on the metal wall (or plasma sheath), is reduced as the diameter of beam and plasma is reduced.

4. Effects of Collisions and Nonzero Plasma Temperature

a. Collisions

We can include the effects of elastic collisions between ions and plasma electrons by adding an additional term $v_c \frac{v}{|v|}$, to F_i in Equation (3.28). We have neglected the effects of all other collisions. Since we can justify neglecting these collisions only by taking the percentage ionization, the particle velocity distribution functions, pressure, etc.

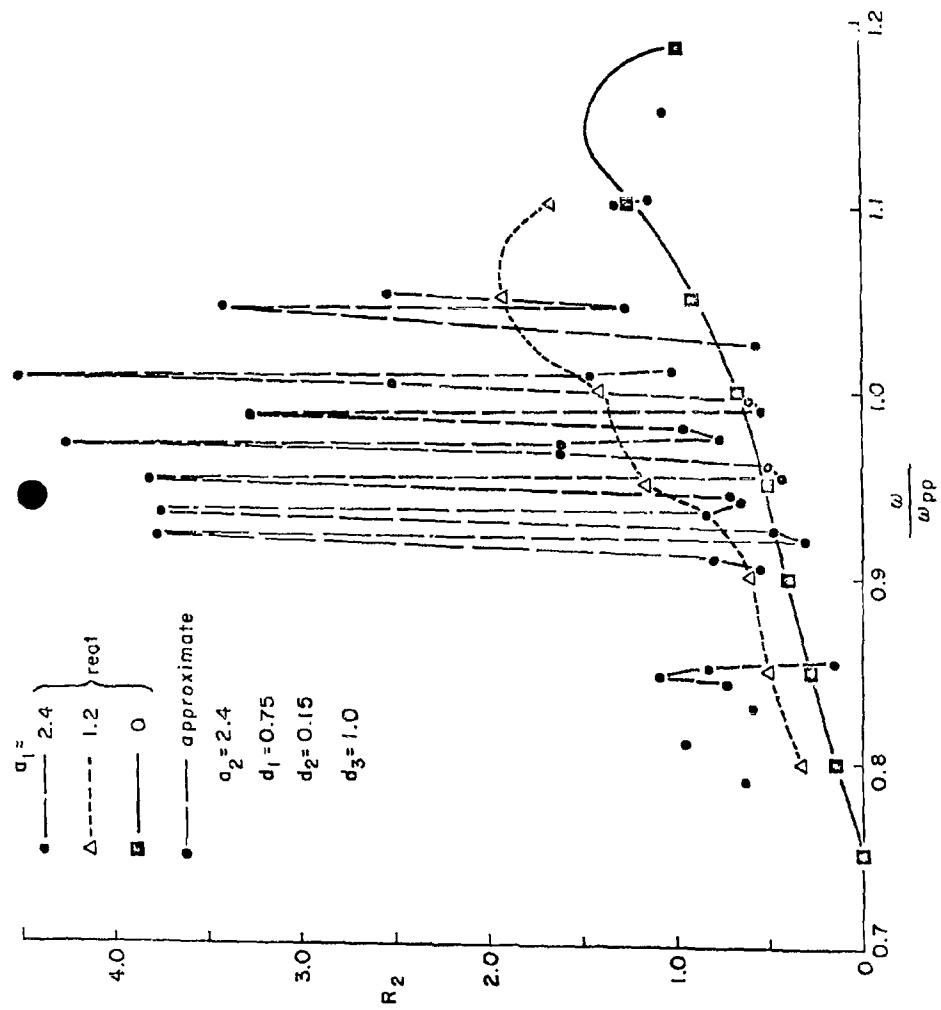


FIGURE 10. Gain Dependence on Plasma Width.
 (See Type b of Figure 8.)

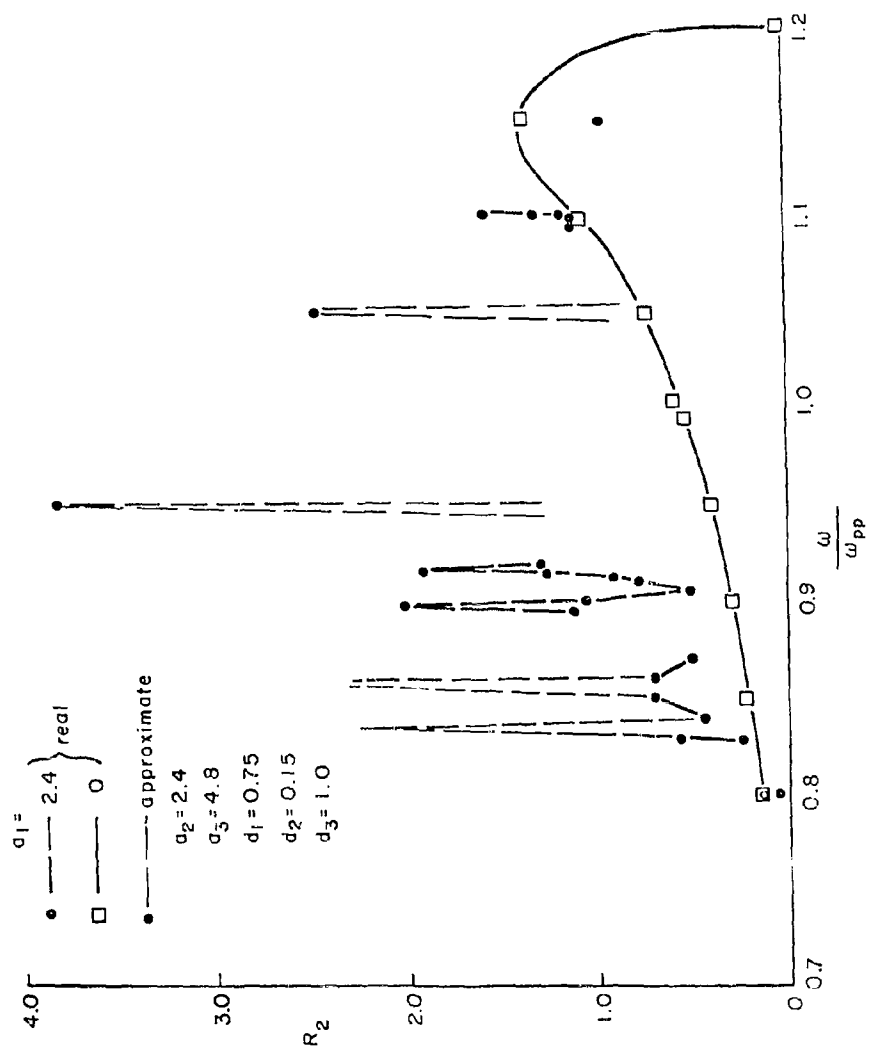


FIGURE 11. Gain Dependence for a Hollow Beam. (See Type c of Figure 8.)

into account, the following analysis is accurate only to an order of magnitude. The solution for the space-charge mode in the infinite case is

$$\frac{\beta}{\beta_e} = a \left\{ 1 + d_2 \frac{1}{\left[a^2 - \frac{1}{\left(i - j \frac{d_4}{a} \right)} \right]} \right\}, \quad (3.55)$$

where

$$d_4 = \frac{\nu_c}{\omega_{pp}}$$

This removes the singularity at the plasma frequency, and if there were no other broadening processes available, e. g., finite geometry, inhomogeneities, plasma temperature, it would give the gain as a function of frequency. Figure 12 plots the gain characteristic for different values of d_4 . In the plasma experiment, we expect a value for d_4 of less than 10^{-3} .

b. Plasma Temperature

Here we work directly with the Boltzmann equation, Equation (3.21), to express f_{1i} in terms of E_i and v_{1i} and then integrate to get ρ , as shown in Appendix D and consider only $v_{Ti} \neq 0$. It is reasonable to consider only the effect of plasma temperature, since the relative velocity spread of the beam is much less than that of the plasma. From Appendix D we get

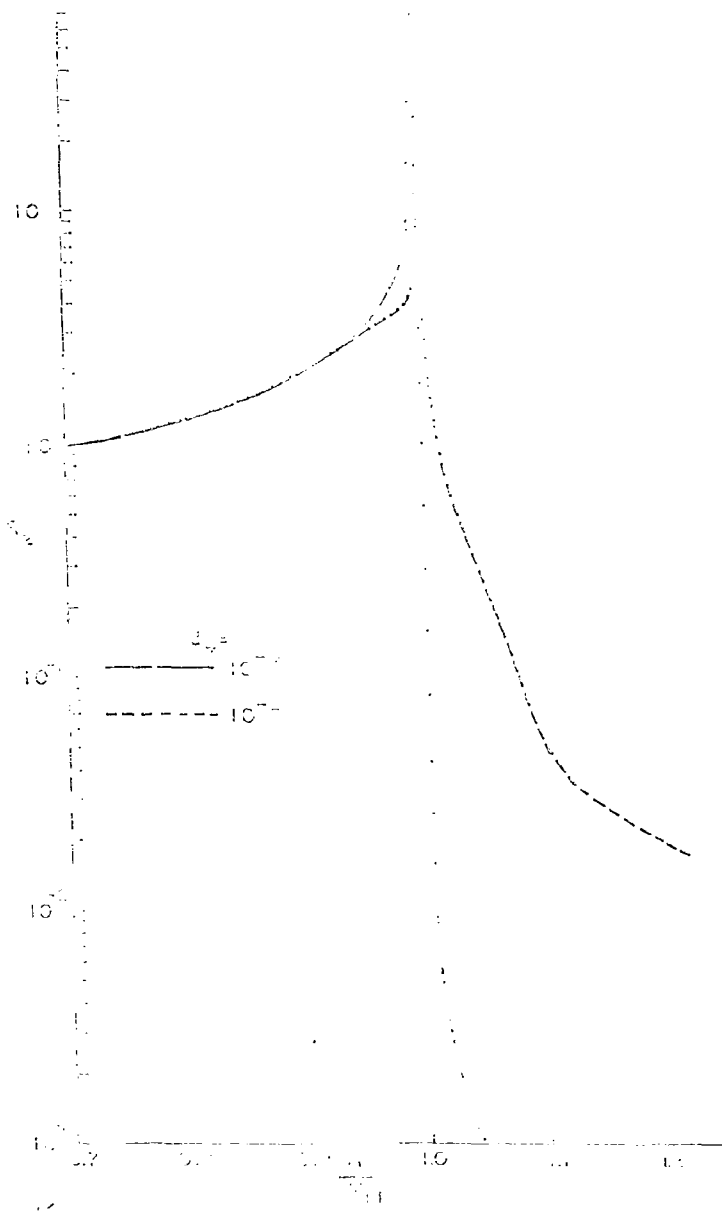


FIGURE 12. Gain Dependence on Plasma Collisions.

$$\hat{N}_{11} = -N \frac{j\beta \delta^2 \left[1 + \frac{3}{2} \delta^2 \frac{1}{\left(1 + \frac{\beta}{\beta_{e1}}\right)^2} \right]}{\omega^2 \left(1 - \frac{\beta}{\beta_{e1}}\right)^2} \quad (3.56)$$

$$\delta = \frac{v_{T1}}{v_{\phi}} \quad (3.57)$$

The approximations are good for all waves that satisfy

$$\delta^2 \ll 1$$

Consider that a stationary plasma β_{e1} is infinite in an infinite geometry.

The dispersion equation is

$$\left\{ 1 - \frac{1}{a^2} \left[1 + \frac{3}{2} \left(\frac{\beta}{\beta_T} \right)^2 \right] - \frac{d_2^2}{a^2 \left(1 - \frac{\beta}{\beta_e} \right)^2} \right\} = 0 \quad (3.58)$$

Figure 13 shows the gain characteristic as a function of γ , where

$$\gamma = \frac{\beta_{e0}^2}{\beta_{T0}^2} = \left(\frac{v_T}{v_D} \right)^2, \quad \beta_{T0} = \frac{\omega_{pp}}{v_T}, \quad v_T = \left(\frac{2kT_e}{m} \right)^{\frac{1}{2}}$$

C. CALCULATION OF POWER GAIN AND PHASE SHIFT

1. Experimental

The equipment needed to measure power gain is shown in Figure 14a. A reading was taken on the calibrated attenuator with the amplifier removed

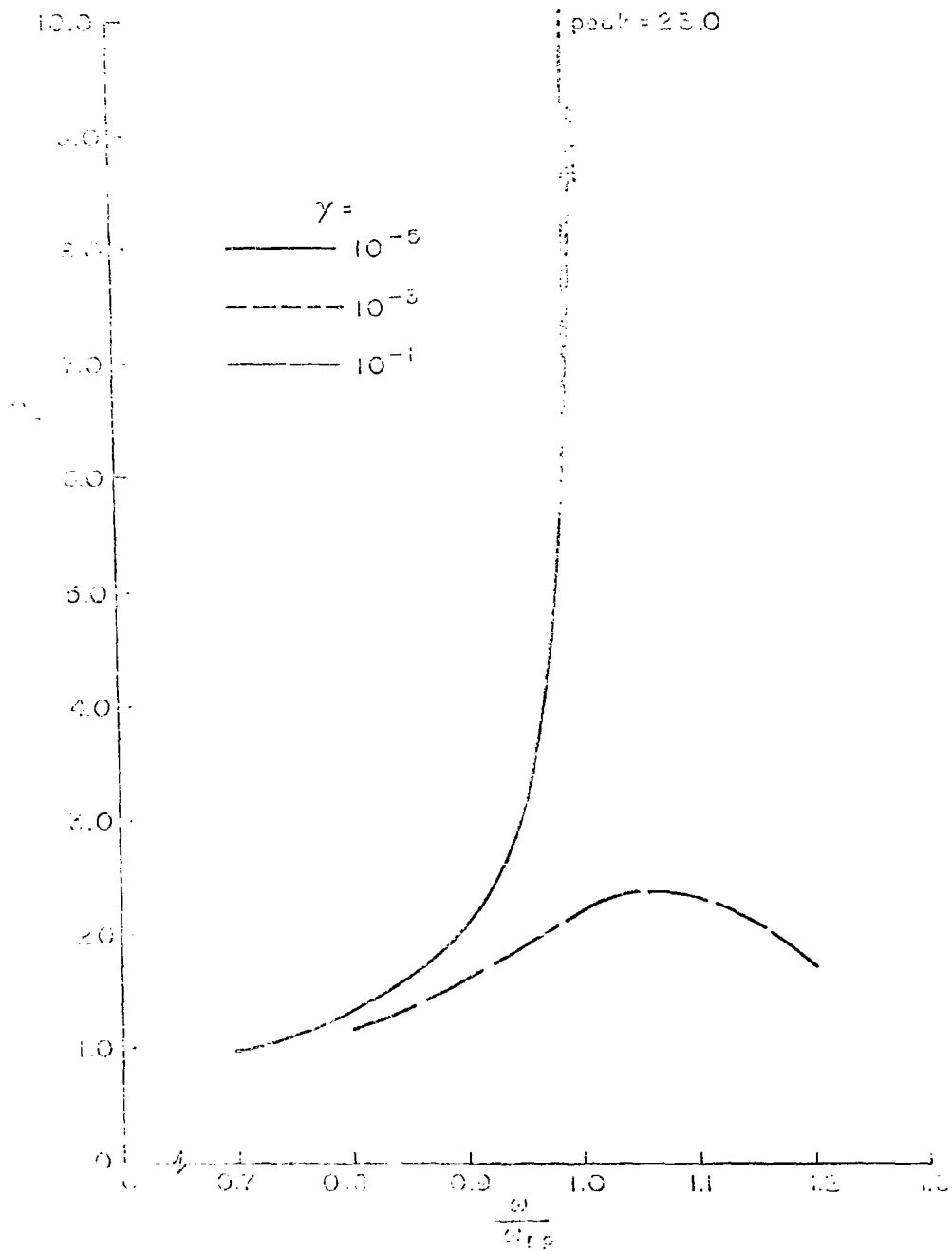


Fig. 10. Variation of n_e with ω/ω_{pe} for different Plasma Temperature.

(dashed line). The amplifier was then placed in the circuit and the attenuator readjusted to get the same reading on the power indicator. The difference in attenuator settings represented the power gain. Of course, corrections resulting from mismatch or amplifier accessories had to be taken into account.

In Figure 14b, equipment was set up to measure amplifier phase shift to within an additive constant of $2k\pi$ radians. A minimum was found on the slotted line with the amplifier out of the circuit (dashed line). With the amplifier in the circuit, a second minimum was found. The amplifier phase shift was equal to twice the VSWR minimum shift.

2. Theoretical

To compare the theoretical and experimental values of power gain, we must know the coupling coefficients for the input and output klystron gaps. The procedure for determining these coefficients is lengthy, and we shall assume that they are known. The total power gain is given by

$$\frac{P_{E2}}{P_{E1}} = \frac{\mu_{11}^2}{\mu_{21}^2} \left[e^{\left(\frac{2\omega pb L \text{Im}(R)}{v_o} \right)} \right] v_E, \quad (3.59)$$

where μ_{11}^2 is the ratio of the power of the lowest-order mode leaving the input cavity to the input power; μ_{21}^2 is the ratio of the power of the lowest-order mode in the output section, to the power output from the amplifier; and $v_E(R)$ is the velocity of energy transport, which we take

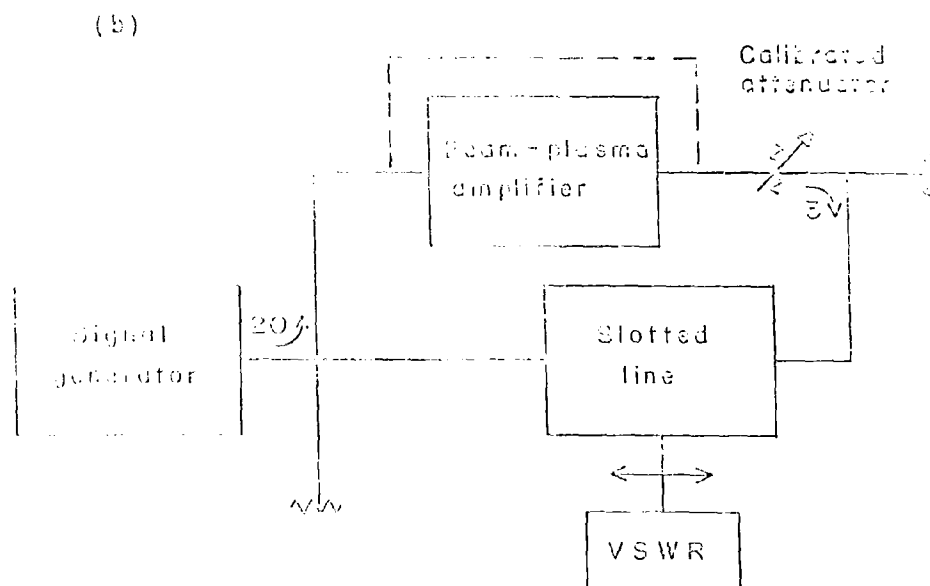
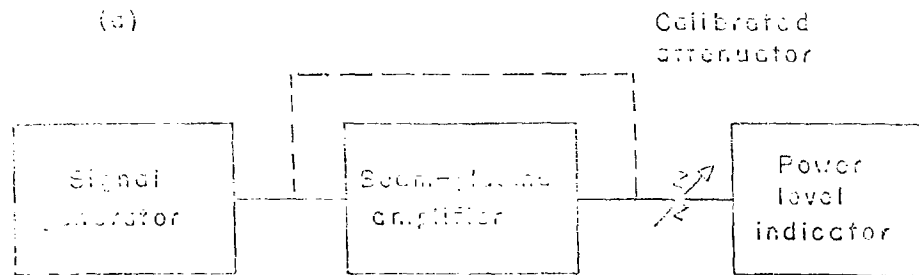


Fig. 2. Measurement (a) of Power Gain and (b) of Phase Shift.

equal to the group velocity of the wave. For the cases discussed in III B,

$$\frac{v_g}{v_o} = \frac{1}{1 + \frac{\partial R}{\partial \alpha}} \quad (3.60)$$

III. CONCLUSIONS

We have found that the effects of finite geometry, inhomogeneous density cross sections, plasma collisions, and plasma temperature all limit the gain and broaden its frequency range. For the experiment now being conducted, we expect the density cross section to be the most important of these factors. For higher-frequency applications, the effects of plasma collisions may dominate the broadening processes since ν_c/ω_{pp} varies as $n^{1/2}$. This is a strong argument for plasma generation using contact ionization, which has a percentage of ionization greater than 50 per cent, for frequencies over 100 Gc/s.

IV. REFERENCES

1. J. R. Pierce, and W. B. Hebenstreit, "A New Type of High-Frequency Amplifier," Bell Sys. Tech. Jour., 28 (1949), p. 33.
2. D. Bohm, and E. P. Gross, "Theory of Plasma Oscillations," Phys. Rev., 75 (1949), pp. 1851, 1864.
3. A. V. Haeff, "The Electron Wave Tube," Proc. I.R.E., Radio Engineers, 37 (1949), p. 4.
4. J. R. Pierce, "Possible Fluctuations in Electron Streams due to Ions," Jour. Ap. Phys., 19 (1948), p. 231.
5. A. W. Trivelpiece, "Slow-Wave Propagation in Plasma Waveguides," Report No. 7, Cal. Inst. Tech. (1958).
6. S. F. Paik, "Coupling of Modes between a Slow Wave Guide and Plasma Helix," Jour. Ap. Phys., 33 (1962), p. 2468.
7. P. Chorney, "Study of the Behavior of Beam Plasma Amplifiers." Final Report, Contract No. NObsr 84206, Microwave Associates (1961).
8. A. Bers, Waves in Anisotropic Plasmas, Part II, Cambridge: M.I.T. (1963).
9. E. A. Jackson, "Drift In Stabilities in a Maxwellian Plasma," Phys. Fluids, 3 (1960), p. 786.
10. J. D. Jackson, "Plasma Oscillations," Plasma Physics, 1 (1960), p. 171.
11. P. J. Kellogg and H. Liemohn, "Instability of Contra-Streaming Plasmas," Phys. Fluids, 3 (1960), p.40.

12. N. R. Rostoker and M. N. Rosenbluth, "Test Particles in a Completely Ionized Plasma," Phys. Fluids, 3 (1960), p. 245.
13. A. Simon, "Diffusion of Arc Plasmas across a Magnetic Field," in Peaceful Uses of Atomic Energy, Vol. 32, United Nations (1958), p. 343.
14. "High-Power Beam-Plasma Amplifier," Report No. 1, Contract No. NObsr 83105, Microwave Associates (March 1963).
15. B. B. Kadomtsev and A. V. Nedospasov, "Instability of the Positive Column in a Magnetic Field," Jour. Nuc. Energy, Part C, 1 (1960), p. 220.
16. L. F. Eastman and L. A. MacKenzie, "Investigation of New Concepts for Microwave Power Generation," Research Report EE 560, Cornell University (April 1963).
17. L. Brillouin, Wave Propagation and Group Velocity, New York: Academic Press (1960), pp. 113-130.
18. L. J. Spitzer, Physics of Fully Ionized Gases, London: Interscience (1956), p. 94.
19. P. A. Sturrock, "Kinematics of Growing Waves," Phys. Rev., 112 (1958), p. 1488.
20. W. D. Getty, "Investigation of Electron-Beam Interaction with a Beam-generated Plasma," M. I. T. Technical Report 407, Section II (1963).
21. R. D. Agnew, Differential Equations, New York: McGraw-Hill (1960), p. 291.

22. M. A. Allen and G. S. Kino, "Beam-Plasma Amplifiers," Report No. 833, Microwave Laboratory, Stanford University (July 1961), p.15.
23. T. H. Stix, Theory of Plasma Waves, New York: McGraw-Hill (1962), p. 178-181.

APPENDIX A. BOLTZMANN AND
BOLTZMANN TRANSPORT EQUATIONS

1. Boltzmann's Equation

Consider the distribution function f_i . This specifies the number of particles of type i at a given point $(\underline{x}, \underline{v})$ in phase space. Using Liouville's theorem that the total derivative of the distribution function along a flow line in the phase space is zero, we get

$$f_i(t) = f_i(t + dt) \quad (\text{A.1})$$

Including the effects of collisions, we get

$$f_i(\underline{x} + \underline{x} dt, \underline{v} + \underline{v} dt, t + dt) - f_i(\underline{x}, \underline{v}, t) = \left(\frac{\partial f_i}{\partial t} \right)_c dt \quad (\text{A.2})$$

Expanding $f_i(\underline{x}, \underline{v}, t)$ about t , gives

$$\begin{aligned} f_i(t) + \frac{\partial f_i}{\partial t} dt + \frac{\partial f_i}{\partial \underline{x}_i} \cdot \frac{\partial \underline{x}_i}{\partial t} dt + \frac{\partial f_i}{\partial \underline{v}_i} \cdot \frac{\partial \underline{v}_i}{\partial t} dt + \text{higher order terms in } dt \\ = \left(\frac{\partial f_i}{\partial t} \right)_c dt \quad (\text{A.3}) \end{aligned}$$

Collecting terms of order dt and letting $dt \rightarrow 0$, gives Boltzmann's equation,

$$\left(\frac{\partial}{\partial t} + \underline{v} \cdot \nabla + \underline{a} \cdot \nabla_{\underline{v}} \right) f_i = \left(\frac{\partial f_i}{\partial t} \right)_c \quad (\text{A.4})$$

2. Boltzmann's Transport Equation

When the time scale is greater than the time between collisions, the particle density, average velocity, and energy can be treated directly, i. e., without velocity distribution functions, since these quantities are invariant during a collision. Integrating Equation (A.4) over velocity space, we get

$$\frac{\partial n_i}{\partial t} = -\nabla \cdot (n_i \underline{v}_i) + I_i \quad , \quad (\text{A.5})$$

where I_i represents net density of particle creation, and \underline{v}_i is an average velocity defined by

$$\underline{v}_i = \frac{1}{n_i} \int \underline{u}_i f_i(\underline{u}_i) d^3 u_i \quad . \quad (\text{A.6})$$

The right-hand side of Equation (A.5) represents the net particle flux from a differential volume element. Contributions to this term can arise in three ways: (1) as a result of diffusion in co-ordinate space, $+\nabla \cdot \underline{D} \cdot n$; (2) as a result of particle mobility in an electric field (akin to a diffusion type process), $-\nabla \cdot \underline{\mu} \cdot \underline{E} n$; (3) as a result of diffusion in velocity space, $-\frac{q_i \underline{E}}{m v}$ and $-\frac{v n}{L}$. (Note that these two terms are usually small compared to the rest, unless the mean-free path is greater than or approximately equal to a typical dimension of the geometry).

APPENDIX B. DERIVATION
OF POISSON'S EQUATION

Using the quasi-static approximation, $H_1 = 0$, the electric field can be derived from a scalar potential. The set of equations to be solved is:

$$\underline{E}_1 = -\nabla\phi \quad , \quad (B.1)$$

$$\nabla \cdot \underline{E}_1 = \rho_1/\epsilon_0 \quad , \quad (B.2)$$

$$d_t n_{11} + \nabla \cdot (n_{01} \underline{V}_{11} + n_{11} \underline{V}_{01}) = 0 \quad , \quad (B.3)$$

$$d_t n_{12} + \nabla \cdot (n_{02} \underline{V}_{12} + n_{12} \underline{V}_{02}) = 0 \quad , \quad (B.4)$$

$$\begin{aligned} d_t \underline{V}_{11} + (\underline{V}_{01} \cdot \nabla) \underline{V}_{11} + (\underline{V}_{11} \cdot \nabla) \underline{V}_{01} \\ = -\eta (\underline{E}_1 + \underline{V}_{11} \times \underline{B}_0 + \underline{V}_{01} \times \underline{B}_1) \quad , \end{aligned} \quad (B.5)$$

$$\begin{aligned} d_t \underline{V}_{12} + (\underline{V}_{02} \cdot \nabla) \underline{V}_{12} + (\underline{V}_{12} \cdot \nabla) \underline{V}_{02} \\ = -\eta (\underline{E}_1 + \underline{V}_{12} \times \underline{B}_0 + \underline{V}_{02} \times \underline{B}_1) \quad , \end{aligned} \quad (B.6)$$

$$\rho_1 = -e (n_{11} + n_{12}) \quad (B.7)$$

The following conditions apply to the beam-plasma problem:

$$\begin{aligned}
 \underline{H}_1 &= 0 & \nabla \cdot \underline{V}_{02} &= 0 & d_t &= j\omega \\
 \underline{V}_{01} &= 0 & E_\theta &= 0 & d_z &= -j\beta \\
 \underline{V}_{02} &= \hat{k} V_0 & d_\theta &= 0 & \underline{B}_0 &= \hat{k} B_0
 \end{aligned} \tag{B.8}$$

Using Equation (B.1) in Equation (B.2) gives

$$(\nabla \cdot \nabla) \phi = -\frac{\rho_1}{\epsilon_0} \tag{B.9}$$

The ∇ in cylindrical co-ordinates is written

$$\begin{aligned}
 \nabla \psi &= d_r \psi \hat{r} + \frac{1}{r} d_\theta \psi \hat{\theta} + d_z \psi \hat{k} \\
 (\nabla \cdot \nabla) \psi &= \frac{1}{r} d_r (r d_r \psi) + \frac{1}{r^2} d_{\theta\theta} \psi + d_{zz} \psi \\
 \nabla \cdot \underline{A} &= \frac{1}{r} d_r (r A_r) + \frac{1}{r} d_\theta A_\theta + d_z A_z
 \end{aligned} \tag{B.10}$$

Using Equations (B.8), (B.10) in (B.3), (B.4), (B.5), (B.6), and (B.9), we get

$$j\omega n_{11} + V_{11r} d_r n_{01} + n_{01} \frac{1}{r} d_r (r V_{11r}) + n_{01} (-j\beta) V_{11z} = 0 \tag{B.11}$$

$$j\omega n_{12} + V_{12r} d_r n_{02} + n_{02} \frac{1}{r} d_r (r V_{12r}) + n_{01} (-j\beta) V_{12z} + V_{01} (-j\beta) n_{12} = 0 \tag{B.12}$$

$$j\omega \underline{V}_{11} = -\eta \left(-\nabla \phi + \underline{V}_{11} \times \underline{B}_0 \right) \tag{B.13}$$

$$j\omega \underline{V}_{12} + V_0 (-j\beta) \underline{V}_{12} = -\eta \left(-\nabla \phi + \underline{V}_{12} \times \underline{B}_0 \right) \tag{B.14}$$

$$\left(d_{rr} + \frac{1}{r} d_r - \beta^2\right) \phi = -\frac{\rho_1}{\epsilon_0} \quad (\text{B. 15})$$

Next, we solve for the small-signal velocities in terms of the scalar potential. Expanding Equation (B. 14), we get

$$\begin{bmatrix} V_{12r} \\ V_{12\theta} \\ V_{12z} \end{bmatrix} = \frac{\begin{bmatrix} (d_r \phi + V_{1\theta} B_0) \\ -V_{1r} B_0 \\ -j\beta\phi \end{bmatrix}}{j\omega \left(1 - \frac{\beta}{\beta_e}\right)}$$

$$\begin{bmatrix} 1 & -j \frac{\omega_c}{\omega \left(1 - \frac{\beta}{\beta_e}\right)} & 0 \\ j \frac{\omega_c}{\omega \left(1 - \frac{\beta}{\beta_e}\right)} & 1 & 0 \\ 0 & 0 & 1 \end{bmatrix} \cdot \underline{V}_{12} = \frac{-\eta \begin{bmatrix} d_r \phi \\ 0 \\ -j\beta\phi \end{bmatrix}}{j\omega \left(1 - \frac{\beta}{\beta_e}\right)}$$

$$\underline{V}_{12} = \frac{\begin{bmatrix} 1 & \frac{j\omega_c}{\omega \left(1 - \frac{\beta}{\beta_e}\right)} & 0 \\ -\eta \frac{-j\omega_c}{\omega \left(1 - \frac{\beta}{\beta_e}\right)} & 1 & 0 \\ 0 & 0 & 0 \end{bmatrix} \begin{bmatrix} d_r \phi \\ 0 \\ -j\beta\phi \end{bmatrix}}{j\omega \left(1 - \frac{\beta}{\beta_e}\right) D} \quad (\text{B. 16})$$

The following identifications are made:

$$\omega_c = \eta B_0 \quad ,$$

$$\beta_e = \frac{\omega}{V_0} \quad ,$$

$$D = 1 - \frac{\omega_c^2}{\omega^2 \left(1 - \frac{\beta}{\beta_e}\right)^2}$$

Following a similar procedure for Equation (B.13), we get

$$\underline{V}_{11} = \frac{\eta \begin{bmatrix} 1 & \frac{j\omega_c}{\omega} & 0 \\ -\frac{j\omega_c}{\omega} & 1 & 0 \\ 0 & 0 & 1 - \frac{\omega_c^2}{\omega^2} \end{bmatrix} \begin{bmatrix} d_r \phi \\ 0 \\ -j\beta \phi \end{bmatrix}}{j\omega \left(1 - \frac{\omega_c^2}{\omega^2}\right)} \quad (B.17)$$

Substituting Equation (B.16) and (B.17) into Equations (B.11) and (B.12), we solve for the small-signal electron densities. Expanding Equation (B.12), we get

$$j\omega n_{12} + \left(\frac{-\eta}{j\omega}\right) \frac{(d_r \phi)(d_r n_{02})}{\left(1 - \frac{\beta}{\beta_e}\right) D} + V_0 (-j\beta) n_{12} + \left(\frac{-\eta}{j\omega}\right) \frac{(-j\beta \phi)(-j\beta) n_{02}}{\left(1 - \frac{\beta}{\beta_e}\right)} + \left(\frac{-\eta}{j\omega}\right) \frac{n_{02} \left(d_{rr} + \frac{1}{r} dr\right) \phi}{\left(1 - \frac{\beta}{\beta_e}\right) D} = 0 \quad ,$$

$$n_{12} = \frac{\eta \left[\beta^2 n_{02} \phi - \frac{(d_r n_{02})(d_r \phi)}{D} - \frac{n_{02} \left(d_{rr} + \frac{1}{r} dr \right) \phi}{D} \right]}{(j\omega)^2 \left(1 - \frac{\beta}{\beta_e} \right)^2} \quad (B.18)$$

Following a similar procedure with Equation (B.11), we get

$$n_{11} = \frac{\eta}{(j\omega)^2} \left[\beta^2 n_{01} \phi - \frac{(d_r n_{01})(d_r \phi)}{\left(1 - \frac{\omega c}{\omega^2} \right)} - n_{01} \frac{\left(d_{rr} + \frac{1}{r} dr \right) \phi}{\left(1 - \frac{\omega c}{\omega^2} \right)} \right] \quad (B.19)$$

Substituting Equation (B.7), (B.18), and (B.19) into Equation (B.15), we get

$$\begin{aligned} \left(d_{rr} + \frac{1}{r} d_r - \beta^2 \right) \phi = & \\ \frac{e}{\epsilon_0} \frac{\eta}{(j\omega)^2} \left\{ \beta^2 \left[n_{01} + \frac{n_{02}}{\left(1 - \frac{\beta}{\beta_e} \right)^2} \right] \phi - \left[\frac{d_r n_{01}}{\left(1 - \frac{\omega c}{\omega^2} \right)} + \frac{d_r n_{02}}{\left(1 - \frac{\beta}{\beta_e} \right)^2} \right] d_r \phi \right. & \\ \left. - \left[\frac{n_{01}}{\left(1 - \frac{\omega c}{\omega^2} \right)} + \frac{n_{02}}{\left(1 - \frac{\beta}{\beta_e} \right)^2} \right] \left(d_{rr} + \frac{1}{r} d_r \right) \phi \right\} & \end{aligned}$$

$$\begin{aligned}
& \left[d_{rr} + \frac{1}{r} d_r - \beta^2 \right] \phi = \\
& -\beta^2 \left[\frac{\hat{n}_{01}}{a^2} + \frac{d_2^2 \hat{n}_{02}}{a^2 \left(1 - \frac{\beta}{\beta_e}\right)^2} \right] \phi + \left[\frac{d_r \hat{n}_{01}}{a^2 - d_1^2} + d_2^2 \frac{d_r \hat{n}_{02}}{a^2 \left(1 - \frac{\beta}{\beta_e}\right)^2 - d_1^2} \right] d_r \phi \\
& + \left[\frac{\hat{n}_{01}}{a^2 - d_1^2} + \frac{d_2^2 \hat{n}_{02}}{a^2 \left(1 - \frac{\beta}{\beta_e}\right)^2 - d_1^2} \right] \left(d_{rr} + \frac{1}{r} d_r \right) \phi, \\
& \left(\left[1 - \frac{\hat{n}_{01}}{a^2 - d_1^2} - \frac{\hat{n}_{02} d_2^2}{a^2 \left(1 - \frac{\beta}{\beta_e}\right)^2 - d_1^2} \right] d_{rr} \right. \\
& + \left. \left\{ 1 - \frac{\hat{n}_{01}}{a^2 - d_1^2} - \frac{\hat{n}_{02} d_2^2}{a^2 \left(1 - \frac{\beta}{\beta_e}\right)^2 - d_1^2} - r \left[\frac{d_r \hat{n}_{01}}{a^2 - d_1^2} + \frac{d_r \hat{n}_{02}}{a^2 \left(1 - \frac{\beta}{\beta_e}\right)^2 - d_1^2} \right] \right\} \frac{1}{r} d_r \right. \\
& \left. + \left\{ -\beta^2 \left[1 - \frac{\hat{n}_{01}}{a^2} - \frac{d_2^2 \hat{n}_{02}}{a^2 \left(1 - \frac{\beta}{\beta_e}\right)^2} \right] \right\} \right) \phi = 0 \quad (B.20)
\end{aligned}$$

The following identifications are made:

$$\begin{aligned}
a &= \frac{\omega}{\omega_{pp}} & \omega_{pp}^2 &= \frac{e^2}{m\epsilon_0} \eta_{01} \Big|_{\max} \\
d_1 &= \frac{\omega_c}{\omega_{pp}} & \omega_{pb}^2 &= \frac{e^2}{m\epsilon_0} \eta_{02} \Big|_{\max}
\end{aligned} \quad (B.21)$$

$$d_2 = \frac{\omega_{pb}}{\omega_{pp}}$$

$$d_3 = \frac{v_o}{r_o \omega_{pp}}$$

$$\hat{\eta}_{01} = \left. \frac{\eta_{01}}{\eta_{01}} \right|_{\max}$$

$$\hat{\eta}_{02} = \left. \frac{\eta_{02}}{\eta_{02}} \right|_{\max}$$

(B. 21)

APPENDIX C. COMPUTER PROGRAM
FOR THE INHOMOGENEOUS CASE

1. Derivation of Parameters

The differential equation is

$$D(R, v) d_{vv} \phi(v) + \left[\frac{D(R_1 v) + E(R_1 v)}{v} \right] d_v \phi(v) + A(R_1 v) \phi(v) = 0 \quad , \quad (C.1)$$

subject to the initial conditions,

$$\begin{aligned} \phi(0) &= 0 \quad , \\ d_v \phi(0) &= 0 \quad . \end{aligned} \quad (C.2)$$

The complex parameter R is to be chosen such that

$$\phi(v) \Big|_{v=1} = 0 \quad .$$

Expanding in real and imaginary parts we get

$$\begin{aligned} \phi &= \phi_1 + j \phi_2 \quad , \\ D &= D_1 + j D_2 \quad , \\ E &= E_1 + j E_2 \quad , \\ A &= A_1 + j A_2 \quad , \\ R &= R_1 + j R_2 \quad . \end{aligned} \quad (C.3)$$

Substituting Equation (C.3) into Equation (C.1), we get a system of two real, coupled, linear, second-order differential equations:

$$\begin{aligned}
& F_1(R_1, R_2, v) d_v \phi_1(v) + F_2(R_1, R_2, v) d_v \phi_1(v) + F_3(R_1, R_2, v) d_v \phi_2(v) \\
& + F_4(R_1, R_2, v) \phi_1(v) + F_5(R_1, R_2, v) \phi_2(v) = 0 \quad , \quad (C.4)
\end{aligned}$$

$$\begin{aligned}
& F_1(R_1, R_2, v) d_v \phi_2(v) + F_2(R_1, R_2, v) d_v \phi_2(v) - F_3(R_1, R_2, v) d_v \phi_1(v) \\
& - F_4(R_1, R_2, v) \phi_2(v) - F_5(R_1, R_2, v) \phi_1(v) = 0 \quad . \quad (C.5)
\end{aligned}$$

The boundary conditions are:

$$\begin{aligned}
\phi_1(0) &= 1.0 & \phi_2(0) &= 0 \\
d_v \phi_1(0) &= 0 & d_v \phi_2(0) &= 0 \\
\phi_1(1) &= 0 & \phi_2(1) &= 0 \quad . \quad (C.6)
\end{aligned}$$

The F_i ($i=1, 2, 3, 4, 5$) are given by

$$\begin{aligned}
F_1 &= D_1^2 + D_2^2 \quad , \\
F_2 &= F_1 + F_1 D_1 + F_2 D_2 \quad , \\
F_3 &= (F_1 D_2 - F_2 D_1) / v \quad , \quad (C.7) \\
F_4 &= D_1^2 \lambda_1 + D_2^2 \lambda_2 \quad , \\
F_5 &= D_2^2 \lambda_1 - D_1^2 \lambda_2 \quad .
\end{aligned}$$

The coefficients F_i are the v -dependent, v -independent, v - and R -dependent, R -independent, R -dependent ones. This is because the average velocity v is held constant during interdiffusion.

$$D_1 = 1 - \frac{e^{-(a_1 r_o v)^{q_1}}}{C_1} - CR_1 e^{-(a_2 r_o v)^{q_2}} - CR_{1A} e^{-(a_3 r_o v)^{q_3}} \quad (C.8)$$

$$D_2 = CR_2 e^{-(a_2 r_o v)^{q_2}} + CR_{2A} e^{-(a_3 r_o v)^{q_3}} \quad (C.9)$$

$$C_1 = a^2 - d_1^2 \quad ,$$

$$CR_1 = \frac{R_1^2 - R_2^2 - \frac{d_1^2}{d_2^2}}{\left(R_1^2 - R_2^2 - \frac{d_1^2}{d_2^2}\right) + (2R_1 R_2)^2} \quad (C.10)$$

$$CR_{1A} = \beta CR_1 \quad ,$$

$$E_1 = CR_{33} (a_1 r_o v)^{q_1} e^{-(a_1 r_o v)^{q_1}} + CR_3 (a_2 r_o v)^{q_2} e^{-(a_2 r_o v)^{q_2}} + CR_{3A} (a_3 r_o v)^{q_3} e^{-(a_3 r_o v)^{q_3}} \quad (C.11)$$

$$E_2 = CR_4 (a_2 r_o v)^{q_2} e^{-(a_2 r_o v)^{q_2}} + CR_{4A} (a_3 r_o v)^{q_3} e^{-(a_3 r_o v)^{q_3}} \quad (C.12)$$

$$CR_{33} = \frac{q_1}{a^2 - d_1^2} ,$$

$$CR_3 = q_2 CR_1 ,$$

$$CR_{3A} = q_3 CR_{1A} , \quad (C. 13)$$

$$A_1 = CR_5 - CR_{53} e^{-(a_1 r_o v)^{q_1}} - CR_{567} e^{-(a_2 r_o v)^{q_2}} - CR_{567A} e^{-(a_3 r_o v)^{q_3}} , \quad (C. 14)$$

$$A_2 = CR_7 - CR_{73} e^{-(a_1 r_o v)^{q_1}} - CR_{765} e^{-(a_2 r_o t)^{q_2}} - CR_{765A} e^{-(a_3 r_o t)^{q_3}} , \quad (C. 15)$$

$$CR_5 = \frac{a^2}{d_3^2} \left[\left(1 + R_1 \frac{d_2^2}{a} \right)^2 - \left(R_2 \frac{d_2^2}{a} \right)^2 \right] ,$$

$$CR_7 = \frac{a^2}{d_3^2} \left[2 R_2 \frac{d_2}{a} \left(1 + R_1 \frac{d_2}{a} \right) \right] ,$$

$$CR_{53} = CR_5 / a^2 ,$$

$$CR_{73} = CR_7 / a^2 ,$$

$$CR_{567} = \frac{CR_5 (R_1^2 - R_2^2) + 2 R_1 R_2 CR_7}{(R_1^2 - R_2^2)^2 + (2 R_1 R_2)^2} ,$$

$$CR_{567A} = \beta CR_{567} ,$$

$$CR_{765} = \frac{CR_5(2R_1R_2) - CR_7(R_1^2 - R_2^2)}{(R_1^2 - R_2^2)^2 + (2R_1R_2)^2}$$

$$CR_{765A} = \beta CR_{765} \quad (C. 16)$$

The integration procedure requires that the real and imaginary parts of $d_{vv}\phi(0)$ be known. To find these we write a power series expansion in v about the origin:

$$\begin{aligned} \phi(v) &= 1 + (a_1 + ja_2)t^2 + \dots + \\ \phi^{(1)}(v) &= 2(a_1 + ja_2)t + \dots + \\ \phi^{(11)}(v) &= 2(a_1 + ja_2) + \dots + \end{aligned} \quad (C. 17)$$

thus

$$d_{vv}\phi(0) = 2a_1 + j2a_2$$

To find a_1, a_2 we substitute Equation (C. 17) into Equation (C. 1):

$$\begin{aligned} 2(2a_1 + j2a_2) \left[1 - \frac{1}{C_1} - CR_1 - CR_{1A} + j(CR_2 + CR_{2A}) \right] \\ + \left[CR_5 - CR_{53} - CR_{567} - CR_{567A} + (CR_7 - CR_{73} \right. \\ \left. - CR_{765} - CR_{765A}) \right] = 0 \end{aligned}$$

$$a_1 = \frac{\left[CON 1 \left(1 - \frac{1}{C_1} - CR_1 - CR_{1A} \right) + CON 2 \left(CR_2 + CR_{2A} \right) \right]}{4 \left[\left(1 - \frac{1}{C_1} - CR_1 \right)^2 + (CR_2 + CR_{2A})^2 \right]} \quad (C. 18)$$

$$a_2 = \frac{\text{CON } 2 \left(1 - \frac{1}{C_1} - \text{CR}_1\right) - \text{CON } 1 \left(\text{CR}_2 + \text{CR}_{2A}\right)}{4 \left[\left(1 - \frac{1}{C_1} - \text{CR}_1\right)^2 + \left(\text{CR}_2 + \text{CR}_{2A}\right)^2 \right]}$$

$$\text{CON } 1 = -\text{CR}_5 + \text{CR}_{53} + \text{CR}_{567} + \text{CR}_{567A}$$

$$\text{CON } 2 = -\text{CR}_7 + \text{CR}_{73} \quad \text{CR}_{765} - \text{CR}_{765A} \quad (C. 19)$$

2. Computer Program

a. Elements of Program

The computer program consists of seven subprograms.

1. DELMAG

This is the main program. It reads the input data and computes the constants that are independent of R . This program also regulates the iterative search procedure for the value of R that minimizes $|\phi(1)|^2$. Starting from a given value of R , it computes increments Δe_1 until $|\phi(1)|$ is minimized.

2. RUNGE

This is a standard routine designed to integrate a system of differential equations by the Runge-Kutta method. First the system is reduced to the following form:

$$\begin{aligned} \frac{dz_1}{dv} &= f_1(z_1, z_2, \dots, z_n, v) \\ &\vdots \\ \frac{dz_n}{dv} &= f_n(z_1, z_2, \dots, z_n, v) \end{aligned} \quad (C. 20)$$

For one case (1) of Equation (C.4) becomes

$$\begin{aligned}
 d_v z_1 &= d_v \phi_1 = z_3 \quad , \\
 d_v z_2 &= d_v \phi_2 = z_4 \quad , \\
 d_v z_3 &= d_{vv} \phi_1 = -[F_2 z_3 + F_3 z_4 + F_4 z_1 + F_5 \cdot z_2] / F_1 \quad , \\
 d_v z_4 &= d_{vv} \phi_2 = -[F_2 z_4 - F_3 z_3 - F_4 z_2 - F_5 z_1] / F_1 \quad . \quad (C.24)
 \end{aligned}$$

Given the starting values $Z_i(0)$, this routine integrates Equation (C.24) from $v = 0$ to $v = 1.0$. During a typical step in this program, say from t to $t + \Delta$, the routine branches out to another subprogram called DERIV, which computes $d_v z_i$, four times. During these times, the values of z_i are stored in temporary storage.

3. DERIV

This subprogram calculates the derivatives $d_v z_i$ as given in Equation (C.24). If $v = 0$, then f_3 is set equal to $d_{vv} \phi_1(0) = 2a_1$ and f_4 is set equal to $d_{vv} \phi_2(0) = 2a_2$, since in the normal evaluation of $d_{vv} \phi$, there is a division by v .

A test is made on the variable N (the number of equations in the system), which is usually equal to four. If the magnitude of F_1 is less than 10^{-5} , the value of N will be set equal to two. For N equal to two, a reduced system of equations is integrated (see EXPRESS).

4. EXPRESS

This subprogram is entered from RUNGE when $v = 0.0$ and $v_2 = 1.0$. When the value for R that minimizes $|\phi(1)|$ is found, this program is entered for all v , so that every step in the integration is printed for this final calculation.

The main function of this program is to print a line of output values of $v_1\phi_1, \phi_2, d_v\phi_1, d_v\phi_2, d_{vv}\phi_1, d_{vv}\phi_2, D_1, D_2$ at the proper values of v . It also tests the magnitude of F_1 against 10^{-1} . If it is less, then Equation (C. 21) is reduced to the following system of two first-order equations:

$$\begin{aligned}d_v\phi_1 &= -(P_1\phi_1 + P_2\phi_2)/P_3, \\d_v\phi_2 &= -(P_1\phi_2 - P_2\phi_1)P_3, \end{aligned} \tag{C.22}$$

$$\begin{aligned}P_1 &= F_2F_4 + F_3F_5, \\P_2 &= F_2F_5 - F_3F_4, \\P_3 &= F_2^2 + F_3^2.\end{aligned} \tag{C.23}$$

This system is integrated over the next interval Δv . The interval is divided into ten steps of length $\Delta v/10$, and after every 10 steps the magnitude of F_1 is tested again. When the magnitude of F_1 is greater than 10^{-5} , then N is reset to four and the integration interval is reset to Δv .

6. PHICON

This routine is entered from the main program DEIMAG. Its function is to set up all the necessary starting conditions, enter RUNGE

to integrate Equation (C. 21) for a particular value of R , and to compute $\phi(1)^2$. It also tests $|\phi(1)|$ to see whether the search procedure should be stopped.

6. RCON

This is an auxiliary routine entered from PHICON. Given a particular value of R , it computes all of the R -dependent constants used in computing the derivatives (namely CR_1, CR_2, CR_3, \dots , etc.).

7. TCALC

This is an auxiliary routine entered from DERIV. For a particular value of v , it uses the stored R -dependent constants and computes $D_1, D_2, E_1, E_2, A_1, A_2, F_1, F_2, F_3, F_4, F_5$.

b. Search Procedure

An initial choice for R is given the computer along with all other input data. From this, four alternate starting values for R are calculated and stored for future reference. Let A_i be the magnitude of $\phi(1)$ squared after the i^{th} integration. PHICON supplies A_i to DEIMAG, but first tests it against .01. If it is smaller, DEIMAG directs EXPRESS to print the output; if it is larger, DEIMAG stores A_i , changes R by Δ , compares A_{i+1} with A_i . If A_{i+1} is larger than .01, the increment in R changes direction by π or $\pi/2$ radians, gets larger or smaller depending on the previous values for A and Δ . The search ends when either Δ is so small that increased accuracy would not justify the added computer time, or when A_i is less than .01.

Superimposed on the above procedure is an additional routine that prevents the computer from searching a nonconvergent region of the R plane. In working with the program, it was noticed that if $|\phi_1(v)|$ was greater than one near $v=0$, no good values of R were found in that region. So, a test is made during the integration procedure. If $|\phi_1(.02)|$ is greater than one for two consecutive values of R , DEIMAG selects an alternate starting value for R that was held in storage from an earlier part of the program. DEIMAG will go through this alternate procedure four times, if necessary. The fifth time, it will go on to the next input data card. The flow chart shown in Figure C. 1 for DEIMAG gives a more sequential explanation of the search procedure.

c. Input Preparation

There are two programs using this Equation (C. 1). The first is called the "regular" program, and is the one with the automatic search for R . The second is called the "grid" program, and does not have the automatic search for R . Instead it takes a rectangular grid in the complex R plane and transforms it into a corresponding area in the complex ϕ plane.

The regular program has two types of input data cards, Card types R-1 and R-2.

Card Type R-1

Columns	1-7	8-14	15-21	22-28	29-35
Data	d_1	d_2	d_3	$a_1 r_0$	$a_2 r_0$

Columns	36-42	43-49	50-56	57-62	63-69
Data	$a_3 r_0$	q_1	q_2	q_3	β

Card Type R-2

Columns	1-10	11-20	21-30	34-35
Data	a	R_1	R_2	1, -1, 0

The values in columns 34 and 35 of card type R-2 indicate procedure. No. 1 means that the next input data card must be of card type R-1. No. 0 means that the value at R_1, R_2 on this card must be used as the starting point for R . No. -1 means that the values of R_1, R_2 derived from the last input data card will be used as the starting values for R_1, R_2 . The grid program also has two types of input data cards, the first of which is identical with card type R-1; the second is card type G-2.

Card Type G-2

Columns	1-10	11-20	21-30	31-40	41-50	51-60
Data	a	R_1	R_2	DGX	DGY	EPS

Card type G-2 will generate a grid in the R plane whose corners occupy the following co-ordinates:

$$(R_1, R_2); (R_1, R_2 + DGY \times EPS); (R_1 + DGX \times EPS); (R_1 + DGX \times EPS, R_2 + DGY \times EPS) .$$

```

PROGRAM DEIMAG
STORE1 = 100.0
STORE2 = 100.0
DELTA = 0.01
1 READ 100,S1,S2,D3,A1R0,A2R0,01,02
100 FORMAT (7F10.6)
6000 READ 6001,BETA,A3R0,03
6001 FORMAT (3F10.6)
999 FORMAT (13)
PRINT 3000, S1,S2,D3,A1R0,A2R0,01,02
3000 FORMAT (1X,7F10.5)
BETA = 0.0 - BETA
PRINT 605,BETA,A3R0,03
605 FORMAT (2X,3F10.6)
IF (S1 -100.0) 555,556,556
556 STOP
555 CONTINUE
FL = 1.0/DELTA
2 READ 101,ALPHA,R1,R2,111
KC = 0
101 FORMAT (3F10.5,15)
PRINT 3001, ALPHA
3001 FORMAT (8H ALPHA =,F10.5)
CALCULATIONS FOR R-INDEPENDENT CONSTANTS
IF (111) 3005,2003,1
3005 R1 = STORE1
R2 = STORE2
STORE1 = 100.0
STORE2 = 100.0
2005 IF (R1 -100.0) 2003,2,2
2004 STOP
2003 CONTINUE
RAB = R1*R1 + R2*R2
ADD = 0.01*SQRTF(RAB)
PEST = 0.01*ADD
R1SET(1) = R1/2.0
R1SET(2) = R1/2.0
R2SET(1) = R2/2.0
R2SET(2) = R2/2.0
PRINT 998, R2SET(2)
998 FORMAT ( F10.5/2)
LHACK = 0
ISET = 1
H = 1.0
333 RR(1) = R1
RR(2) = R2
RAB = R1*R1 + R2*R2
RAB = SQRTF(RAB)
DEL1 = RAB*0.01
DEL2 = DEL1
KC = KC + 1
CALL PHICON
IF (LBACK) 21,301,300
301 CONTINUE
COMP = PAB
KEY = 1
105 DL(1) = DEL1
DL(2) = DEL2
101 RR(KEY) = RR(KEY) + DL(KEY)
R1 = RR(1)
R2 = RR(2)
KC = KC + 1
PRINT 999,KC
IF (KC - 42) 307,300,300
307 CONTINUE
CALL PHICON
IF (LBACK) 21,303,300
303 CONTINUE
IF (PAB-COMP) 14,11,11
11 RR(KEY) = RR(KEY) - 2.0*DL(KEY)
DL(KEY) = -DL(KEY)
R1 = RR(1)
R2 = RR(2)
DEL1 = DL(1)
DEL2 = DL(2)
KC = KC + 1
PRINT 999,KC
IF (KC - 42) 306,300,300
306 CONTINUE
CALL PHICON
IF (LBACK) 21,304,300
304 CONTINUE
IF (PAB-COMP) 14,14,13
13 RR(KEY) = RR(KEY) - DL(KEY)
GO TO 200
14 TEST = (COMP-PAB)/DL(KEY)
COMP = PAB
IF (TEST-H) 100,171,101
100 TDEL = 2.0*ABSF(DL(KEY))
IF (TDEL-RAB) 103,102,102
103 DEL1 = 2.0*DEL1
DEL2 = 2.0*DEL2
GO TO 105
102 DLL1 = 0.01*RAB
DFL2 = DEL1
10 IF (KEY-1) 106,107,106
106 KEY = 1
GO TO 105
107 KEY = 2
GO TO 105
200 DL(KEY) = DL(KEY)*(-0.1)
TST1 = ABSF(DL(1))
TST2 = ABSF(DL(2))
DEL1 = DL(1)
DEL2 = DL(2)
IF (MAX1F(TST1,TST2) - PEST) 21,21,10
21 L = 1
KC = KC + 1
CALL PHICON
304 STORE1 = R1
STORE2 = R2
GO TO 2
300 R1 = R1SET(ISET)
R2 = R2SET(ISET)
KC = 0
ISET = ISET + 1
IF (ISET-3) 302,302,2
302 a STOP
END

```

FIGURE C. 1. Program Deimag

APPENDIX D. CORRECTION TERM FOR
MAXWELLIAN DISTRIBUTION IN LONGITUDINAL VELOCITY

We can treat the effects of nonsingular longitudinal- and transverse-velocity distributions separately, since these modes are not coupled to each other in Boltzmann's equation. From Equation (21), evaluating the contribution of the axial variation of velocity to the particle density variation, we get

$$n_1 = \int_{-\infty}^{\infty} f_1(v_z) dv_z = \int_{-\infty}^{\infty} \frac{-e E_{1z}}{m(\omega - \beta v_z)} \frac{\partial}{\partial v_z} [f_0(v_z)] dv_z \quad (D.1)$$

For a Maxwellian distribution,

$$f_0(v_z) = \pi^{-1/2} v_T^{-1} e^{-(v_z - v_0)^2 / v_T^2}$$

$$n_1 = (-2) \frac{e}{m} j \pi^{-1/2} E_{1z} v_T^{-3} \int_{-\infty}^{\infty} \frac{(v_z - v_0) e^{-(v_z - v_0)^2 / v_T^2}}{(\omega - \beta v_z)} dv_z \quad (D.2)$$

where $v_T = (2kT/m)^{1/2}$. If we set

$$F_P = j\beta \pi^{-1/2} \int_{-\infty}^{\infty} \frac{v_z^P}{\omega - \beta v_z} e^{-(v_z - v_0)^2 / v_T^2} dv_z \quad (D.3)$$

then

$$n_1 = \frac{-e}{m\beta} \left[2v_T^{-3} (F_1 - v_0 F_0) \right]$$

$$n_1 = \frac{-e}{m} j \frac{\beta}{\omega^2 \left(1 - \frac{\beta}{\beta_e}\right)^2} \left[1 + \frac{3}{2} \frac{\delta^2}{\left(1 - \frac{\beta}{\beta_e}\right)^2} \right] \quad (\text{D.5})$$

PLASMA DIAGNOSTICS

D. M. Kerr

ABSTRACT

This report describes the design and use of singly re-entrant cavities in an electron-beam hydrogen-plasma system. The cavities serve as the input and output coupling structures of a beam-plasma amplifier and, in addition, they are used to investigate the properties of the plasma discharge. Perturbation of a resonant cavity by a plasma is discussed and equations are obtained relating the shifts in resonant frequency and cavity Q to the average electron density and collision frequency. Some typical experimental results are given and a linear relationship is found between resonant frequency shift and discharge current.

TABLE OF CONTENTS

	Page
I. INTRODUCTION	1
II. CAVITY DESIGN	1
III. MEASUREMENT OF CAVITY Q	6
A. CASE 1. SHUNT LOSSES	14
B. CASE 2. SERIES LOSSES	14
C. CASE 3. SERIES AND SHUNT LOSSES	15
IV. MEASUREMENT OF $\mu^2 R_{sh}/Q_o$	18
V. COLD TEST RESULTS	25
VI. FREQUENCY SHIFT OF CAVITY MODES IN PRESENCE OF A PLASMA	26
VII. PLASMA DIAGNOSIS	32
VIII. EXPERIMENTAL RESULTS	36
IX. REFERENCES	39

I. INTRODUCTION

Two singly re-entrant cavities of the type ordinarily used in klystron amplifiers were designed and tested for use in the study of an electron-beam hydrogen-plasma system. Their primary purpose was to serve as the input and output coupling structures for a beam-plasma amplifier. It was also thought that they might be used to diagnose the properties of the plasma and, in particular, to determine the electron density and collision frequency. The following sections describe the design and cold testing of the cavities and their use as diagnostic tools; and presents the experimental results obtained.

II. CAVITY DESIGN

The beam-plasma system operates at about 3000 Mc/s with a 5-kv electron beam. These specifications together with certain structural details of the vacuum system, fixed the cavity dimensions. Figure 1 shows the quantities considered. The inside diameter of the drift tube r_0 was fixed by the size of the hollow cathodes used to generate the plasma, which were 0.500 in. in diameter. The stainless steel rods that supported the plasma cathodes and cavities placed a restriction on the outside diameter of the cavities of 2.50 in. The copper tubing for the outer cavity wall had an outside diameter of 2.00 in. and an inside diameter of 1.75 in.; that for the drift tube had an outside diameter

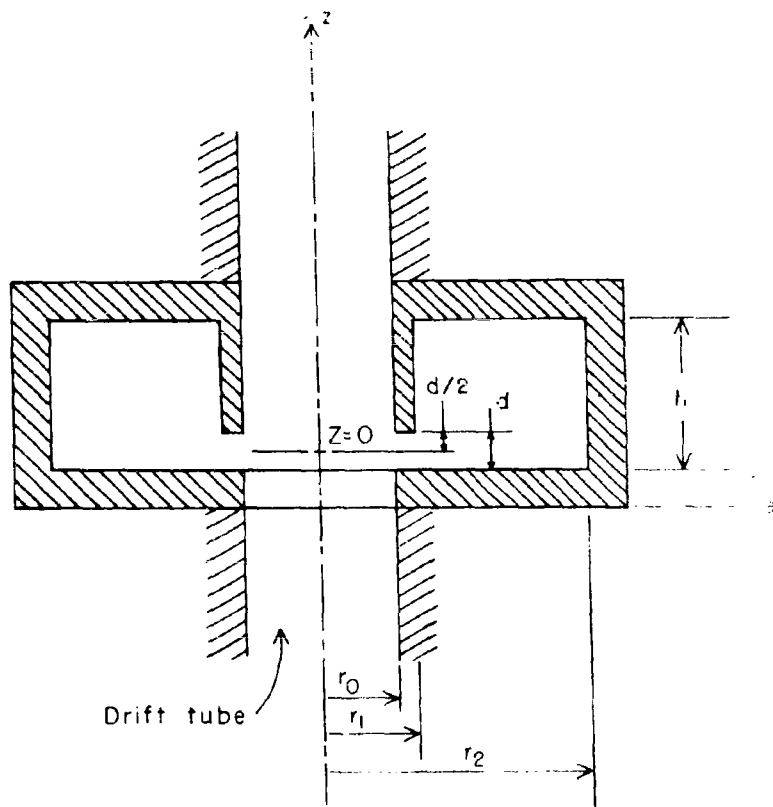


FIGURE 1. Cavity Co-ordinates.

of .750 in. and an inside diameter of .625 in. Transit angle and resonant frequency requirements were then used to find the appropriate values for h and d.

The transit angle is given by

$$\theta_T = \frac{\omega d}{u_0} = \frac{2\pi f d}{u_0} \quad (1)$$

where f is the resonant frequency, and where the beam velocity is

$$u_0 = \left(\frac{2 e V_0}{m} \right)^{\frac{1}{2}} .$$

It was desired to keep θ_T between 1 radian and 2 radians in order to assure a reasonably strong electric field across the gap. This meant that d had to be between 0.0876 in. ($\theta_T = 1$) and 0.1752 in. ($\theta_T = 2$). A second consideration in establishing the gap length was the problem of multipactor, or breakdown, in the gap caused by secondary emission in phase with the gap voltage. A first-order treatment of this problem showed that it would not be a factor at the power levels contemplated for the system. The problem was approached by considering an electron with zero velocity at one side of the gap when a r-f voltage is applied. The force on the electron is given by

$$e \bar{E} = e \frac{V_m}{d} \sin \omega t = m a(t) , \quad (2)$$

and since the acceleration is known, the position can be found by integrating twice and using the initial conditions $u(t=0) = 0$ and $z(t=0) = 0$, which gives

$$u(t) = \int \frac{e V_m}{m d} \sin \omega t \, dt = \frac{e V_m}{\omega m d} [1 - \cos \omega t] , \quad (3)$$

$$z(t) = \int u(t) \, dt = \frac{e V_m}{\omega^2 m d} [\omega t - \sin \omega t] . \quad (4)$$

For multipactor to occur, the electron must arrive at the other side of the gap (that is, $z=d$) when $\omega t = \pi$ (i.e., just as the phase of the r-f voltage reverses) with sufficient energy to cause secondary emission:

$$z(\omega t = \pi) = \frac{e V_m}{\omega^2 m d} \pi \quad (5)$$

To get an idea of the level at which multipactor effects could begin to appear, one can solve Equation (5) for V_m :

$$V_m = \left[\frac{\omega^2 m}{\pi} \frac{m}{2} \right] d^2 \quad (6)$$

Solving Equation (6) for several gap spacings gives the following results:

<u>d (in.)</u>	<u>θ_T (radians)</u>	<u>V_m (volts)</u>
0.0876	1.00	3190
0.100	1.14	4160
0.125	1.43	6500

The maximum value of r-f voltage across the gap is V_m , and the experiments planned for the beam-plasma system should not require values of V_m greater than those listed.

The next step in the design procedure was to consult the design charts in Moreno¹ to determine the values of h and d that would result in a resonant frequency of about 3000 Mc/s. Several possible

pairs of h and d values were chosen and were then checked using the design equations of Fujisawa.² There was about a 10 per cent difference between their predicted resonant frequencies. After the cavities were cold tested, Fujisawa's equations were found to give the best agreement. The sample calculation using the dimensions of the cavities built for cold testing follows:

$$r_2 = 0.875 \text{ in.} = 2.22 \text{ cm} \quad d = 0.125 \text{ in.} = 0.318 \text{ cm}$$

$$r_1 = 0.375 \text{ in.} = 0.952 \text{ cm} \quad h = 0.500 \text{ in.} = 1.280 \text{ cm}$$

$$r_0 = 0.3125 \text{ in.} = 0.795 \text{ cm}$$

$$L = \frac{\mu_0}{2\pi} h \ln \frac{r_2}{r_1} = \text{equivalent inductance} \quad , \quad (7a)$$

$$C_1 = 4\epsilon_0 r_1 \ln \frac{e l_m}{d} = \text{fringing capacitance} \quad , \quad (7b)$$

$$C_0 = \epsilon_0 \frac{\pi(r_1^2 - r_0^2)}{d} + \epsilon_0 \frac{\pi r_0^2}{d} (\gamma) = \text{direct capacitance} \quad , \quad (7c)$$

$$l_m = \frac{\sqrt{(r_2 - r_1)^2 + h^2}}{2} \quad \gamma \cong \frac{1}{3} \text{ (from graph)} \quad (7d)$$

The results of these calculations are:

$$L = 2.145 \times 10^{-9} \quad , \quad C_1 = 6.86 \times 10^{-13} \quad , \quad C_0 = 4.23 \times 10^{-13} \quad ;$$

and the resonant frequency is found to be

$$f_o = \frac{1}{2\pi} \frac{1}{\sqrt{LC}} = \frac{1}{2\pi} \frac{1}{\sqrt{L(C_1 + C_o)}} = 3260 \text{ Mc/s} \quad (8)$$

Two cavities were built for cold testing; resonant frequency, Q , and R_s/Q_o were determined. The test methods are discussed in the following sections since the calculations are important in the later use of this type of cavity for plasma diagnosis. The cold-test results led to a few minor modifications in the design. The cavities to be used in the actual system were then built from the design shown in Figure 2. Figure 3 shows the method of loop coupling and the vacuum seal in the coaxial input line.

III. MEASUREMENT OF CAVITY Q

Cavity Q was measured using the standard point-by-point impedance technique as described in Ginzton.³ When calculating the Q of resonant cavities for use in plasma measurements, the necessary accuracy is not achieved if one neglects the series losses in the coupling circuit between the cavity and transmission line. Since the total loading of the cavity determines the width of the resonance curve, the loaded Q best represents the effective load. For diagnostic work the various Q values are computed so as to include the effects of coupling losses.

A general form of the equivalent circuit representing the cavity and its coupling network is shown in Figure 4. The cavity system consists of a cavity and part of the input transmission line to which the

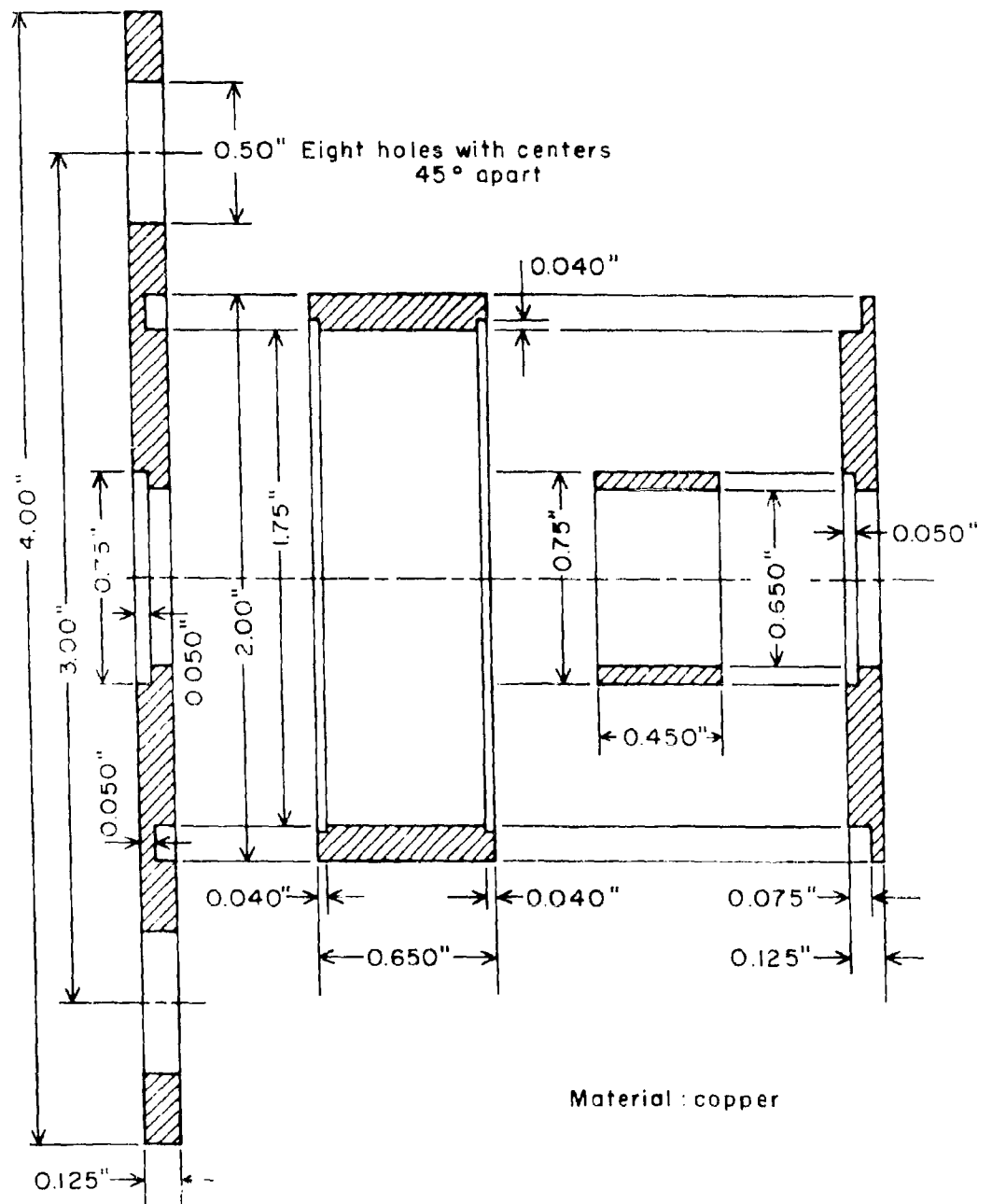


FIGURE 2 Cavity Design.

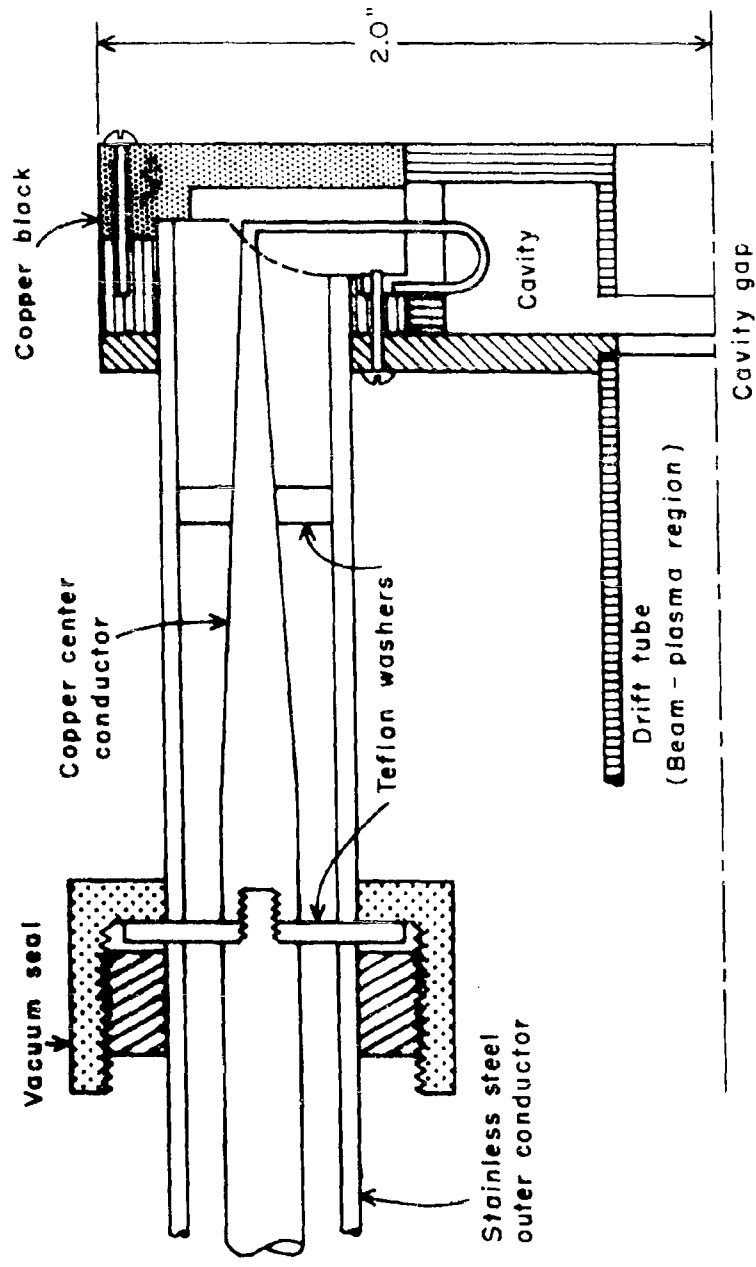


FIGURE 3. R-F Coupling Structure and Vacuum Seal.

cavity is coupled by a loop. To be complete, the equivalent circuit should contain enough elements to account for all phenomena associated with the cavity. Such a circuit is difficult to deal with, so we first construct a reasonably complete equivalent circuit and then attempt to simplify it by making physically reasonable assumptions. The terminals of the coupling network 1-1 and 2-2 are chosen so that all sources of loss are included between them. Also, 1-1 will be located at the detuned-short position (DSP) in order to simplify the treatment of data. Of the several possible forms of equivalent circuits, the one shown in Figure 5 is used, since it is most readily analyzed.

In this network, the resistances R_s and R_p represent the losses; the reactances X_p and X_s represent the reactive elements, such as the inductance of the coupling loop. A simple analysis near resonance is possible only if the energy storage in the loop circuit is negligible compared with that in the cavity at resonance. It is then possible to neglect the reactances X_s and X_p and use the equivalent circuit in Figure 6, which has a new resonant impedance of $\beta_2 Z_0$ after transformation through the transformer.

A plot of the variation of the impedance at terminals 1-1 (plane P_1) with frequency is a circle on the Smith Chart, since it represents the conformal transformation of the circular impedance locus of the network at plane b-b through the coupling network. The locus is shown in Figure 7. If the series resistance in Figure 6 were zero, the impedance locus would pass through the origin ($r = 0$, $x = 0$); thus the choice of P_1 corresponds to the location of the

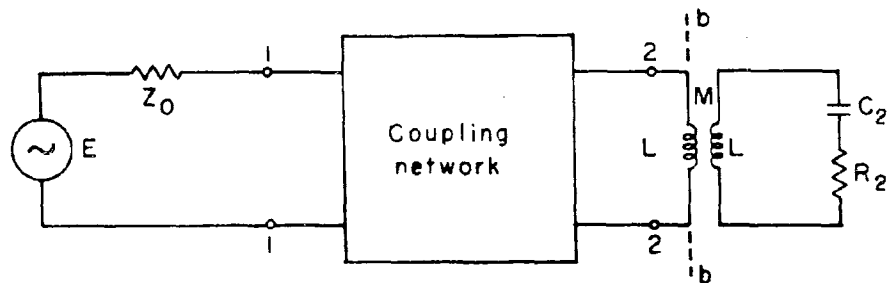


FIGURE 4. General Equivalent Circuit for a Cavity.

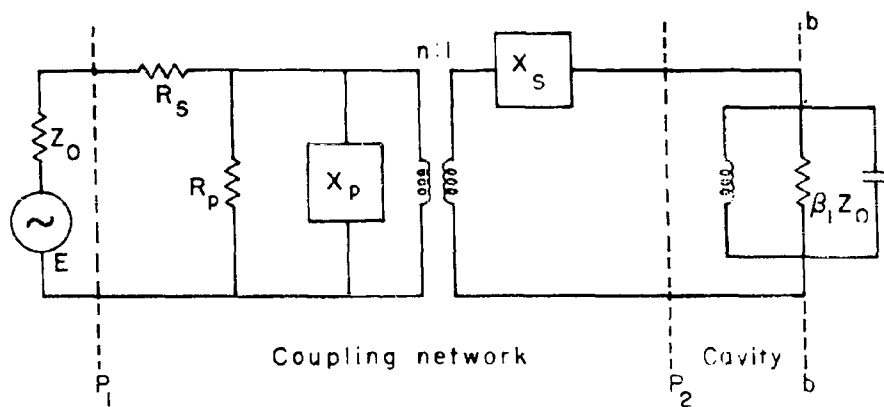


FIGURE 5. Equivalent Circuit.

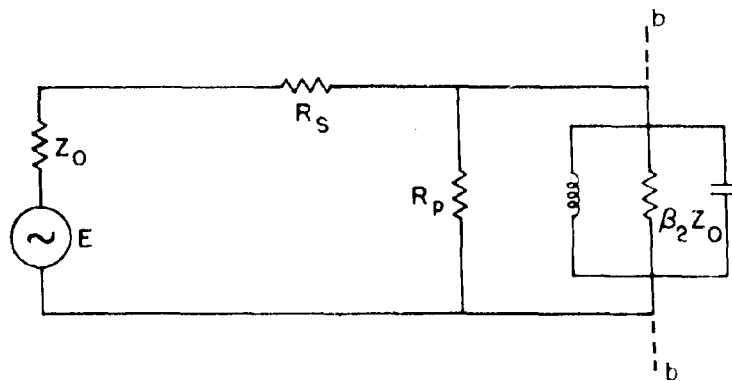


FIGURE 6. Simplified Equivalent Circuit.

detuned-short position in the case of no loss.

Referring to Figure 7, let the intercepts of the impedance locus with the resistive axis be called α and β , which are defined as

$$\alpha = \frac{R_s}{Z_o} \quad , \quad (9)$$

$$\beta = \alpha + \beta' \quad , \quad (10)$$

where

$$\beta' = \frac{R_p \beta_2}{R_p + \beta_2 Z_o} = \beta_2 \frac{\gamma}{\gamma + 1} \quad , \quad (11)$$

$$\gamma = \frac{R_p}{\beta_2} Z_o \quad . \quad (12)$$

The intercept described by α results when the cavity is tuned far off resonance and that described by β when it is tuned to ω_o , where the resonant frequency ω_o is taken as the frequency when the impedance across R_p is a maximum and purely resistive.

The input impedance Z_1 at plane P_1 may be written as

$$Z_1 = R_s + \frac{R_p Z_{bb}}{R_p + Z_{bb}} \quad (13)$$

and

$$\frac{Z_{bb}}{Z_o} = \frac{\beta_2}{1 + j 2 Q_o \delta} \quad , \quad (14)$$

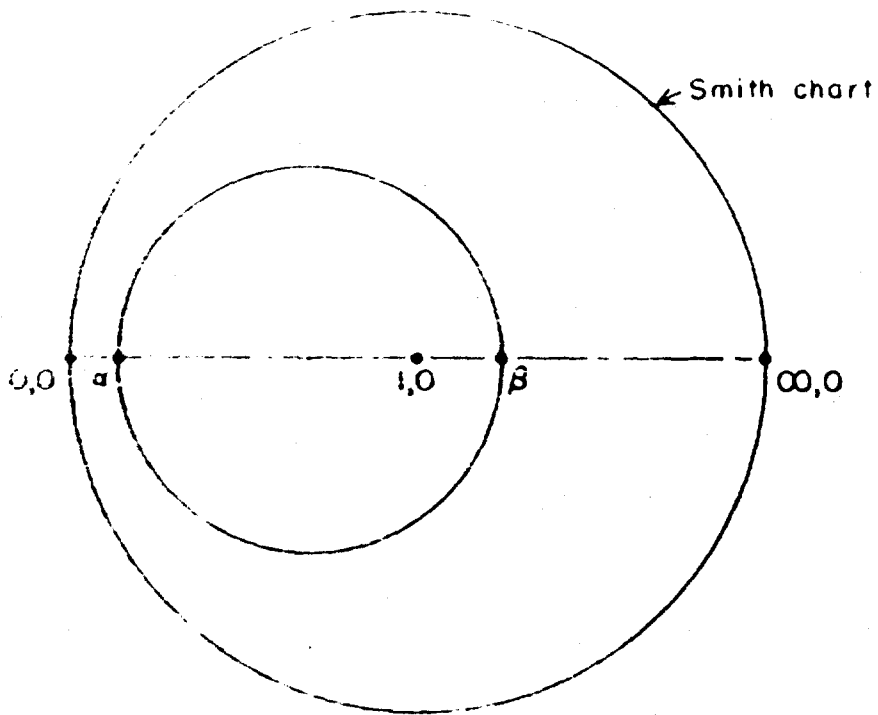


FIGURE 7 Variation of Cavity Impedance with Frequency.

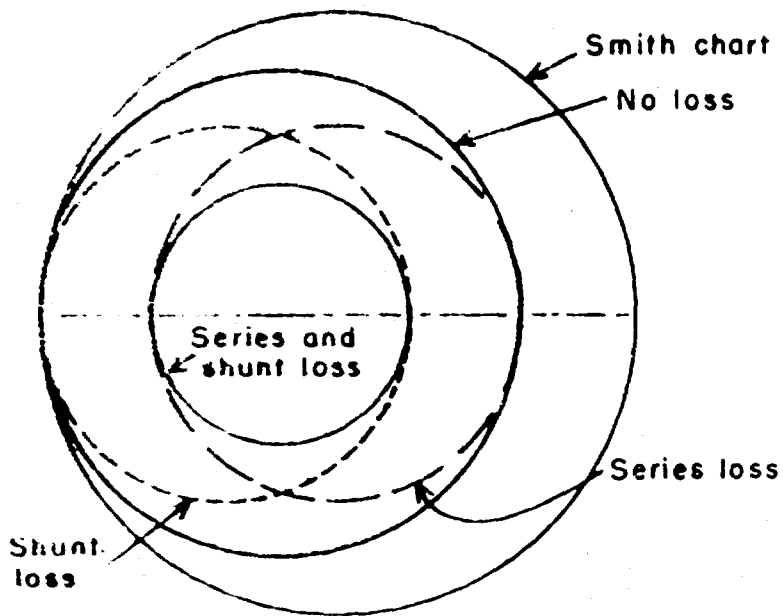


FIGURE 8 Impedance Loci in Presence of Losses

where

Z_0 = characteristic impedance of transmission line,

Q_0 = unloaded Q of cavity, and

$\delta = (\omega - \omega_0)/\omega =$ tuning parameter,

Combining Equations (13) and (14) and rearranging gives

$$\frac{Z_1}{Z_0} = a + \frac{\beta - a}{1 + j 2 Q_0 \delta} \quad (15)$$

where

$$Q_0 = Q_0 \left[\frac{1}{1 + \frac{\beta_2 Z_0}{R_p}} \right] = Q_0 \frac{Y}{Y + 1} \quad (16)$$

Figure 8 shows the impedance locus for the four possible cases: no coupling loss, series loss alone, shunt loss alone, and both series and shunt losses.

It is obvious from the preceding discussion that it is necessary to know the coupling network parameters R_s and R_p to be able to interpret the impedance data. The values of R_s and R_p could be determined experimentally if the coupling network could be physically separated from the cavity. This is impractical or impossible in most cases. Since in most devices coupling losses are small and are due mainly to either series or shunt losses alone, it is convenient to consider three separate cases ⁴

A. CASE 1. SHUNT LOSSES

In this case $\alpha = 0$ and Equation (15) becomes

$$\frac{Z_1}{Z_0} = \frac{\beta}{1 + j 2 Q_0 \delta} \quad (17)$$

where Q_0 may be found from the measured impedance locus; and the true value of Q_0 is obtained from Equation (16) if γ is known.

B. CASE 2. SERIES LOSSES

In this case, $R_p = \infty$, and Equation (15) becomes

$$\frac{Z_1}{Z_0} = \alpha + \frac{\beta - \alpha}{1 + j 2 Q_0 \delta} \quad (18)$$

The value of Q_0 may be obtained from the measured impedance locus in the following way. Let $2Q_0\delta = \pm 1$ and substitute in Equation (18) to get

$$\frac{Z_1}{Z_0} = \frac{\beta + \alpha \pm j(\beta - \alpha)}{2} \quad (19)$$

Using values of α and β taken from a plot of the data, one can compute the real and imaginary parts of Equation (19) and locate them on the locus determining the points for which $2Q_0\delta = \pm 1$. If the frequencies at which they occur are f_1 and f_2 , then

$$Q_0 = \frac{f_0}{f_1 - f_2} \quad (20)$$

If the two points on the locus do not coincide with data points for which the frequencies are known, the desired frequencies may be found by constructing a linear frequency scale as shown in Figure 9.

C. CASE 3. SERIES AND SHUNT LOSSES

When both series and shunt losses are present and each is small, the Q_o' value may be found from Equation (20), which takes into account the series losses alone, and then multiplying this value by the factor given in Equation (16) to account for shunt losses.

When the behavior of resonant cavities is considered, Q_x (the external Q) and Q_L (the loaded Q) are also of interest. These along with Q_o and Q_o' are defined as⁵

$$Q_o = \omega \frac{\text{energy stored in cavity}}{\text{energy dissipated in cavity}} \quad (21)$$

$$Q_o' = \omega \frac{\text{energy stored in cavity}}{\text{cavity losses} + \text{shunt losses}} \quad (22)$$

$$Q_L = \omega \frac{\text{energy stored in cavity}}{\text{cavity losses} + \text{coupling loss} + \text{energy dissipated in load}} \quad (23)$$

$$Q_x = \omega \frac{\text{energy stored in cavity}}{\text{energy dissipated in load}} \quad (24)$$

When coupling losses are not present, or if Z_o , R_s , and R_p are considered to be the load, Q_x , Q_L , and Q_o are related by

$$\frac{1}{Q_L} = \frac{1}{Q_o} + \frac{1}{Q_x} \quad (25)$$

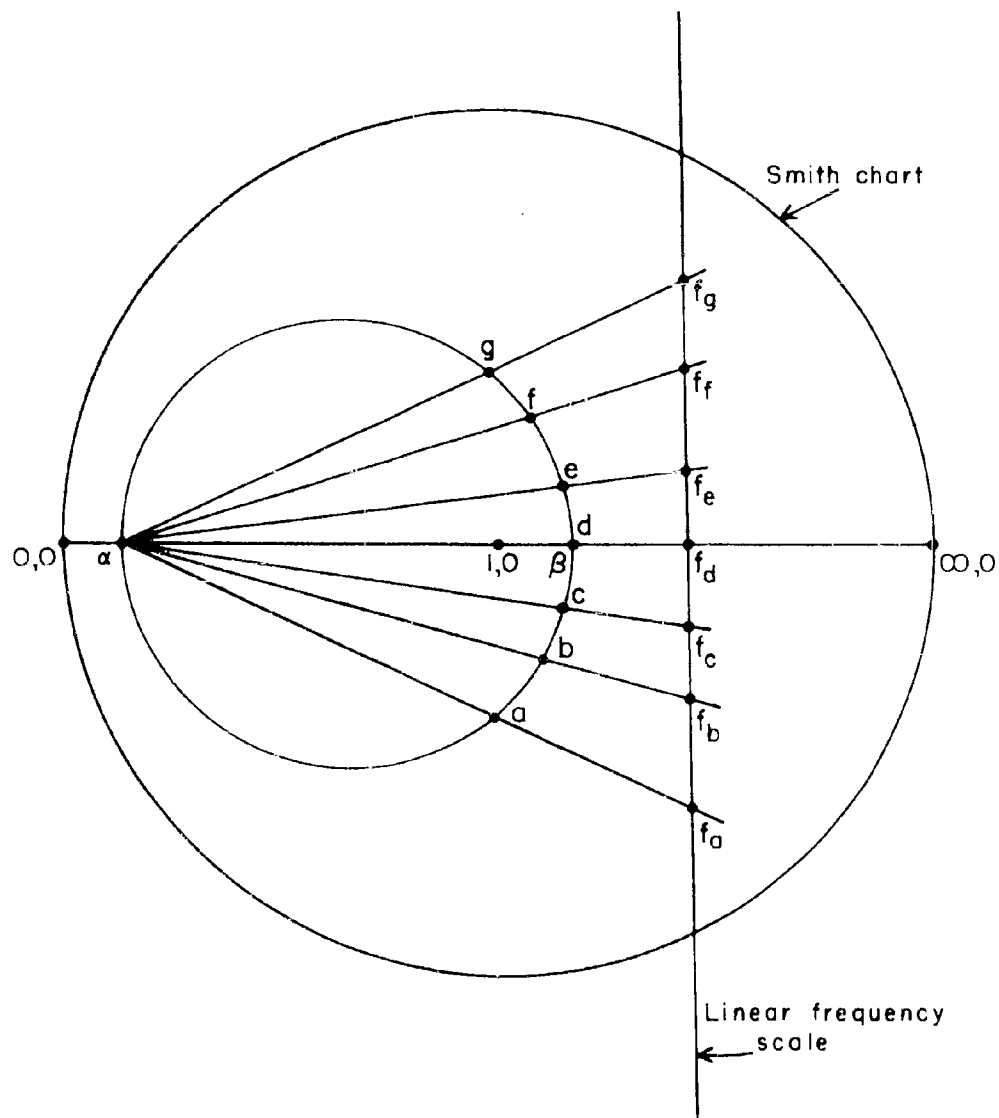


FIGURE 9. Construction of Linear Frequency Scale

When Z_o and R_s are the load, then

$$\frac{1}{Q_L} = \frac{1}{Q_o} + \frac{1}{Q_x} \quad (26)$$

If Q_o' and/or Q_o have been experimentally obtained, and α , β , and γ are known, then the expressions for Q_L and Q_x are found as follows. Let V be the voltage across the capacitance shown in Figure 6, then from Equation (21),

$$Q_o = \omega \frac{\frac{1}{2} CV^2}{\frac{1}{2} \left[\frac{V^2}{\beta_2 Z_o} \right]} = \omega C \beta_2 Z_o \quad (27)$$

Similarly, from Equation (16)

$$Q_o' = Q_o \frac{\gamma}{\gamma+1} = \omega C \beta_2 Z_o \frac{\gamma}{\gamma+1} \quad (28)$$

and

$$Q_L = Q_o' \frac{1+\alpha}{1+\beta} = Q_o \frac{\gamma}{\gamma+1} \frac{1+\alpha}{1+\beta} \quad (29)$$

and from Equation (26),

$$Q_x = Q_o' \frac{1+\alpha}{\beta} \quad (30)$$

Thus if α , β , and γ are all known, it is possible to determine the various Q values. If γ is not known, the Q values may only be found in terms of Q_o' , in which the cavity losses and shunt losses in the coupling network are not separated.

For the particular case of interest, it is convenient and reasonable to assume that the shunt losses are very small and to include them with the cavity losses. Then from Equation (16), Q_0 and Q_0' become identical, and only the effect of series loss is explicitly considered. A method for treating the data is given in Case 2, and an alternate method³ follows. The data required are a plot of VSWR versus frequency near resonance, and the values of a and β . The VSWR at the half-power frequencies, where $2Q_0\delta = \pm 1$, is given by

$$\left(\frac{r_1}{Z}\right)_0 = \frac{|1 + j + (\beta + ja)| + |1 + j - (\beta + ja)|}{|1 + j + (\beta + ja)| - |1 + j - (\beta + ja)|} \quad (31)$$

which may be simplified to

$$\left(\frac{r_1}{Z}\right)_0 = \frac{2 + (\beta^2 + a^2) + \sqrt{4 + (\beta^4 + a^4)} - 8a\beta + 2a^2\beta^2}{2(\beta + a)} \quad (32)$$

The frequencies f_1 and f_2 may be found from the plot of VSWR versus frequency, and Equation (20) can be used to find Q_0 .

IV. MEASUREMENT OF $\mu^2 R_{sh}/Q_0$

A prediction of the performance of cavities as resonant systems is made possible by the measurement of R_{sh} , the shunt resistance, and Q_0 of the resonator, or by the measurement of $\mu^2 R_{sh}/Q_0$ in

the case where an electron beam is present. These three parameters are considered because cavity resonators are subject to three types of loading: resistive losses, external loads, and beam loading. For maximum output, when the cavity is used to couple energy from an electron beam to a load, it is customary to design the resonator so that the effective shunt resistance $\mu^2 R_{sh}$ is equal to the beam-loading impedance; which may be approximated by the d-c beam impedance. This specifies $\mu^2 R_{sh}$ and, since R_{sh}/Q_0 is independent of loading, determines the degree of coupling necessary for proper matching. Appropriate matching will be necessary to obtain reasonable output power from the beam-plasma system, therefore knowledge of $\mu^2 R_{sh}/Q_0$ for the cavities used is useful.

The effective gain-bandwidth parameter $\mu^2 R_{sh}/Q_0$ for a cylindrical electron beam of radius b traversing an interaction gap of length d in a resonator having cylindrical symmetry can be measured by a perturbation technique.⁵ The resonant frequency shift caused by a small metallic sphere located successively at closely spaced points on the axis of the interaction gap is measured, and the resulting distribution of frequency shifts is used to determine both the configuration of the electric field on the axis of the resonator and the value of $\mu^2 R_{sh}/Q_0$ that corresponds to the electron beam to be used in the resonator.

The equation relating $\mu^2 R_{sh}/Q_0$ to the frequency shifts caused by a metallic bead of radius r_0 is

$$\mu^2 \frac{R_{sh}}{Q_0} = 120 \times 10^8 \frac{f_0^2 (10) - f_1^2 (10)}{f_0^2} \int_{-\infty}^{\infty} \frac{\sqrt{\Delta f} e^{j\beta_e z} dz}{\Delta V} \quad (33)$$

where

Δf = resonant frequency shift as a function of bead position on the resonator axis;

z = axial position of beam with respect to the midplane of the resonator gap;

$\beta_e = 2\pi f_0 / \mu_0 =$ axial propagation constant of electrons, where μ_0 is the d-c beam velocity and f_0 is the resonant frequency;

b = radius of electron beam;

$\Delta V = \frac{4}{3} \pi r_0^3$; and

$$Y = \sqrt{\beta_e^2 - (2\pi f_0 / c)^2}$$

It should be noted that the computation of $\mu^2 R_{sh} / Q_0$ is based on field distributions actually measured in the resonator, and no assumptions are made about field distributions in an ideal cavity, as is often done. The derivation of Equation (33) is made under two assumptions: the interaction gap has cylindrical symmetry, and the beam radius is small compared to the gap radius.

We can define Q_0 by

$$Q_0 = \omega \frac{\text{energy stored}}{\text{energy dissipated}} = \frac{\omega U}{W} \quad (34)$$

where U is the stored energy, and W is the energy dissipated per second in the cavity. The effective shunt resistance is defined in terms of the square of the effective gap voltage as

$$\mu^2 R_{sh} = R_{eff} = \frac{(\text{effective voltage})^2}{\text{power loss}} \quad (35)$$

$$\mu^2 R_{sh} = \frac{(\mu_b \mu_d E_m d)^2}{2W} \quad (36)$$

where μ_b and μ_d are as defined by Branch.⁶ Combining Equations (34) and (36) gives

$$\mu^2 R_{sh}/Q_0 = \frac{(\mu_b \mu_d E_m d)^2}{2\omega U} \quad (37)$$

From Slater's perturbation formula⁷ for a metallic sphere,

$$\frac{f - f_0}{f_0} = \frac{3 \int (\mu H^2 - \epsilon E^2) dV}{4U} \quad (38)$$

and for the re-entrant cavities of interest, $H = 0$ on the axis. Since the bead is small, Equation (38) then becomes

$$\frac{\Delta f}{f_0} = - \frac{3 \epsilon E^2 \Delta V}{4U} \quad (39)$$

Solving Equation (39) for U and substituting in Equation (37) gives

$$\mu^2 \frac{R_{sh}}{Q_o} = \frac{(\mu_b \mu_d E_m d)^2 \Delta f}{3 \pi \epsilon f_o^2 E^2 \Delta V} \quad (40)$$

Considering $\mu^2 R_{sh}/Q_o$ in terms of the maximum frequency shift that corresponds to E_m gives

$$\mu^2 \frac{R_{sh}}{Q_o} = 120 \times 10^8 \mu^2 \frac{d^2 \Delta f_{max}}{f_o^2 \Delta V} \quad (41)$$

where $\mu = \mu_b \mu_d$. Branch gives μ as

$$\mu = \mu_b \mu_d = \frac{\int_{-\infty}^{\infty} g(z) e^{j\beta_e z} dz}{d} \cdot \frac{I_o^2(\gamma_b) - I_1^2(\gamma_b)}{I_o(\gamma_a)} \quad (42)$$

On the axis, $a = 0$, and $I_o(0) = 1$.

$$\mu^2 = \frac{\int_{-\infty}^{\infty} g(z) e^{j\beta_e z} dz}{d^2} \left[I_o^2(\gamma_b) - I_1^2(\gamma_b) \right] \quad (43)$$

and, therefore,

$$\mu^2 \frac{R_{sh}}{Q_o} = 120 \times 10^8 \frac{I_o^2(\gamma_b) - I_1^2(\gamma_b)}{f_o^2} \frac{\Delta f_{max}}{\Delta V} \left[\int_{-\infty}^{\infty} g(z) e^{j\beta_e z} dz \right]^2 \quad (44)$$

where $g(z)$ is the normalized variation of the field in the gap referred to the field on the axis. Thus for an arbitrary field variation

$$g(z) = \frac{E_z}{E_m} \quad (45)$$

From Slater's perturbation formula, the change in frequency at any point on the z -axis is proportional to the square of the electric field; thus

$$E_z = K\sqrt{\Delta f} \quad , \quad E_m = K\sqrt{\Delta f_{\max}} \quad , \quad g(z) = \frac{\sqrt{\Delta f}}{\sqrt{\Delta f_{\max}}} \quad (46)$$

Substituting gives Equation (33):

$$\mu^2 \frac{R_{sh}}{Q_o} = 120 \times 10^8 \frac{I_o^2(\gamma b) - I_1^2(\gamma b)}{f_o^2} \frac{\left| \int_{-\infty}^{\infty} \sqrt{\Delta f} e^{j\beta e^z} dz \right|^2}{\Delta V} \quad (47)$$

The integral can be evaluated graphically or by Simpson's rule.

A diagram of a test setup suitable for performing the required measurements is shown in Figure 10. The resonance curve is displayed on the oscilloscope; then the marker signal, an accurately known harmonic, is centered, and the frequency is read on the electronic counter. The bead is then lowered, the marker signal is readjusted to center, and the corresponding frequency shift is read from the counter. The process is repeated in convenient steps.

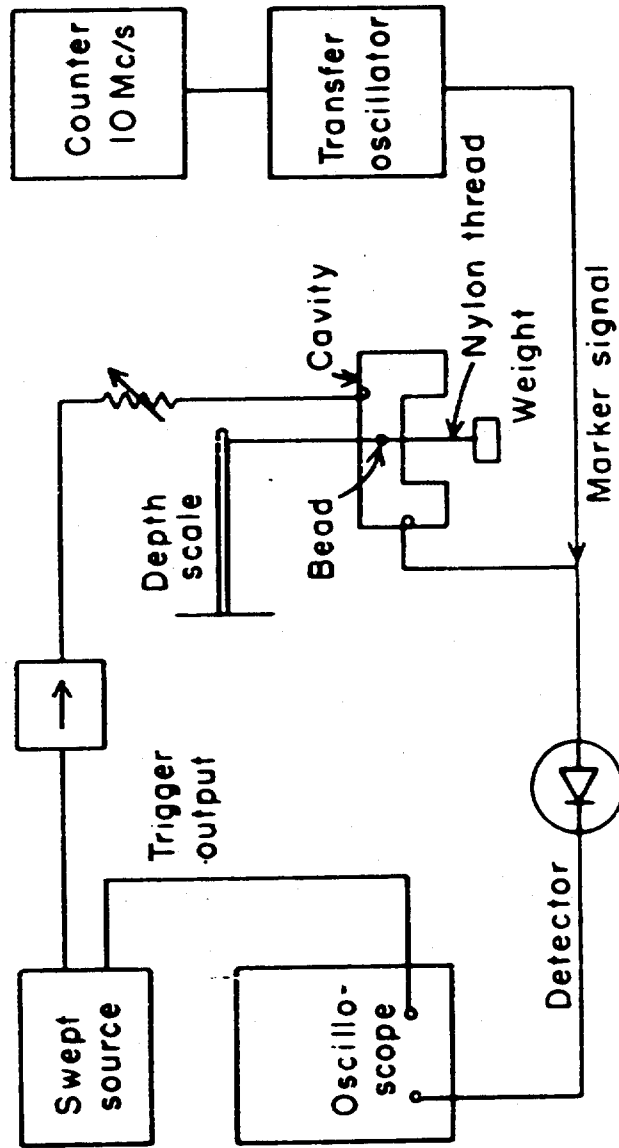


FIGURE 10. Test Setup for Perturbation Measurements.

The equations and techniques developed in this section may be used to find R_{sh}/Q_0 for the cavity alone, as well as $\mu^2 R_{sh}/Q_0$ when an electron beam must be considered.

V. COLD TEST RESULTS

The first measurements were made on a test cavity built for cold testing and the results are compared with theoretical values. Q_0 was measured using a coaxial slotted line and a standing-wave indicator, the initial value, obtained by following the procedure discussed in Section III, being $Q_0 = 4920$. Lower values were obtained from later measurements because of the deterioration of the copper surfaces. R_{sh}/Q_0 was found by using the perturbation technique described in Section IV. Dividing both sides of Equation (41) by μ^2 gives

$$\frac{R_{sh}}{Q_0} = 120 \times 10^8 \frac{d^2}{f_0^2} \frac{\Delta f_{max}}{\Delta V} \quad (48)$$

A metallic bead was pulled through the gap and the maximum frequency shift recorded. The following values,

$$\begin{aligned} d &= 0.125 \text{ in.} = 0.318 \text{ cm} & \Delta V &= 4\pi r_0^3/3 \\ f_0 &= 3280.97 \text{ Mc/s} & r_0 &= 0.031 \text{ in.} = 0.0787 \text{ cm} \\ \Delta f_{max} &= 94 \text{ kc/s} \end{aligned}$$

inserted in Equation (48) gave a value of 51 for R_{sh}/Q_o . For comparison, theoretical values follow, together with the values for Q_o and R_{sh}/Q_o obtained from Ginzton and Nalos.⁸

	f_o (Mc/s)	Q_o	R_{sh}/Q_o
Theoretical Value:	3260	5250	45
Experimental Value:	3280.97	4920	51

The close agreement between the theoretical and experimental values is an indication that the design procedures were sound.

Figure 11 shows the normalized axial electric field in the gap as determined by the perturbation method. The curve is not symmetrical because the gap configuration of the singly re-entrant cavity is asymmetrical.

VI. FREQUENCY SHIFT OF CAVITY MODES IN PRESENCE OF A PLASMA

In this section, an expression for the frequency shift of a nondegenerate mode of a cavity perturbed by a plasma is derived. The properties of the plasma are represented by a tensor dielectric constant or by a tensor conductivity derived from the following tensor mobility:⁹

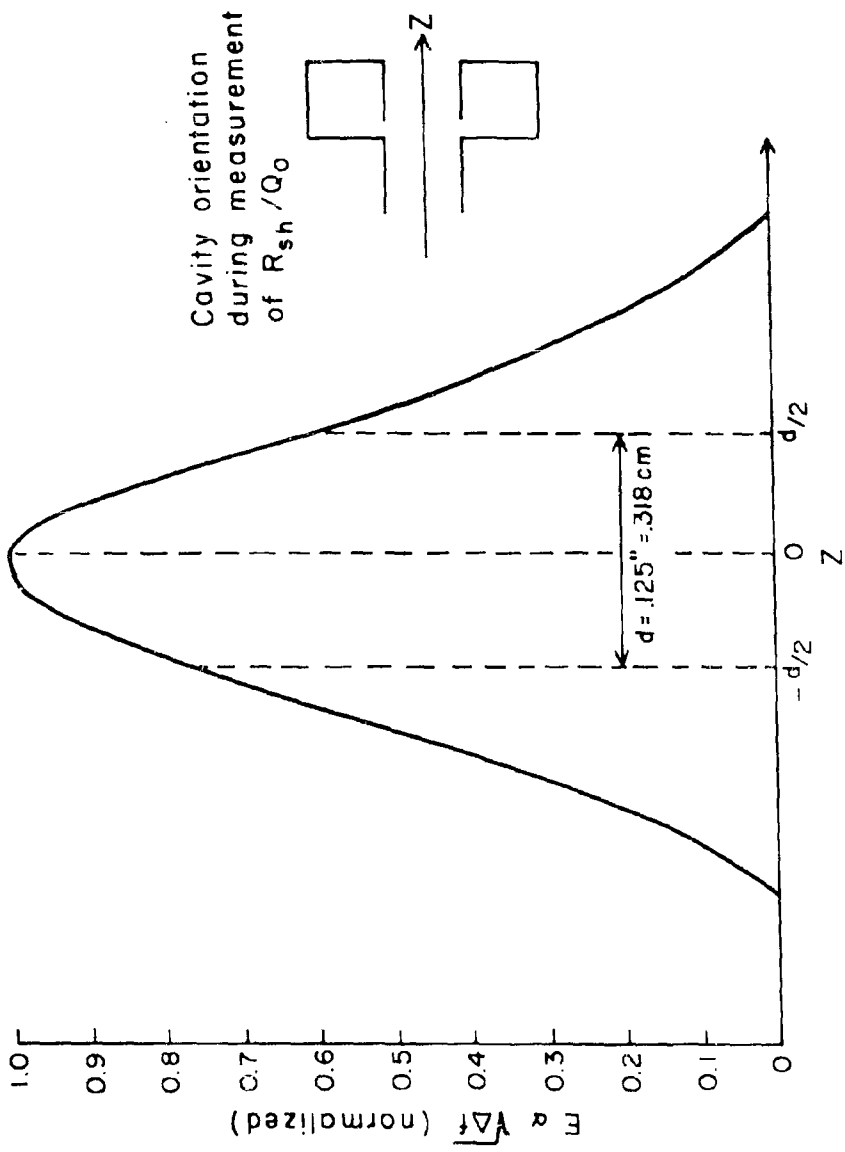


FIGURE 11. Relative Electric Field on the Axis of Cavity. $f_0 = 3280.97$, $\Delta f_{\text{max}} = 94\text{kc}/e$.

$$\mu = \frac{e}{2m} \begin{bmatrix} 1+r & -j(1-r) & 0 \\ j(1-r) & 1+r & 0 \\ 0 & 0 & 2p \end{bmatrix}, \quad (49)$$

where

$$l = -\frac{4\pi}{3} \int_0^{\infty} \frac{v^3 \frac{\partial f^{\circ}}{\partial v} dv}{v_c + j(\omega - \omega_b)},$$

$$r = -\frac{4\pi}{3} \int_0^{\infty} \frac{v^3 \frac{\partial f^{\circ}}{\partial v} dv}{v_c + j(\omega - \omega_b)}, \quad (50)$$

$$p = -\frac{4\pi}{3} \int_0^{\infty} \frac{v^3 \frac{\partial f^{\circ}}{\partial v} dv}{v_c + j\omega},$$

and $\omega_b = e B_0/m$ is the electron cyclotron frequency; B_0 is the d.c. magnetic field parallel to the z-axis, and f° is the normalized, spherically symmetric part of the electron velocity-distribution function. When f° is Maxwellian and v_c is independent of velocity, the integrals for l , r , and p can be evaluated to yield

$$l = \frac{1}{v_c + j(\omega + \omega_b)},$$

$$r = \frac{1}{v_c + j(\omega - \omega_b)}, \quad (60)$$

$$p = \frac{1}{v_c + j\omega}.$$

The mobility and conductivity are related by

$$\underline{\underline{\sigma}} = ne \underline{\underline{\mu}} = \frac{ne^2}{2m} \begin{bmatrix} 1+r & -j(1-r) & 0 \\ j(1-r) & 1+r & 0 \\ 0 & 0 & 2p \end{bmatrix} \quad (61)$$

$$= \begin{bmatrix} \sigma_{rr} & \sigma_{r\theta} & 0 \\ \sigma_{\theta r} & \sigma_{\theta\theta} & 0 \\ 0 & 0 & \sigma_{zz} \end{bmatrix} ,$$

where n is the electron density. A tensor dielectric constant is defined by

$$\underline{\underline{K}} = \underline{\underline{I}} + \underline{\underline{\sigma}}/j\omega\epsilon_0 = \begin{bmatrix} K_{rr} & K_{r\theta} & 0 \\ K_{\theta r} & K_{\theta\theta} & 0 \\ 0 & 0 & K_{zz} \end{bmatrix} , \quad (62)$$

where $\underline{\underline{I}}$ is the unit tensor,

$$K_{\theta\theta} = K_{rr} = 1 - \frac{\omega_p^2}{\omega^2} \frac{(1-j\gamma)}{(1-j\gamma)^2 - \omega_b^2/\omega^2} , \quad (63a)$$

$$K_{r\theta} = -K_{\theta r} = j \frac{\omega_p^2/\omega^2 - \omega_b/\omega}{(1-j\gamma)^2 - \omega_b^2/\omega^2} , \quad (63b)$$

$$K_{zz} = 1 - \frac{\omega_p^2}{\omega^2} \frac{1}{(1 - j\gamma)} \quad , \quad (63c)$$

and $\omega_p^2 = ne^2/m\epsilon_0$, and $\gamma = \nu_c/\omega$. Because the motion of ions has been neglected, the validity of this treatment is limited to plasmas of electron temperatures low enough that Landau damping and other effects characteristic of a hot plasma are negligible.¹⁰

We now consider two solutions to Maxwell's equation for a cavity: \bar{E}_0 , \bar{H}_0 in the absence of the plasma, and \bar{E}_1 , \bar{H}_1 when the plasma is present. The first set satisfies

$$\nabla \times \bar{E}_0 = -j\omega_0 \mu_0 \bar{H}_0 \quad , \quad (64)$$

$$\nabla \times \bar{H}_0 = j\omega_0 \epsilon_0 (\underline{K}_0 \cdot \bar{E}_0) \quad , \quad (65)$$

where \underline{K}_0 is the unit tensor if the cavity is empty. When the plasma is present, \bar{E}_1 , \bar{H}_1 satisfy

$$\nabla \times \bar{E}_1 = -j\omega \mu_0 \bar{H}_1 \quad , \quad (66)$$

$$\nabla \times \bar{H}_1 = j\omega \epsilon_0 (\underline{K} \cdot \bar{E}_1) \quad . \quad (67)$$

Now multiply Equation (65) by \bar{E}_1 and Equation (67) by \bar{E}_0 , and integrate over the cavity volume to obtain

$$\int \bar{E}_1 \cdot \nabla \times \bar{H}_0 \, dv = j \int \omega_0 \epsilon_0 \bar{E}_1 \cdot (\underline{K}_0 \cdot \bar{E}_0) \, dv \quad , \quad (68)$$

$$\int \bar{E}_0 \cdot \nabla \times \bar{H}_1 \, dv = j \int \omega \epsilon_0 \bar{E}_0 \cdot (\underline{K} \cdot \bar{E}_1) \, dv \quad . \quad (69)$$

Then subtract Equation (69) from Equation (68), which gives

$$\int [\bar{\mathbf{E}}_1 \cdot \nabla \times \bar{\mathbf{H}}_0 - \bar{\mathbf{E}}_0 \cdot \nabla \times \bar{\mathbf{H}}_1] dv = j \int \epsilon_0 [\omega_0 \bar{\mathbf{E}}_1 \cdot (\underline{\mathbf{K}}_0 \cdot \bar{\mathbf{E}}_0) - \omega \bar{\mathbf{E}}_0 \cdot (\underline{\mathbf{K}} \cdot \bar{\mathbf{E}}_1)] dv \quad (70)$$

The left side of Equation (70) becomes

$$\begin{aligned} [\bar{\mathbf{E}}_1 \cdot \nabla \times \bar{\mathbf{H}}_0 - \bar{\mathbf{E}}_0 \cdot \nabla \times \bar{\mathbf{H}}_1] dv &= \int \nabla \cdot [\bar{\mathbf{H}}_0 \times \bar{\mathbf{E}}_1 - \bar{\mathbf{H}}_1 \times \bar{\mathbf{E}}_0] dv \\ &+ \int [\bar{\mathbf{H}}_0 \cdot \nabla \times \bar{\mathbf{E}}_1 - \bar{\mathbf{H}}_1 \cdot \nabla \times \bar{\mathbf{E}}_0] dv \quad (71) \end{aligned}$$

and by the divergence theorem, the first term on the right of Equation (71) can be rewritten as the surface integral over the cavity walls of

$$\hat{\mathbf{n}} \cdot [\bar{\mathbf{H}}_0 \times \bar{\mathbf{E}}_1 - \bar{\mathbf{H}}_1 \times \bar{\mathbf{E}}_0] \quad ,$$

which is zero if the walls are perfect conductors. The second integral in Equation 71 can be simplified by using Equation (64) and Equation (66) to define $\nabla \times \bar{\mathbf{E}}_0$ and $\nabla \times \bar{\mathbf{E}}_1$:

$$\int [\bar{\mathbf{H}}_0 \cdot \nabla \times \bar{\mathbf{E}}_1 - \bar{\mathbf{H}}_1 \cdot \nabla \times \bar{\mathbf{E}}_0] dv = j \mu_0 (\omega_0 - \omega) \int \bar{\mathbf{H}}_1 \cdot \bar{\mathbf{H}}_0 dv \quad (72)$$

Equation (70) can now be rewritten as

$$\mu_0 (\omega_0 - \omega) \int \bar{\mathbf{H}}_1 \cdot \bar{\mathbf{H}}_0 dv = \epsilon_0 \int [\omega_0 \bar{\mathbf{E}}_1 \cdot (\underline{\mathbf{K}}_0 \cdot \bar{\mathbf{E}}_0) - \omega \bar{\mathbf{E}}_0 \cdot (\underline{\mathbf{K}} \cdot \bar{\mathbf{E}}_1)] dv \quad (73)$$

which can be solved for the relative frequency shift $\delta = (\omega - \omega_0)/\omega$ as

$$\delta = - \frac{\epsilon_0 \int [\bar{\mathbf{E}}_0 \cdot (\underline{\mathbf{K}} \cdot \bar{\mathbf{E}}_1) - \bar{\mathbf{E}}_1 \cdot (\underline{\mathbf{K}}_0 \cdot \bar{\mathbf{E}}_0)] dv}{\epsilon_0 \int \bar{\mathbf{E}}_1 \cdot (\underline{\mathbf{K}}_0 \cdot \bar{\mathbf{E}}_0) dv - \mu_0 \int \bar{\mathbf{H}}_1 \cdot \bar{\mathbf{H}}_0 dv} \quad (74)$$

This can also be written as

$$\delta = \frac{j}{\omega} \frac{\int \bar{\mathbf{E}}_0 \cdot [(\underline{\mathbf{g}} - \underline{\mathbf{g}}_0) \cdot \bar{\mathbf{E}}_1] dv}{\epsilon_0 \int \bar{\mathbf{E}}_0 \cdot \bar{\mathbf{E}}_1 dv - \mu_0 \int \bar{\mathbf{H}}_0 \cdot \bar{\mathbf{H}}_1 dv} \quad (75)$$

For the case where the unperturbed cavity is in a vacuum, Equation (75) can be further simplified to give

$$\delta = \frac{j}{2\omega\epsilon_0} \frac{\int \bar{\mathbf{E}}_0 \cdot \underline{\mathbf{g}} \cdot \bar{\mathbf{E}}_1 dv}{\int \bar{\mathbf{E}}_0 \cdot \bar{\mathbf{E}}_1 dv} \quad (76)$$

This equation is the basis of the plasma diagnosis, since it relates the complex frequency shifts to the cavity fields and plasma parameters.

VII. PLASMA DIAGNOSIS

In the microwave-cavity method of measuring properties of a plasma (in use for over fifteen years^{11, 12}), the plasma to be studied is partially or completely contained in a microwave cavity, and the resulting

shift in the resonant frequency and the change in cavity Q_0 are measured. These two measurements are then related to the electron density and electron collision frequency by means of the expressions derived in the preceding section.

The structure of the singly re-entrant cavity makes it possible to assume that only z-directed electric fields interact strongly with the plasma. This means that Equation (76) may be simplified to

$$\delta = \frac{j}{2\omega\epsilon_0} \frac{\int \sigma_{zz} \bar{E}_0 \cdot \bar{E}_1 dv}{\int \bar{E}_0 \cdot \bar{E}_1 dv} \quad (77)$$

where σ_{zz} is given by

$$\sigma_{zz} = \frac{ne^2}{m} \frac{1}{v_c + j\omega} = \frac{nc^2}{\omega m} \frac{\gamma - j}{1 + \gamma^2} \quad (78)$$

Since σ_{zz} is a complex quantity, δ is also complex, with its real part equal to the relative shift in resonant frequency, and with twice the imaginary part equal to $\frac{1}{Q} - \frac{1}{Q_0}$. The following equations express these relationships:

$$\frac{f - f_0}{f} = \frac{1}{2} \int \frac{x}{1 + \gamma^2} \bar{E}_0 \cdot \bar{E}_1 dv / \int \bar{E}_0 \cdot \bar{E}_1 dv \quad (79)$$

$$\frac{1}{Q} - \frac{1}{Q_0} = \int \frac{-\gamma x}{1 + \gamma^2} \bar{E}_0 \cdot \bar{E}_0 dv / \int \bar{E}_0 \cdot \bar{E}_1 dv \quad (80)$$

where $x = ne^2/m\epsilon_0\omega^2 = \omega_p^2/\omega^2$ and $\gamma = v_c/\omega$.

The only problem remaining is that of performing the required integrations in Equations (79) and (80). Buchsbaum and Brown¹³ have solved this problem by assuming that the plasma causes only a small perturbation of the cavity fields and the electron density is constant within the volume of integration. These assumptions allow one to replace \bar{E}_1 with \bar{E}_0 to obtain

$$\frac{\Delta f}{f} = \frac{1}{Z} \int \frac{x}{1+\gamma} E_0^2 dv \bigg/ \int E_0^2 dv = \frac{1}{Z} \frac{x}{1+\gamma} \quad (81)$$

$$\frac{1}{Q} - \frac{1}{Q_0} = \int \frac{\gamma x}{1+\gamma} E_0^2 dv \bigg/ \int E_0^2 dv = \frac{\gamma x}{1+\gamma} \quad (82)$$

When the electron density is low, that is, when $x = \omega_p^2/\omega^2 \ll 1$, the approximation is good, since the plasma does not appreciably disturb the electric field. As the density is increased however, \bar{E}_1 becomes different from \bar{E}_0 for three reasons: (1) a-c space charge, commonly called "plasma resonance," appears as ω_p^2/ω^2 approaches unity; (2) as ω_p^2/ω^2 becomes greater than unity, the plasma begins to shield its interior from the field outside; and (3) when both ω_p^2/ω^2 and the pressure are high enough that the Q value changes greatly, the overlapping of higher modes may also cause \bar{E}_1 to be different from \bar{E}_0 by adding to \bar{E}_0 some of the fields of the higher modes. This means that the cavity method will work well at low pressures and small percentages

of ionization, but will give increasingly poorer results as pressure and ionization increase. When the perturbation theory is valid, the electron density and the resonant frequency shift have an approximately linear relationship. The point at which the measured data begins to depart from this linear relationship indicates the beginning of the region where Equations (81) and (82) are no longer valid. Experimentally, this point is obtained by making a plot of resonant frequency shift versus discharge current.

In the region where the perturbation analysis is not valid, one must return to Equations (79) and (80) and employ the actual cavity fields E_0 and E_1 if an exact analysis is to be made. This is a questionable procedure because the approximations that have to be made in order to obtain a reasonable solution for the fields are difficult to work with. For convenience in experimental work, it may be preferable to extrapolate the data taken in the region where the perturbation relations are valid and then use the point where $\omega = \omega_p$ for calibration. The validity of this method can only be determined by experiment.

Since the electron density is not a constant in the actual system, but varies radially, the values for n found by experiment will be average values. These are not a disadvantage in this study since we are concerned with the bulk plasma properties.

VIII. EXPERIMENTAL RESULTS

Preliminary data has been obtained on the hydrogen plasma discharge described in this report. Figures 12 and 13 show, respectively, the d-c current-voltage characteristics and the detuning of the microwave cavity as a function of discharge current.

The linear relationship between the cavity detuning and the discharge current indicates that the approximations in the perturbation analysis are justified for the range of discharge currents studied. Further measurements are being made to find the absolute electron density.

It was possible to reset the plasma current so that the cavity detuning was within one or two megacycles of the earlier data. These results indicate that cavity detuning is a practical way of adjusting the plasma density to the desired point for beam plasma amplifications.

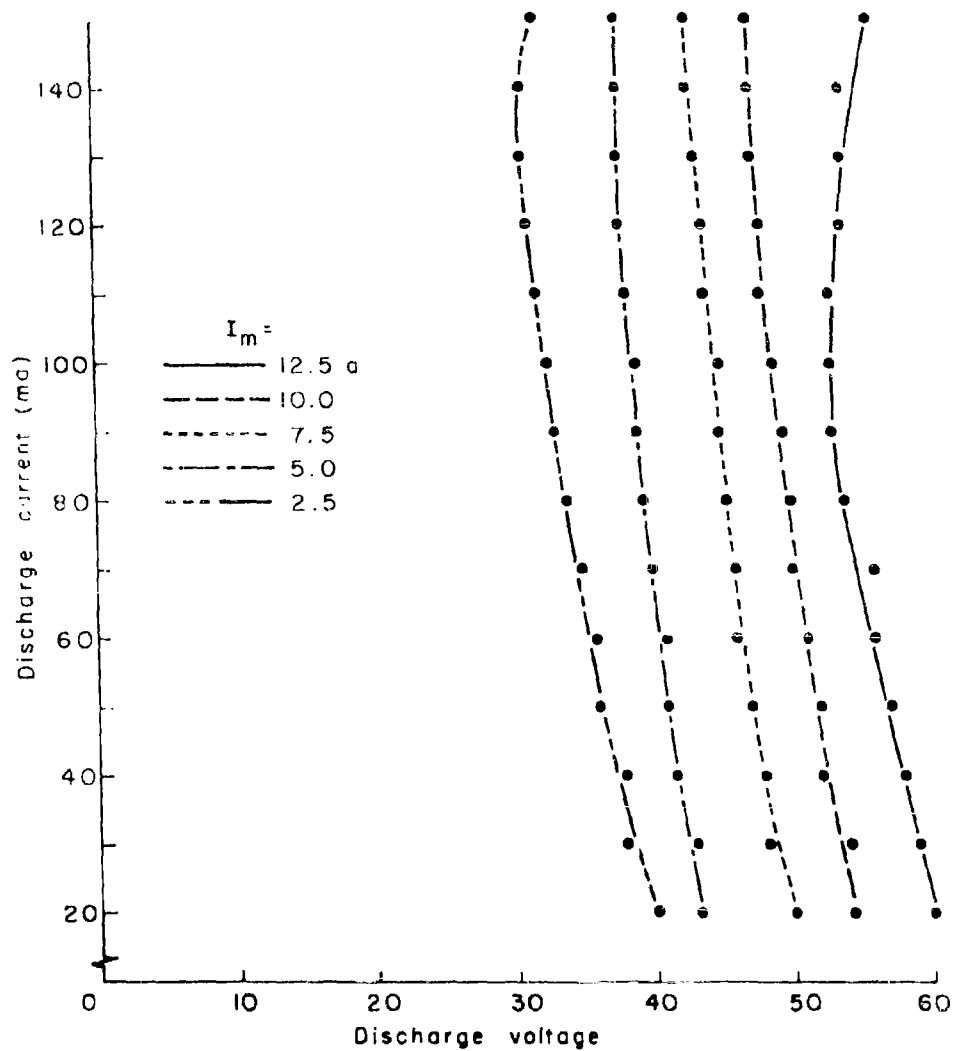


FIGURE 12. Current-Voltage Characteristics of Plasma Discharge at Different Values of d-c Solenoid Current (I_m)

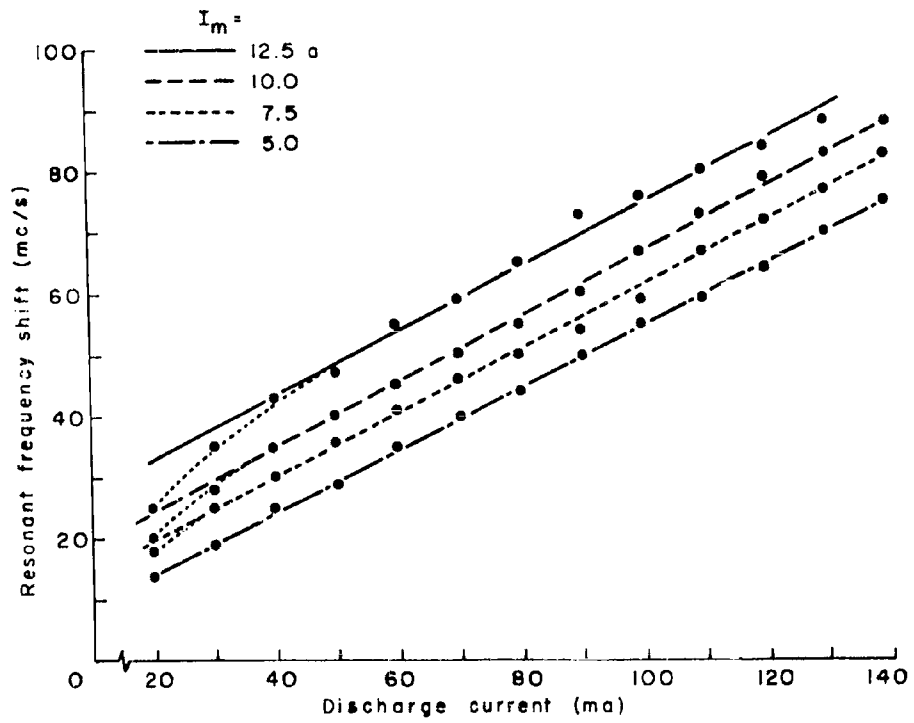


FIGURE 13. Frequency Shift of Resonant Cavity versus Discharge Current at Fixed (I_m)

IX. REFERENCES

1. T. Moreno, Microwave Transmission Design Data, New York: Dover (1958).
2. K. Fujisawa, "General Treatment of Klystron Resonant Cavities," Trans. I.R.E. MTT-6 (October 1958), pp. 344-358.
3. E. L. Ginzton, Microwave Measurements, New York: McGraw-Hill (1957).
4. E. L. Ginzton, "Microwave Q Measurements in the Presence of Coupling Losses," Trans. I.R.E. , MTT-6 (October 1958), pp. 383-389.
5. G. M. Branch, Private communication.
6. G. M. Branch, "Electron Beam Coupling in Interaction Gaps of Cylindrical Symmetry," Trans. I.R.E. , ED-8 (May 1961), pp. 193-207.
7. J. C. Slater, Microwave Electronics, Princeton, N. J.: D. Van Nostrand (1950).
8. E. L. Ginzton and E. J. Nalos, "Shunt Impedance of Klystron Cavities," Trans. I.R.E. MTT-3 (October 1955), pp. 4-7.
9. W. P. Allis, "Motions of Ions and Electrons," Tech. Rep. No. 299, Research Laboratory of Electronics, M.I.T. (1956).
10. S. J. Buchsbaum, L. Mower, and S. C. Brown, "Interaction between Cold Plasmas and Guided Electromagnetic Waves," Phys. Fluids, 3 (1960), p. 806.

11. S. C. Brown, et al., "Methods of Measuring the Properties of Ionized Gases at Microwave Frequencies," Tech. Rep. No. 66, Research Laboratory of Electronics, M.I.T. (1948).
12. S. C. Brown and D. J. Rose, "Methods of Measuring the Properties of Ionized Gases at High Frequencies," Tech. Rep. No. 222, Research Laboratory of Electronics, M.I.T. (1952).
13. S. J. Buchsbaum and S. C. Brown, "Microwave Measurement of High Electron Densities," Phys. Rev., 106 (April 1957), pp. 196-199.

ION-INDUCED OSCILLATIONS OF ELECTRON BEAMS

A. S. Gilmour, Jr.

ABSTRACT

The results of measurements of the properties of transverse and radial ion-induced electron-beam oscillations are described in detail. From the data on the transverse oscillations and from data published by Mihran and Agdur, it is concluded that the transverse oscillations increase in amplitude with time because of interaction after the electrons enter the magnetic focusing field. Because the ion core disturbs the potential well caused by the electrons, the electron beam follows a helical path from the gun to the collector. Ions or electrons traveling toward the gun alter the helical path and cause the oscillations to grow.

The radial oscillations were found to occur at a frequency that was 1.4 to 2 times the transverse frequency. They increase in amplitude with time because, accompanying the oscillation of the ion core, there is a density modulation of the ions in the core that affects the focusing of the electron beam in the convergent Pierce gun in a periodic manner. This causes the diameter of the electron beam to oscillate, which in turn causes the radial oscillations of the ions to grow.

Suggestions are made for the control or elimination of radial and transverse oscillations.

CONTENTS

	Page
I. INTRODUCTION	1
II. DESCRIPTION OF EQUIPMENT	3
III. EXPERIMENTAL OBSERVATIONS	8
A. GENERAL	8
B. TRANSVERSE OSCILLATIONS	9
C. RADIAL OSCILLATIONS	24
IV. DISCUSSION AND CONCLUSIONS	29
V. APPENDIX	30
VI. REFERENCES	39

I. INTRODUCTION

Although a large amount of analytical and experimental work has been carried out during the past 35 years¹⁻¹² in an attempt to explain ion-induced electron-beam oscillations, the questions of how and why the oscillations build up remain unanswered. The purpose of this paper is to present the results of detailed experimental analyses of the behavior of the electron beam during oscillations. These results verify and complement the work of Mihran⁷ and Agdur,¹² which has provided the greatest amount of experimental data to date on ion-induced electron-beam oscillations.

In addition, an extension of the analytical work of Peterson and Puthoff¹¹ is given, which helps in explaining the build-up of oscillations. Peterson and Puthoff¹¹ treat the transverse and radial oscillations of a cylindrical ion core within a cylindrical electron beam that is assumed to be stationary (the time spent by electrons in the plasma is assumed to be very short). The frequency of transverse oscillations of the ion core is found to be

$$\frac{\omega_{LT}}{\sqrt{2}} \left(1 - \frac{c^2}{d^2} \right)^{1/2},$$

where ω_{LT} is the plasma ion frequency first found by Langmuir and Tonks,¹ c is the radius of the ion core, and d is the radius of the anode within which the oscillations are occurring. The frequency of

radial oscillation of the ion core is found to be simply ω_{LT} , when the amplitude of the oscillations is small.

From the analytical and experimental results, the mechanism for the build-up of ion oscillations is deduced, and precautions that may be taken to prevent the build-up are pointed out.

II. DESCRIPTION OF EQUIPMENT

The beam analyzer used in obtaining the data presented in this study is the one described by Gilmour and Hallock.¹³ The electron beam on which measurements were made was generated by the shielded Pierce gun shown at the right-hand side of Figure 1. This gun was normally pulse operated at 5000 volts and had a microperveance of 1.15. At pressures in the range of 10^{-8} Torr, the area compression of the beam was 50:1, and the magnetic field required for Brillouin flow (less than 2 per cent scalloping) was 285 gauss.

The parts of the analyzer essential to the current measurements are shown in Figure 1. A ball valve is shown positioned between the gun and the drift region, which contains a doubly re-entrant cavity and a beam-analyzing mechanism. This valve is considered to be one of the most important parts of the analyzer because when it is closed, the drift tube can be opened to atmospheric pressure while the cathode remains evacuated at a pressure of about 10^{-9} Torr. After the drift tube was evacuated, the valve was opened, and the beam from the gun passed through the aperture in the ball to the beam-modulating and beam-analyzing region.

The beam-analyzing mechanism shown at the left of Figure 1 is shown in cross section in Figure 2. Most of the electron beam was collected by the beam-collecting plate, which was carbonized to reduce the secondary emission. A small portion however, passed through the .010-inch aperture in the center of the plate to a Faraday cage. The

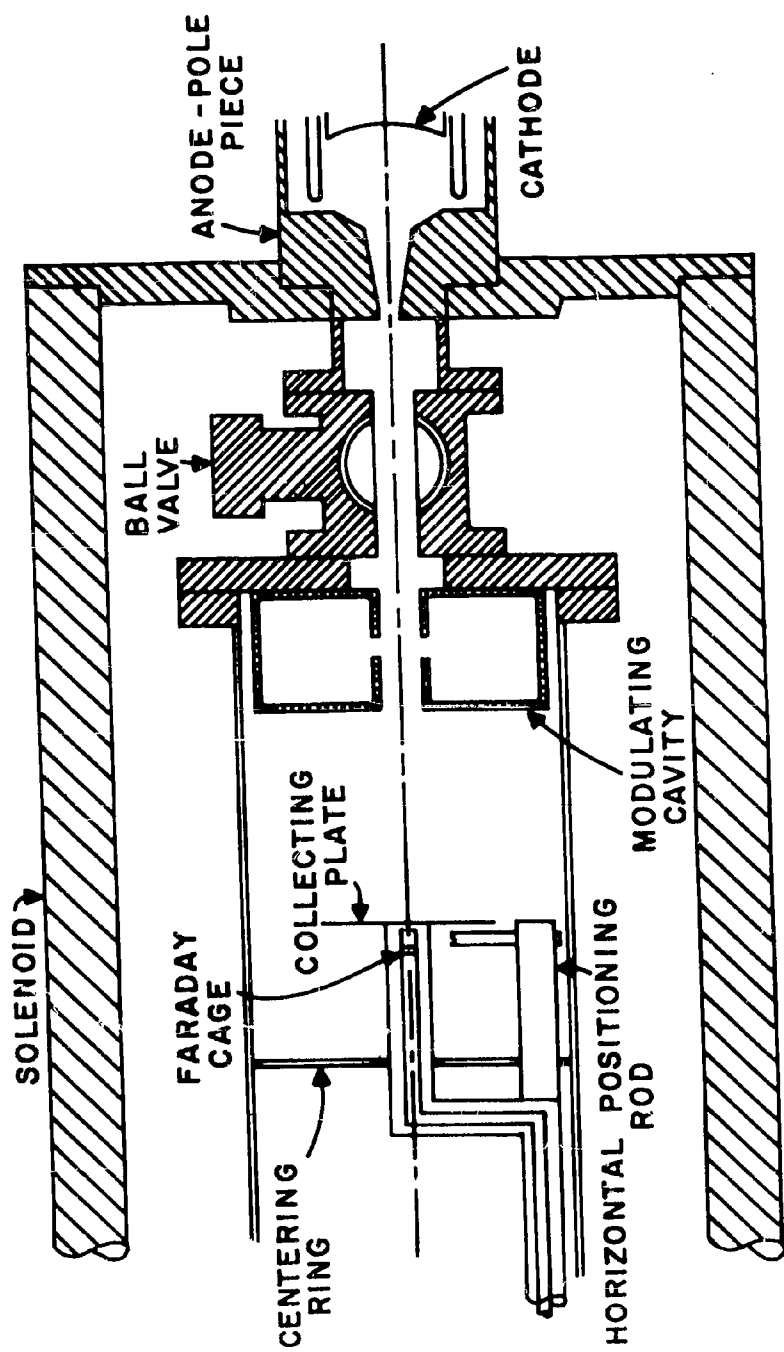


FIGURE 1. Simplified Sketch of Beam Analyzer.

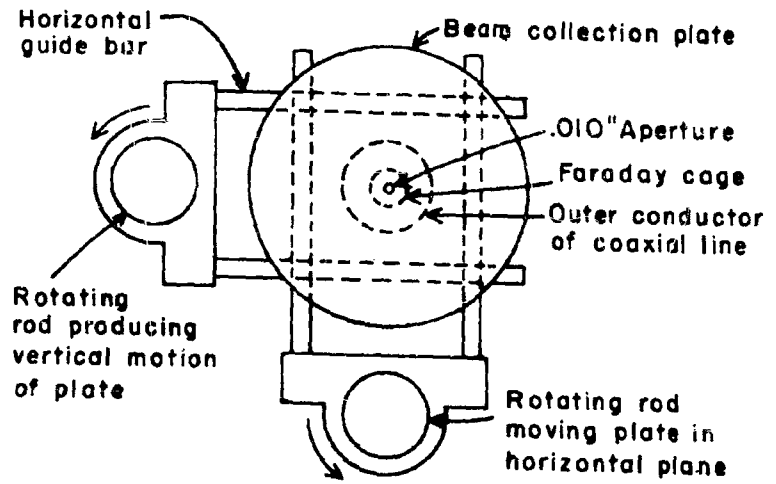


FIGURE 2. Simplified Sketch of Beam Scanner.

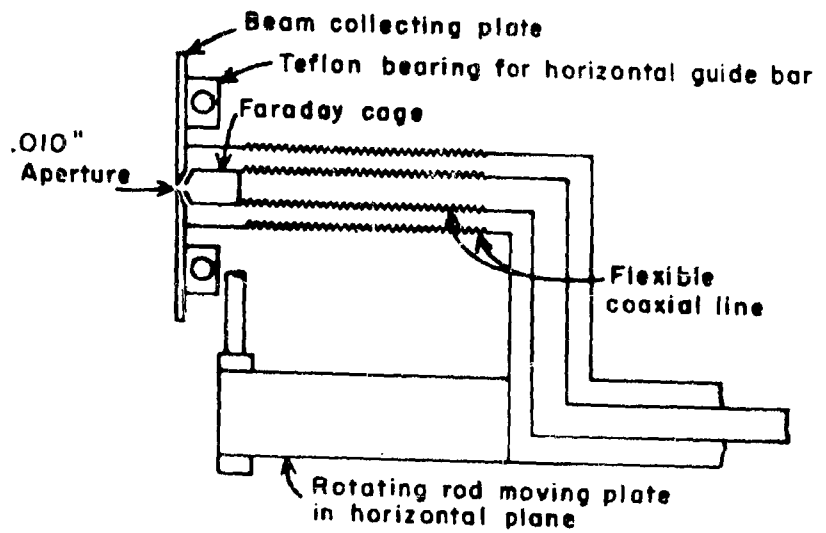


FIGURE 3. Simplified Sketch of Faraday Case and Flexible Coaxial Line.

cage, in turn, was attached to the end of the center conductor of a nonresonant coaxial line, which was used to measure currents at frequencies from d-c to 6000 Mc/s.¹⁴ The current from the cage went out through a coaxial feedthrough in the bottom control rod to an indicating device outside the analyzer.

As shown in Figure 3, a short portion of the coaxial line directly behind the beam-collecting plate was flexible, so that the plate could be positioned in a plane perpendicular to the axis of the solenoid by rotations of the two control rods. Figure 2 shows that the plate could be moved horizontally by rotating the bottom rod, and that vertical motion was produced in a similar manner by rotating the side rod. Although rotational motions were converted to translational motions in positioning the cage, they could be considered linear, since the distances moved were small compared to the length of the lever arms. Axial motion of the cage assembly was produced by moving the control rods through Veeco quick couplings.

The angular position of the rods was adjusted by means of micrometers, the micrometer that set the horizontal position of the cage being equipped with a motor-driven screw. Power being switched to the motor caused the motor to sweep the cage back and forth across the beam automatically. To provide a voltage proportional to the horizontal position of the cage a ten-turn helipot was geared to the motor. The voltage was applied to the X input of an X-Y recorder and a voltage proportional to the cage current was applied to the Y input of the

X-Y recorder, so that plotting of current amplitude as a function of position in the beam was automatic.

To obtain plots of the current density versus position at various times after the beginning of the cathode pulse (necessary because ions caused the beam shape and position to change with time), a Hewlett Packard oscilloscope with a display scanner was used. The output from the display scanner was applied to the Y input of the recorder.

Pressures up to approximately 10^{-3} Torr were obtained by first pumping the analyzer to the low range of 10^{-8} Torr with the 75 l/s ion pump and then backfilling to the desired pressure with hydrogen through a palladium leak. At pressures in the range of 10^{-6} and low 10^{-5} Torr the 75 l/s ion pump was used to help control the pressure; at higher pressures, the 1 l/s ion pump attached to the electron gun was used.

III. EXPERIMENTAL OBSERVATIONS

A. GENERAL

At low pressures ($< 10^{-7}$ Torr) the electron beam used for this study was very nearly an ideal Brillouin beam (at a magnetic field within 2 per cent of the Brillouin value, less than 2 per cent scalloping occurred). No ion-induced oscillations and no phase shift of a r-f signal applied to the beam were observed during cathode pulses with durations up to 30 μ s. This, of course, indicates that at pressures below 10^{-7} mm Hg, the number of ions produced was negligible. As hydrogen was allowed to leak into the analyzer, the effects of ions were first observed at a pressure of approximately 3×10^{-7} Torr, when it was noted that the beam diameter decreased slightly as a function of time.¹⁵ As the pressure was increased further, the beam diameter continued to decrease until, at a pressure near 2×10^{-6} Torr a few cycles of small-amplitude oscillations with a frequency of 6 Mc/s occurred at the end of the 30- μ s cathode pulses. These oscillations were of the transverse type and are described in detail in the following pages. As the pressure was further increased, the transverse oscillations occurred earlier in the pulse and usually increased in amplitude. These oscillations were usually stable and were amplitude modulated at frequencies up to approximately 2 Mc/s.

At pressures in the low range of 10^{-4} Torr the oscillations were still mostly transverse, with a few cycles of radial oscillations

occurring early in the pulse. At a pressure of 5×10^{-4} Torr and a time of 20 μ s after the beginning of the pulse, an abrupt change occurred in the oscillations—they changed from transverse to radial oscillations. Usually the radial oscillations would remain stable for a few cycles and then become very unstable. At the same time that the radial oscillations became unstable, strong electron cyclotron oscillations occurred. The cyclotron oscillations are not described in this report.

B. TRANSVERSE OSCILLATIONS

Figure 4 shows records of the electron current entering the Faraday cage when the aperture in the scanning mechanism was placed at seven positions on a diameter of the beam. Note the phase shift of 180° between the curves at the top and those at the bottom of the figure. These curves and the curves shown in Figure 5 of current density as a function of radial position for the times t_1 through t_6 indicated on Figure 4 show that the electron beam was moving transversely during the oscillations. These data were taken at a pressure of 4×10^{-4} Torr, at a distance of 15 inches from the electron gun with the beam voltage set at 5 kv and the magnetic field at 320 gauss.

Figure 6 shows a curve relating the frequency of the transverse oscillation to the electron accelerating potential. Note that the slope of the curve is nearly one-half, which is the value expected for ion-plasma oscillations when the ion density is proportional to the density of the electrons in the beam from the

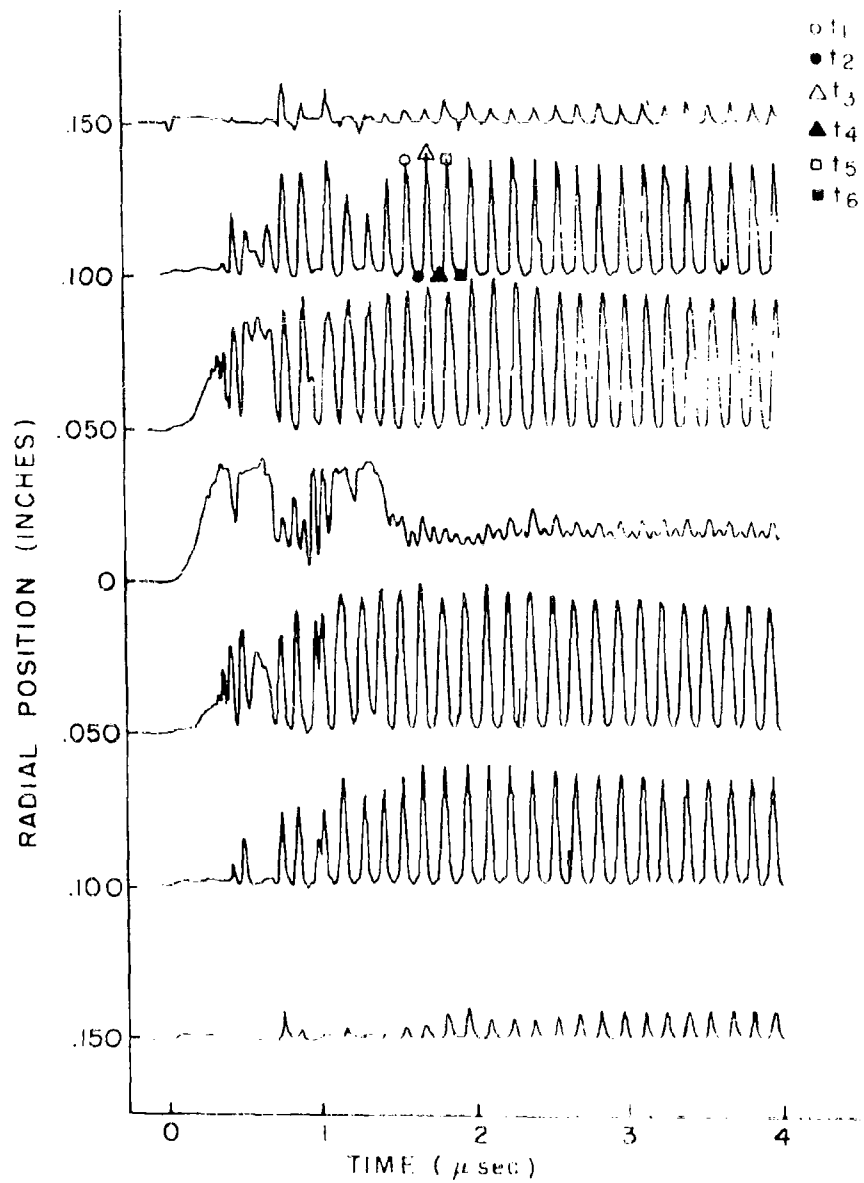


FIGURE 1. Data from the 1962-63 Observations of Electron Beams.

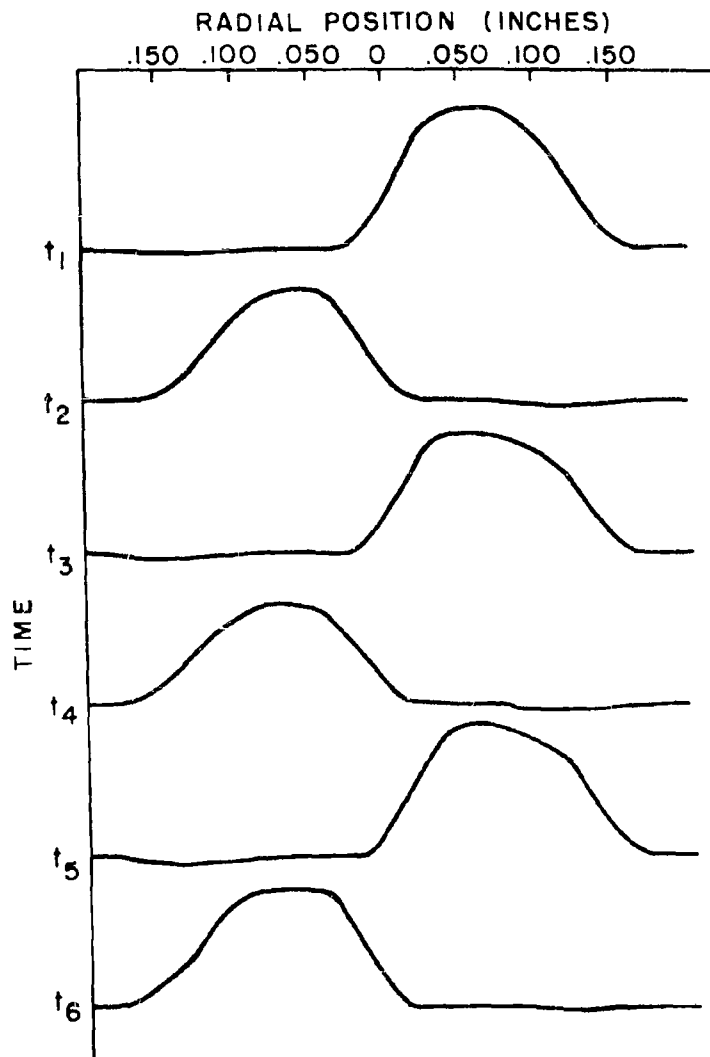


FIGURE 5. Current Density as Function of Radial Position for Times t_1 through t_6 Shown in Figure 4.

electron gun. At one point during measurements, the hydrogen in the vacuum system was replaced by nitrogen, and it was noted that the frequency decreased from 5.6 Mc/s to 1.5 Mc/s. The ratio of these two frequencies is 3.15, which is the square root of the ratio of the mass of N_2 to the mass of H_2 and which is also to be expected for ion-plasma oscillations.

Measurements were made to find out if the oscillation frequency was affected by the strength of the magnetic field.

The unexpected result shown in Figure 7 is related to the dependence of the diameter of the electron beam on the magnetic field. At low levels of magnetic field, the beam diameter was inversely proportional to the field, whereas at high levels (500 gauss and above) the beam diameter was nearly constant because a small amount of magnetic field linked the cathode¹⁶. Since the beam diameter was a function of the magnetic field, the shape of the potential well and the ion-oscillation frequency were a function of the magnetic field. When a small coil was placed around the electron gun and was used to introduce magnetic flux into the cathode region, it was possible to change the shape of the electron beam so that the frequency of oscillation was as low as 3 Mc/s or as high as 10 Mc/s, while the beam voltage, the magnetic focusing field, and the pressure remained constant. It was also possible to change the frequency of oscillation simply by changing the phase of the cathode pulse with respect to the a-c filament current (normally the cathode was pulsed at 60 cps with the pulses being phased so that they

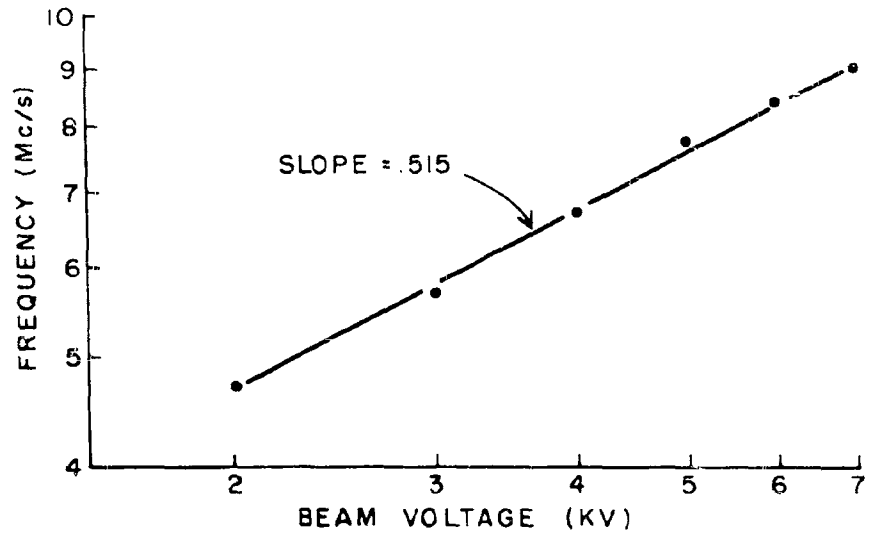


FIGURE 6. Transverse Oscillation Frequency as Function of Beam Voltage.

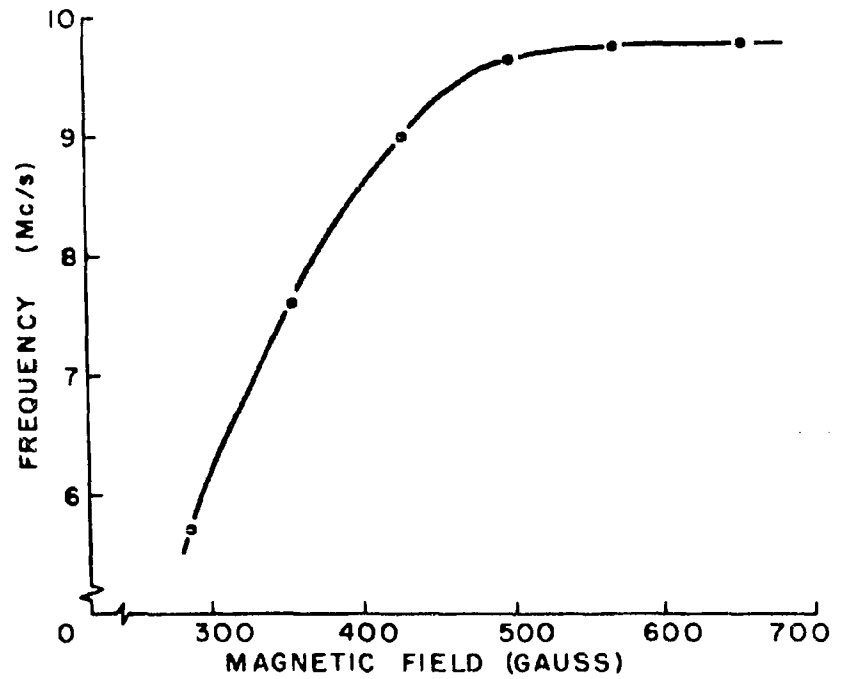


FIGURE 7. Transverse Oscillation Frequency as Function of Magnetic Field.

occurred at zeros of the sinusoidal filament current.) Thus there was no perturbation of the beam by the magnetic field of the filament.

Measurements were made of the frequency of oscillation as a function of pressure and time at a beam voltage of 5 kv and a magnetic field of 0.30 gauss. The frequency at the beginning of transverse oscillations was found to be constant at 8 Mc/s over the pressure range of $5 \times 10^{-6} - 5 \times 10^{-4}$ Torr. A marked variation in frequency occurred as a function of time after the beginning of oscillations (see Figure 8).

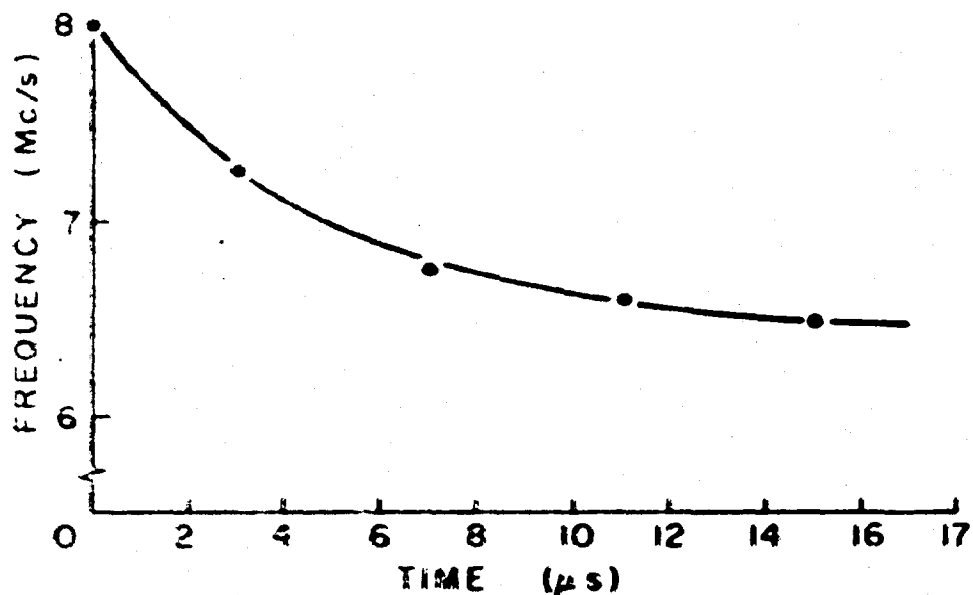


FIGURE 8 Frequency of Transverse Oscillations as Function of Time after Beginning of Oscillations.

Since it seemed unlikely that the beam was moving back and forth in a straight line during transverse oscillations, complete plots of the current density as a function of horizontal and vertical position were made at 60-degree intervals during a few cycles of the transverse oscillations. These plots were made near the beginning of the current pulse, so that the build-up of the transverse oscillation could be observed. The center position of the beam was determined as a function of time from the plots of current density (see Figure 9). Notice that the beam first moved in a path that was nearly linear, but with time, the oscillation path became elliptical. (The data for Figure 9 was taken at an axial position 4 in. from the electron gun.)

With the data from Figures 4, 5, and 9, it is clear that at any axial position, the electron beam followed an elliptical path during transverse oscillations. It is interesting to observe that because of the low transit time of electrons from the gun to the collector (approximately $.10 \times 10^{-6}$ s), no single electron moved in the elliptical orbit of the beam, because the time required to traverse one orbit was about $.15 \times 10^{-6}$ s; thus the assumption of a stationary beam by Peterson and Puthoff¹¹ is at least partially justified. To determine just how "stationary" the beam was as it moved through the beam-analyzing regions, current density was plotted as a function of radial position for various axial positions from

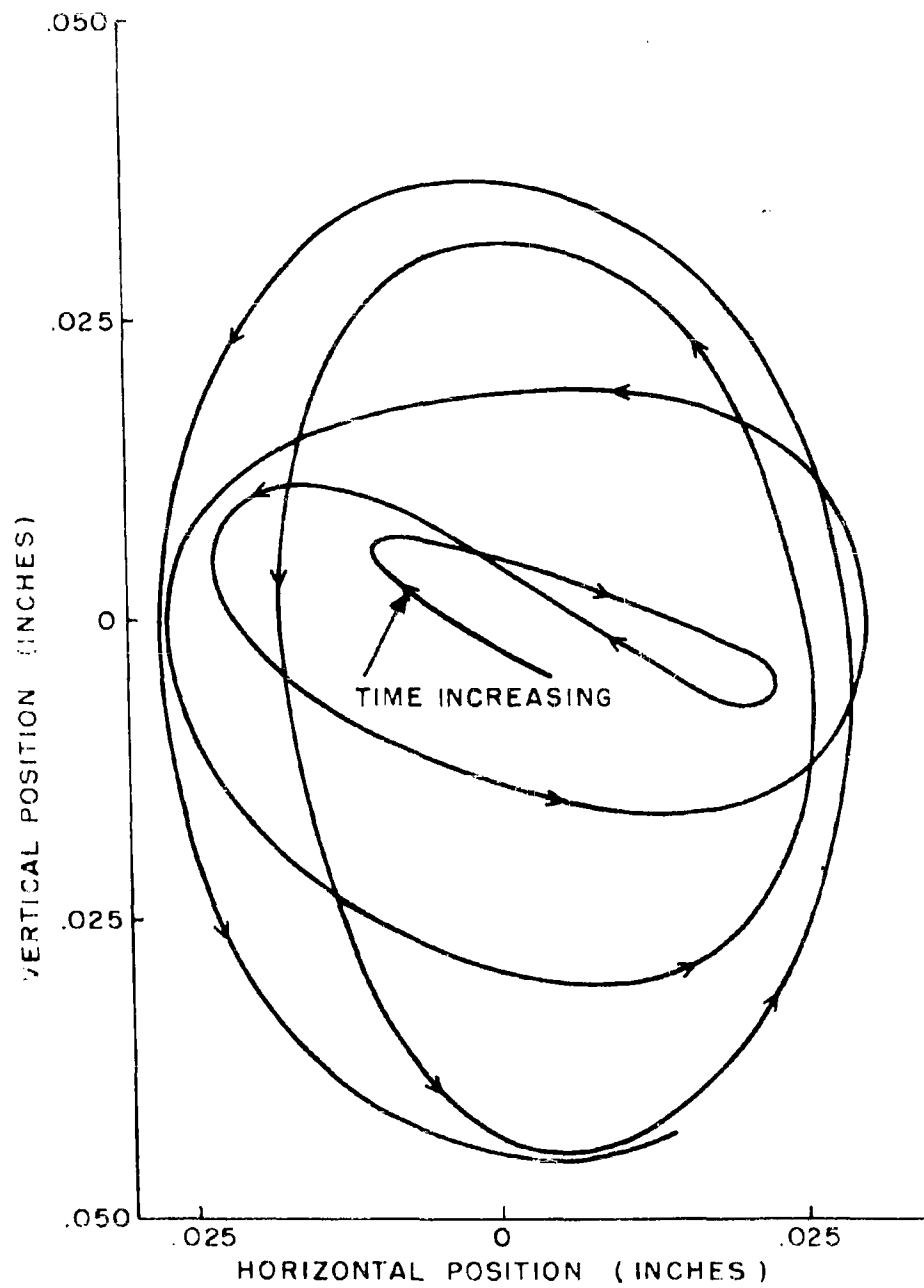


FIGURE 9. Center Position of Electron Beam as Function of Time during Build-up of Transverse Oscillation

the gun at times corresponding to t_1 and t_2 (see Figure 4). From these plots, the center position of the beam in a horizontal plane as a function of axial position was determined and is shown in Figure 10. If the cyclotron oscillation in Figure 10 is ignored it is apparent that instead of following a linear path, the beam followed a path that was a portion of a relatively low-frequency (compared with the cyclotron frequency) sinusoid. Figure 11 shows this path more clearly and shows that it was actually helical. This result has also been observed by Agdur.¹² The reason for the path being helical instead of linear may be understood if the effect on the electron trajectories of an electron-beam well, which is nearly filled with ions, is examined. Let us assume that the ion core is displaced to one side and the electron beam to the other side of the axis of the solenoid, as is shown in Figure 12a. Then a very rough approximation to the potential distribution in the electron beam as a function of radial position from the axis of the solenoid is the parabolic distribution shown in Figure 12b, where it has been assumed that neutralization has occurred in the ion core. If it is assumed that no magnetic flux links the cathode, then it may easily be shown that the trajectory of an electron is of the form,

$$r = A \sin (\theta + Ct) \quad (1)$$

where θ is $\omega_L t$ (ω_L is the Larmor frequency) and C is a constant determined by the density of the beam. Equation (1) shows that the electron's path is a circle which precesses about the solenoid

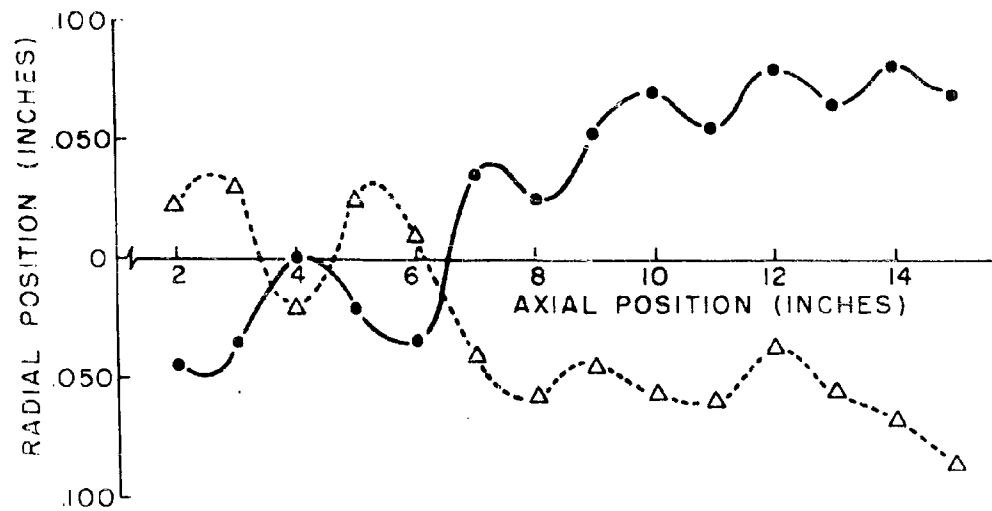


FIGURE 10. Center Position of Electron Beam as Function of Axial Position for Times t_1 and t_2 Shown in Figure 4.

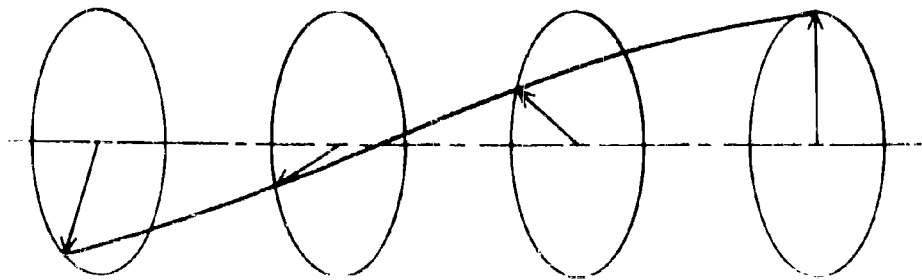


FIGURE 11. Sketch Showing Helical Path of Beam.

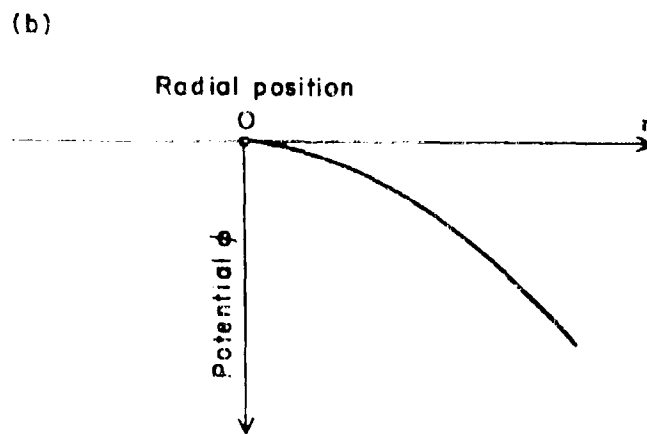
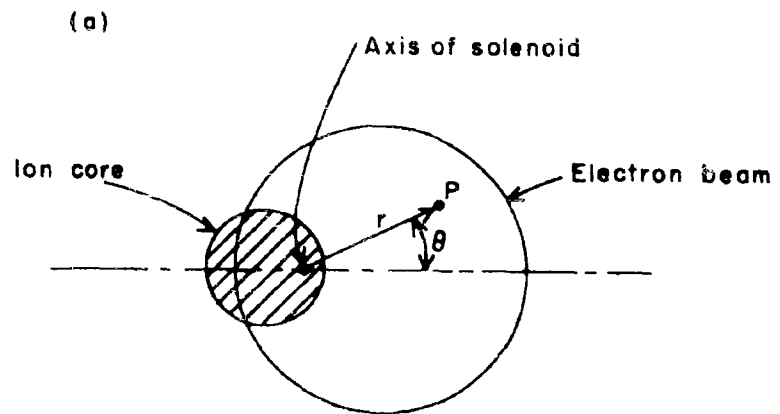


FIGURE 13(a) - Approximate Position of Ion Core with Respect to Electron Beam. (b) Approximate Potential Distribution near Axis of Solenoid

axis. If the constant C is evaluated for a potential drop of 10 volts between the center of the solenoid and the outer edge of the beam, the precession rate shown in Figure 10 is obtained. This 10-volt drop is quite conceivable, when it is remembered that the potential drop from the edge to the center of the beam considered, with no ions present, was 70 volts. From the preceding considerations, it is apparent that the transverse oscillations originated before the electron beam entered the region in which beam measurements were made.

It had been shown⁶ that under some circumstances secondary electrons from the electron beam collector provide the feed-back loop necessary for the build-up of transverse oscillations. For the measurements made in this study, this occurred at low pressure ($< 5 \times 10^{-5}$ Torr). As the collector was moved transversely or axially, both the amplitude of the oscillations and the time at which they started were greatly affected, even though the collector was coated with Aquadag to reduce the emission of secondary electrons to a minimum. It seems probable that it was the high-speed rather than the low-speed secondary electrons that were responsible for the feed-back action, because in the pressure range $< 5 \times 10^{-5}$ Torr for microsecond pulses, the beam was not completely neutralized, causing a potential depression as high as a few hundred volts in the drift tube. This, of course, was enough to stop the low-speed secondary electrons. By using a special beam collector,

Agdur¹² had trapped high-speed as well as low-speed secondary electrons, but although he succeeded in reducing the amplitude of the transverse oscillations by a factor of 5, he was not able to eliminate them.

Mihran found that the suppression of secondary electrons at the collector did not eliminate or even significantly reduce the oscillation of positive ions. It seems therefore that secondary electrons are not necessary for sustaining the oscillations and that some other feed-back mechanism must also exist. It was suggested by Agdur¹² that phenomena in the gun region may be significantly related to the oscillation mechanism. This seems unlikely, however, since the transverse oscillations observed by Mihran, Agdur, and the author are identical, even though the electron guns used were very different (Mihran's gun was gridded, contained a planar cathode, and was shielded from the magnetic field. Agdur's gun also was gridded and contained a planar cathode, but it was completely immersed in the magnetic focusing field. The author's gun was a convergent-flow Pierce gun which was shielded from the magnetic field). It is probable that the transverse oscillations resulted from the influence of ions or electrons (secondary electrons from the collector or from ions) traveling towards the electron gun combined with a disturbance of the profile of the radial potential in the electron beam similar to that shown in Figure 12.

The build-up of transverse oscillations might be accounted for as follows. Assume first that the electron beam was not

oscillating and that it was traveling along the axis of the magnetic focusing field. If the ion core were also centered on the axis of the solenoid, then nothing would happen; however, if the ion core were displaced transversely, as is shown in Figure 13a, the electron beam would follow a helical path, as shown in Figure 13b. The ion core would not remain stationary, but would move toward the center of the electron beam; however, when the ion core moved, the electron beam would assume a new position as shown in Figure 13c. As this process continued, the oscillations of the ion core would increase in amplitude because the electron beam would always be on the opposite side of the axis of the solenoid from the ion core (see the appendix). Now, if an axial potential of the appropriate magnitude increasing in the plus z direction were applied to the oscillating ion core, it would move in the minus z direction and in turn cause the diameter of the helical path of the electron beam to increase. This, of course, would further enhance the ion oscillations, etc.* The oscillations would stop growing when, as shown in Figure 13c, the ion core moved outside the electron beam so that ions were accelerated towards the walls of the vacuum chamber.

*The axial potential resulted from the penetration of the cathode potential into the drift region.

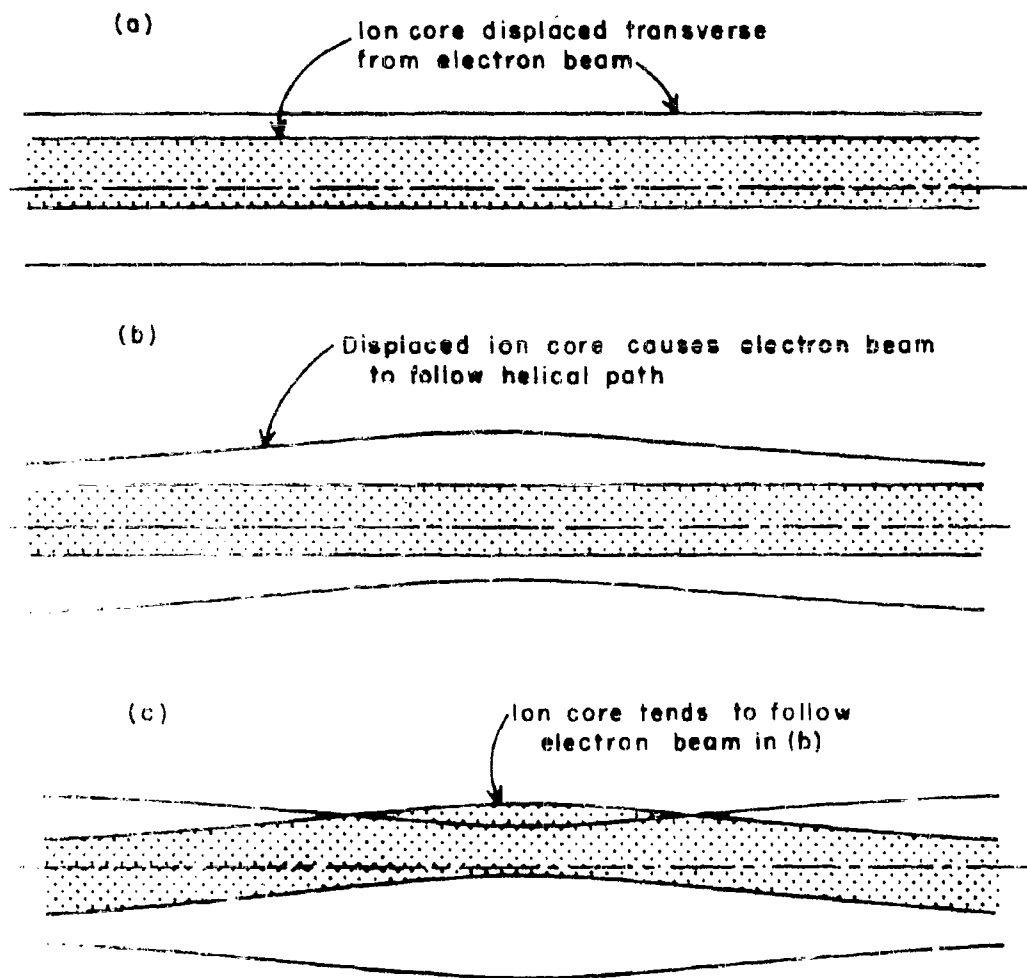


FIGURE 13. Sketches Illustrating Initial Steps in Build-up of Transverse Ion Oscillations

In many cases the axial potential was other than a value that caused continuous enhancement of the ion oscillations so that beating phenomena occurred which produced the variety of amplitude modulations mentioned earlier in connection with the transverse oscillations.

When gridded electron guns similar to those used by Agdur and Mihran are employed to generate electron beams for plasma devices, ions are normally not accelerated towards the gun. Electrons freed from molecules during ionization, however, are accelerated toward the gun, and these can cause a feedback similar to that illustrated in Figure 13.

C. RADIAL OSCILLATIONS

Figure 14 gives a plot of current density as a function of time, which shows that there were at least two distinct modes of ion-induced oscillations in the electron beam at a beam voltage of 5 kv, a magnetic field of 300 gauss, and a pressure of 5×10^{-4} Torr. The oscillations shown between the times of 1 μ s and 3.5 μ s are of the transverse variety described in the previous section. The fluctuations prior to 1 μ s and after 3.5 μ s result from oscillation of the beam radius, as shown in Figure 15. The effect of these radial oscillations on the beam voltage and on the magnetic field was found to be very similar to that of the transverse oscillations, except that at high magnetic fields (> 500 gauss) they disappeared. The frequency was found to be independent of time

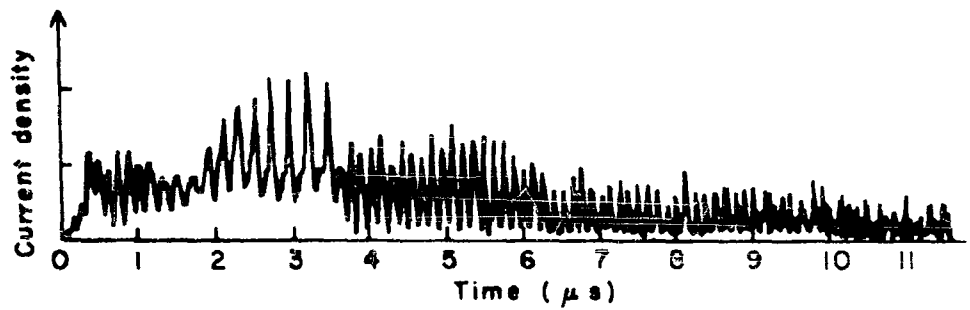


FIGURE 14. Plot of Current Density Showing Two Modes of Ion-induced Beam Oscillations.

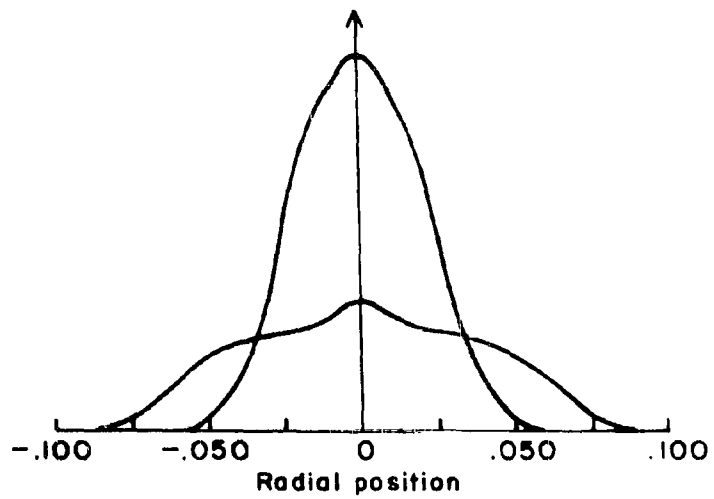


FIGURE 15. Minimum-radius and Maximum-radius Current density Profiles Taken during Radial Oscillations of Beam

and pressure and was higher than the frequency of the transverse oscillations by a factor ranging from 1.4 at the beginning of the transverse oscillations to 2 at the end, as can be seen in Figure 14.

By comparing the predicted frequency of the transverse oscillation

$$\frac{\omega_{LT}}{\sqrt{2}} \left(1 - \frac{c^2}{d^2} \right)^{1/2}$$

with that of the radial oscillation, ω_{LT} , it is seen that for a small ion core, ($c \ll d$), the radial frequency should be $\sqrt{2}$ times the transverse frequency. This compares favorably with the value of 1.4. When c/d is not small, but is instead closer to $3/4$, it is apparent that the radial frequency should be about 2 times the transverse frequency, which agrees with the upper limit of the ratio given.

It is interesting that since the frequency of the radial oscillations was independent of time and pressure, the plasma frequency of the ions ω_{LT} was also constant. This means that changes in the frequency of the transverse oscillations as a function of time (Figure 8) probably resulted from an increase in the radius of the ion core with time.

Since neither Mihran nor Agdur (nor other workers) have reported radial oscillations of the type shown in Figures 14 and 15, it is probable that they are the result of the particular gun geometry used for the measurements made in this study.

It is shown in the appendix that if the diameter of the electron beam oscillates at or near the natural frequency of the radial oscillations of the ion core, then the ion oscillations will build up exponentially with time. In examining the convergent Pierce gun for possible ways in which oscillations of the ion core could cause the diameter of the electron beam to oscillate, it was noted that a density modulation of the ion core could periodically alter the focusing of the electron beam in the region where the beam approached its minimum diameter. Indeed a density modulation of the ion core is to be expected in the region near the gun because both changes in the radius of the ion core and in the radius of the electron beam affect the potential along the axis of the beam, which in turn affects the velocities of the ions and their density.

The absence of radial oscillations at high levels of magnetic field is explained by there being enough magnetic flux linking the cathode and passing through the region where the beam approached its minimum diameter to confine the beam. As a result, no feed-back mechanism existed, and the oscillations failed to grow. The initial occurrence of radial oscillations before the transverse oscillations built up were the result of the rapid build-up of ions in the beam in the 10^{-4} Torr range. Since the ion build-up time was comparable to the period of the radial oscillations, the ion density increased to a large value before sufficient time elapsed for the ions to move radially inward

into the potential well of the electron beam. The ion core then decreased in diameter and oscillations followed. The reasons for the oscillations changing from radial to transverse and back to radial during the cathode pulse are not known.

It appears that radial oscillations of the electron beam can be eliminated by using magnetic fields well above the Brillouin value and by ensuring that the magnetic field links the cathode. Apparently there is no convenient way to prevent the transverse oscillations of the beam when it is necessary to operate a device under conditions (of pressure and time duration), where transverse oscillations normally occur. The only possible solution seems to be to operate at a pressure where radial oscillations normally occur and then to use a magnetic field that is large enough to prevent the transverse oscillations. This means that either very short or very long pulses should be used.

IV. DISCUSSION AND CONCLUSIONS

From the data on transverse oscillations and from the data published by Mihran and Agdur, it can be concluded that the transverse oscillations increase in amplitude with time because of an interaction after the electrons enter the magnetic focusing field. It was found that, because the ion core disturbed the potential well caused by the electrons, the electron beam followed a helical path from the gun to the collector. Ions or electrons traveling towards the gun altered the helical path and caused the oscillations to grow.

The radial oscillations occurred at a frequency that was $1.4-2$ times the transverse frequency. They increased in amplitude with time because, accompanying the oscillation of the ion core, there was a density modulation of the ions in the core that affected the focusing of the electron beam in the convergent Pierce gun in a periodic manner. This caused the diameter of the electron beam to oscillate, which in turn caused the radial oscillations of the ions to grow.

It is concluded that the radial oscillations can be eliminated by using a strong magnetic field that links the cathode and beam-formation regions. It appears, however, that if the transverse oscillations are avoided by operating at high pressure, strong electron cyclotron oscillations occur which may counteract any advantage gained.

V. APPENDIX

It is helpful in understanding the ion-induced beam oscillations if the work of Peterson and Puthoff¹¹ is extended to include the effects of transverse and radial oscillations of the electron beam at or near the plasma frequency of the ions.

Shown in Figure 16 is a sketch of the geometry for transverse oscillation to be analyzed. The potential distribution is found, as was done by Peterson and Puthoff, by superposing the potential resulting from the negative and positive space charges θ_1 and θ_2 , and a space-charge-free potential θ_3 chosen to make the sum of all three potentials fit the boundary condition at the anode (where the potential equals zero).

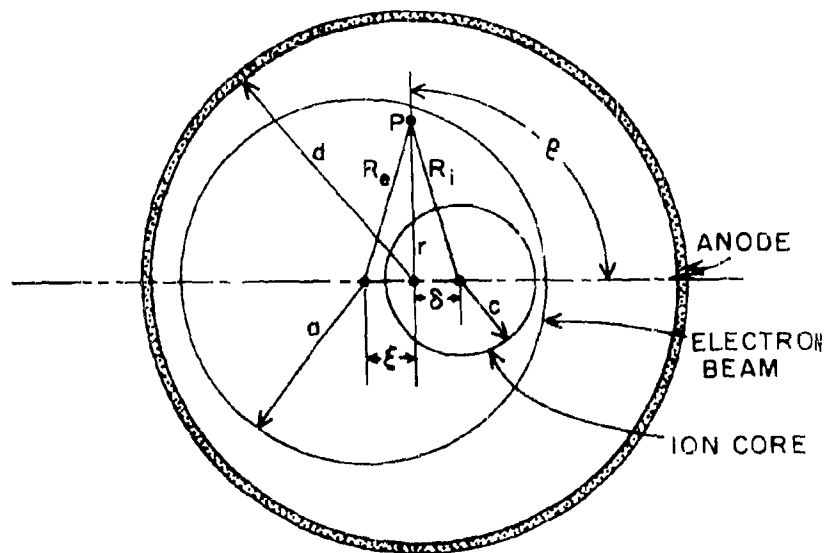


FIGURE 16. Geometry of Transverse Oscillations.

The potential ϕ_1 is given by

$$\nabla^2 \phi_1 = -\frac{\rho_e}{\epsilon_0} \quad (\text{A. 1})$$

or

$$\phi_1 = \frac{\rho_e R_e}{4 \epsilon_0} \quad (\text{A. 2})$$

where

$$R_e = r^2 + \xi^2 - 2r\xi \cos\theta, \quad (\text{A. 3})$$

and ρ_e is the electron charge density. Then

$$\phi_1 \cong \frac{\rho_e}{4 \epsilon_0} (r^2 - 2r\xi \cos\theta) \quad (\text{A. 4})$$

inside the negative space-charge region, and it has been assumed that $\xi \ll r$. Outside the negative space-charge region,

$$\nabla^2 \phi_1' = 0; \quad (\text{A. 5})$$

therefore

$$\phi_1' \cong \frac{\rho_e a^2}{4 \epsilon_0} \left(1 + 2 \ln \frac{r}{a} - 2 \frac{\xi}{r} \cos\theta \right) \quad (\text{A. 6})$$

In a similar manner, the potential in the positive space-charge region resulting from the positive space charge may be found to be

$$\phi_2 \cong -\frac{\rho_e}{4 \epsilon_0} (r^2 - 2r\xi \cos\theta) \quad (\text{A. 7})$$

where it has been assumed that the charge density of the ions equals the charge density of the electrons. Outside the positive space-charge region,

$$\phi_2 = -\frac{\rho_e c^2}{4\epsilon_0} \left(1 + 2 \ln \frac{r}{c} - 2 \frac{\delta}{r} \cos \theta\right) \quad (\text{A.8})$$

On the anode $\phi(r, 0) = 0 = \phi_1 + \phi_2 + \phi_3$ and $r = d$. Therefore inside the anode

$$\begin{aligned} \phi_3 = & -\frac{\rho_e a^2}{4\epsilon_0} \left(1 + 2 \ln \frac{d}{a} - 2 \frac{\xi}{d^2} r \cos \theta\right) + \frac{\rho_e c^2}{4\epsilon_0} \left(1 + 2 \ln \frac{d}{c} \right. \\ & \left. - 2 \frac{\delta}{d^2} r \cos \theta\right) \quad . \end{aligned} \quad (\text{A.9})$$

This means that the total potential is

$$\begin{aligned} \phi_1 + \phi_2 + \phi_3 = & \frac{\rho_e}{2\epsilon_0} \left[\left(1 - \frac{c^2}{d^2}\right) - \xi \left(1 - \frac{a^2}{d^2}\right) \right] r \cos \theta \\ & - \frac{\rho_e}{2\epsilon_0} \left(\frac{a^2 - c^2}{2} + \ln \frac{c}{a} \right) ; \end{aligned} \quad (\text{A.10})$$

therefore the force equation may be written as

$$\frac{d^2}{dt^2} \delta + \frac{\omega_{L\Gamma}^2}{2} \left(1 - \frac{c^2}{d^2}\right) \delta = \frac{\omega_{L\Gamma}^2}{2} \left(1 - \frac{a^2}{d^2}\right) \xi \quad . \quad (\text{A.11})$$

Now if it is assumed that $\xi = \xi_0 \sin \omega t$, the solution is of the form

$$\delta = A \sin \frac{\omega_{L\Gamma}}{\sqrt{2}} \left(1 - \frac{c^2}{d^2}\right)^{\frac{1}{2}} t + B \sin \omega t \quad , \quad (\text{A.12a})$$

when

$$\omega = \frac{\omega_{LT}}{\sqrt{2}} \left(1 - \frac{c^2}{d^2}\right)^{\frac{1}{2}},$$

$$\omega = \frac{\omega_{LT}}{\sqrt{2}} \left(1 - \frac{c^2}{d^2}\right)^{\frac{1}{2}},$$

and

$$\delta = A \sin \left[\frac{\omega_{LT}}{\sqrt{2}} \left(1 - \frac{c^2}{d^2}\right)^{\frac{1}{2}} t \right] + B t \cos \left[\frac{\omega_{LT}}{\sqrt{2}} \left(1 - \frac{c^2}{b^2}\right)^{\frac{1}{2}} t \right] \quad (\text{A. 12b})$$

Thus it is seen that, depending on the value of ω , the transverse oscillations of the ions may be amplitude modulated because of $\sin\omega t$ beating with

$$\sin \left[\frac{\omega_{LT}}{\sqrt{2}} \left(1 - \frac{c^2}{d^2}\right)^{\frac{1}{2}} t \right],$$

and there is the possibility that this could lead to amplitude modulation of the transverse oscillations of the electron beam.

Shown in Figure 17 is a sketch of the geometry for the radial oscillations to be analyzed. Using the notation of Peterson and Puthoff, we take the d-c radius of the plasma column as being r_0 and the instantaneous radius as r_i . The net charge per unit length inside the plasma core caused by ions is $\pi r_0^2 \rho_i$; that

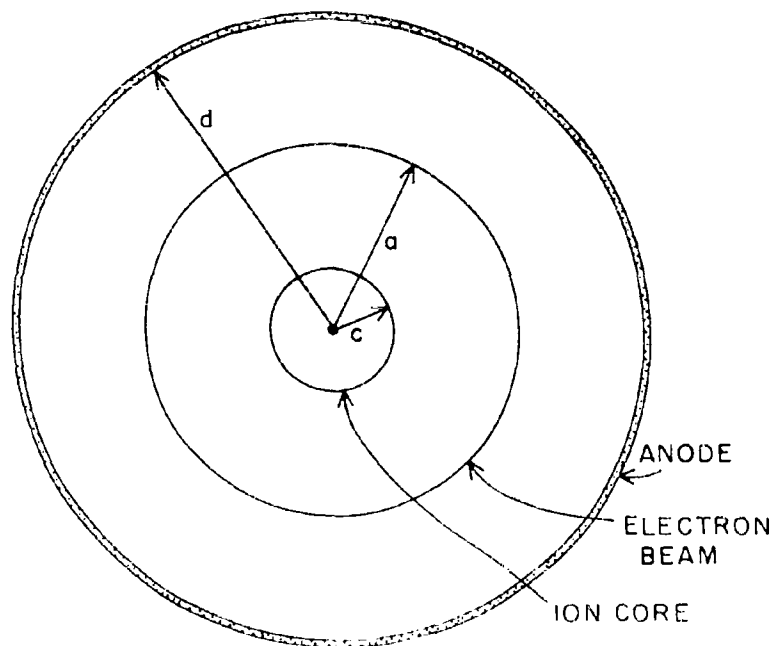


FIGURE 17. Geometry of Radial Oscillation System.

caused by electrons is $-\pi r_1^2 \rho_e$. If it is assumed that ρ_e varies as

$$\rho_e = \rho_{e0} + \rho_{e1} \cos \omega t, \quad (\Delta. 13)$$

where ω is near but not necessarily equal to the oscillation frequency of the ions in the plasma, then by Gauss' law the electric field at the edge of the plasma column is

$$E(r_i) = \frac{r_i}{2\epsilon_0} (\rho_{e0} t + \rho_{e\sim} \cos \omega t - \frac{r_0^2}{2r_1\epsilon_0} \rho_i) ; \quad (\text{A.14})$$

therefore the force equation can be written as

$$\frac{d^2}{dt^2} R + \frac{\eta}{2\epsilon_0} (\rho_{e0} R - \frac{\rho_i}{R} + R \rho_{e\sim} \cos \omega t) = 0 , \quad (\text{A.15})$$

where $r_i/r_0 = R$. When r_i/r_0 is near unity, $1/R = 2 - R$, so the force equation can be rewritten as

$$\frac{d^2}{dt^2} R + (a - 2q \cos 2z) R = b , \quad (\text{A.16})$$

where

$$a = 2 \frac{\eta \rho_{e0}}{\epsilon_0 \omega^2} \left(1 + \frac{\rho_i}{\rho_{e0}} \right) ,$$

$$q = \frac{\eta \rho_{e0}}{\epsilon_0 \omega^2} \frac{\rho_{e\sim}}{\rho_{e0}} ,$$

$$b = \frac{\eta \rho_i}{\epsilon_0 \omega^2} , \quad (\text{A.17})$$

and

$$z = \frac{\omega t}{2} .$$

Equation (A.17) is a Mathieu equation in the form given by McLachlan¹⁷ with the solution given as

$$R = (Ay_1 + By_2) - \frac{1}{c^2} \left[y_1(z) \int^z y_2(u) f(u) du - y_2(z) \int^z y_1(u) f(u) du \right] , \quad (\text{A.18})$$

where y_1 and y_2 are Mathieu functions appropriate for the values of a and q being used, $-c^2$ is the value of the Wronskian $y_2 y_1' - y_1 y_2'$, and $f(u)$ is b . The proper forms of y_1 and y_2 can be determined if the values of a and q are known. Since the ratio of ρ_i to ρ_{e0} is likely to be near unity, and since the ratio of ω_{LT} to ω is also likely to be near unity, it can be seen from Equation (A.17) that $a \approx 4$ and that q is nearly $-\rho_{e\omega}/\rho_{e0}$, where $0 < \rho_{e\omega}/\rho_{e0} < 10$. By examining Figure 18 it can be seen that the solution to Equation (A.16) lies in the unstable region near $a = 4$ to the left of the a axis. When q is small, the functions y_1 and y_2 can be approximated by

$$y_1 \approx e^{\mu z} [-C_2 \cos z_\mu - S_2 \sin z_\mu] , \quad (\text{A.19})$$

$$y_2 \approx e^{-\mu z} [-C_2 \cos z_\mu + S_2 \sin z_\mu] , \quad (\text{A.20})$$

where C_2 and S_2 are constants, and the values of μ are shown in Figure 18. When Equations (A.19) and (A.20) are combined with Equation (A.18), R has the form,

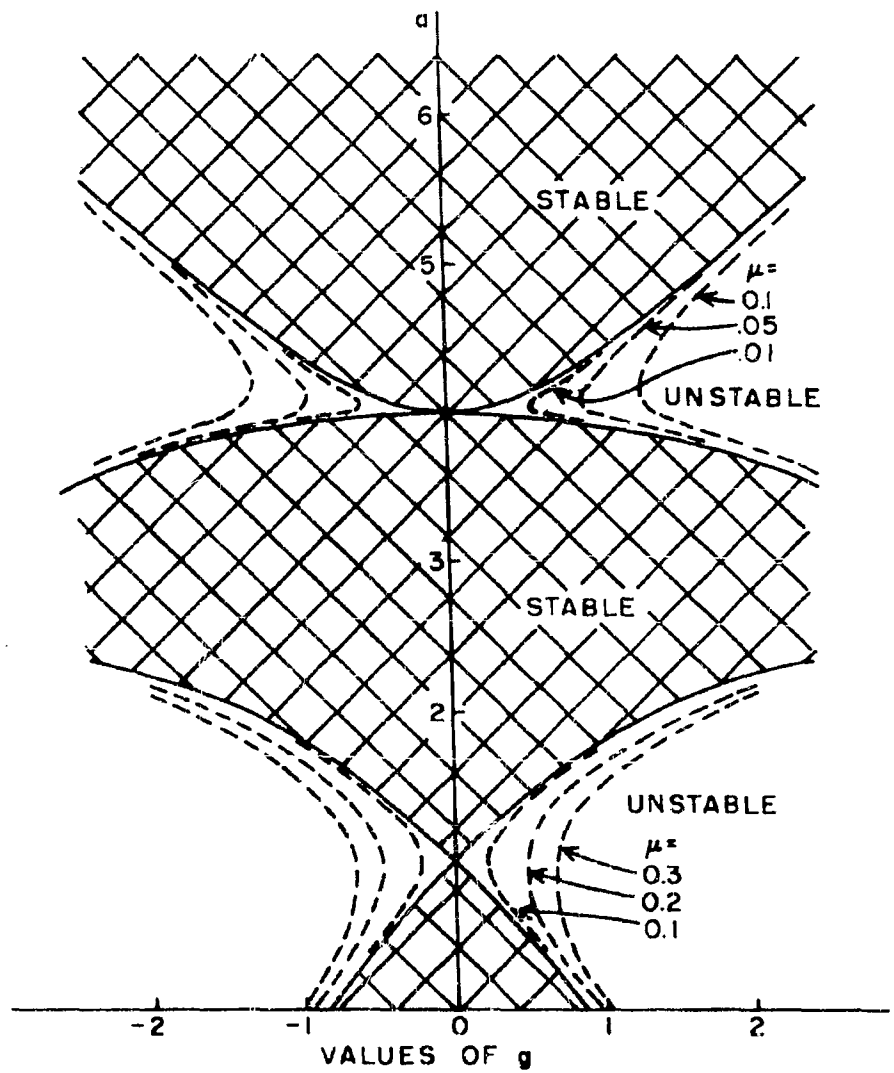


FIGURE 18. Iso- μ Stability Chart for Mathieu Functions of Fractional Order.

$$R = A + Be^{\mu z} \sin 2a + Ce^{-\xi z} \sin 2e + D \sin 4z, \quad (\text{A. 21})$$

where no attempt has been made to retain the phase relationships between the sinusoidal terms. The most important information contained in Equation (A. 21) is that as long as a remains in the unstable region, the frequency of the ion oscillations is the same as the frequency at which the electron beam oscillates, and that the oscillations build up exponentially with time. This means, of course, that amplitude modulation similar to that occurring with transverse oscillations because of the beating of the oscillation frequency of the electron beam with the natural frequency of oscillation of the ion core should not occur in the case of radial oscillations.

VI. REFERENCES

1. L. Tonks and I. Langmuir, "Oscillations in Ionized Gases," Phys. Rev., 33 (1929), pp. 195 - 210.
2. L. Tonks, "The High-Frequency Behavior of a Plasma," Phys. Rev., 37 (1931), pp. 1458 - 1483.
3. L. Tonks, "Plasma-Electron Resonance, Plasma Resonance and Plasma Shape," Phys. Rev., 38 (1931), pp. 1219 - 1223.
4. J. R. Pierce, "Possible Fluctuations in Electron Streams Due to Ions," Jour. Appl. Phys., 19 (1948), pp. 231 - 236.
5. E. G. Linder and K. G. Hernqvist, "Space-Charge Effects in Electron Beams and Their Reduction by Positive Ion Trapping," Jour. Appl. Phys., 21 (1950) pp. 1088 - 1097.
6. K. G. Hernqvist, "Plasma Ion Oscillations in Electron Beams," Jour. Appl. Phys., 26 (1955), pp. 544 - 548.
7. T. G. Mihran, "Positive Ion Oscillations in Long Electron Beams," I.R.E. Trans., ED-3 (1956), pp. 117 - 121.
8. C. Cutler, "Spurious Modulation of Electron Beams," Proc. I.R.E., 44 (1956), pp. 61 - 64.
9. R. L. Jepson, "Ion Oscillations in Electron Beam Tubes; Ion Motion and Energy Transfer," Proc. I.R.E., 45 (1957), pp. 1069 - 1080.
10. J. T. Serise, "Note on Positive-Ion Effects in Pulsed Electron Beams," Jour. Appl. Phys., 29 (1958), pp. 839 - 841.

11. W. W. Peterson and H. E. Puthoff, "A Theoretical Study of Ion Plasma Oscillations," I.R.E. Trans., ED-6 (1959), pp. 372 - 377.
12. B. Agdur, "Oscillations in Long Electron Beams," Ericsson Technics (1960), pp. 534 - 539.
13. A. S. Gilmour, Jr., and D. D. Hallock, "A Demountable Beam Analyzer for Studying Magnetically Confined Electron Beams," Paper presented at the Sixth National Conference on Tube Techniques, New York City, 1962.
14. A. S. Gilmour, Jr., G. C. Dalman, and L. F. Eastman, "The Current and Velocity Distributions in a Velocity-modulated, Brillouin-focused Electron Beam," Paper presented at the 4th International Congress on Microwave Tubes, Scheveningen, Holland, September 1962.
15. A. S. Gilmour, Jr., and D. D. Hallock, "Ion Effects in a Brillouin Beam," Research Report EE 545, Cornell University, 1962.
16. D. D. Hallock, "An Investigation of the Laminarity of Flow in a Magnetically Confined Electron Beam," Research Report EE 539, Cornell University, 1962.
17. N. W. McLachlan, "Theory and Application of Mathieu Functions," London: Oxford University Press, 1947.